Forced Navier-Stokes flows on a bounded two-dimensional domain

Forced Navier-Stokes Flows on a Bounded Two-Dimensional Domain

David Molenaar

Omslagontwerp: Jan-Willem Luiten / David Molenaar
Druk: Printservice TUE

CIP-DATA LIBRARY TECHNISCHE UNIVERSITEIT EINDHOVEN

Molenaar, David

Forced Navier-Stokes flows on a bounded two-dimensional domain /
by David Molenaar.-
Eindhoven: University of Technology Eindhoven, 2004.-
Proefschrift.-
ISBN 90-386-2025-X
NUR 928
Trefwoorden: turbulentie / chaos / wandeffecten / schaling
Subject headings: turbulence / chaos / wall effects / scaling

Forced Navier-Stokes Flows on a Bounded Two-Dimensional Domain

PROEFSCHRIFT

ter verkrijging van de graad doctor aan de
Technische Universiteit Eindhoven op gezag van
de Rector Magnificus, prof.dr. R.A. van Santen,
voor een commissie aangewezen door het College
voor Promoties in het openbaar te verdedigen op
woensdag 17 november 2004 om 16.00 uur

door

David Molenaar

geboren te Enschede

Dit proefschrift is goedgekeurd door de promotoren:

prof.dr.ir. G.J.F. van Heijst
en
prof.dr. D. Lohse

Copromotor:
dr. H.J.H. Clercx

Financial support by the Foundation for Fundamental Research on Matter (Stichting FOM) is gratefully acknowledged.

To my Father & Juuleke and to my Mother,
whose incommensurate frequencies shaped so much of my world.

Contents

Chapter 1

Introduction

All truths are easy to understand once they are discovered; the point is to discover them.
Galileo Galilei (1564 - 1642)

A complete understanding of the turbulence in fluids stands as perhaps the last great problem of classical physics. While the equations of fluid motion have been known for a long time, the system is essentially still a black box, where the core of the problem is its strong nonlinearity. Not surprisingly then, a comprehensive theory of turbulence is still lacking, notwithstanding experimental and theoretical efforts by such great physicists as G.I. Taylor and A.N. Kolmogorov, which have shed light on many aspects of turbulent flows. Even the development in the last quarter of the twentieth century of chaos theory, providing a framework of analysis for a wide scala of nonlinear phenomena, eventually proved insufficient for the turbulence problem.
In a sense turbulence is as much a mathematical problem as it is a physical one. As remarked by Foias *et al.* [49], the equations of fluid motion, the Navier-Stokes equations, are one of the few examples in physics where the nonlinearity arises solely due to kinematical, or mathematical, considerations. But the mathematical difficulties accompanying the turbulence problem are in no sense less than their physical counterparts. In fact, the difficulties in proving existence and uniqueness of solutions for the Navier-Stokes equations are so great that the prestigious Clay Institute of Mathematics turned it into one of seven Millennium Problems, offering a million dollar prize for its solution.

Let us recall then, in broad terms and before involving any tedious mathematics, some basic aspects of the turbulence problem and simultaneously try to indicate why it remains such a fascinating topic of study.

1.1 Preliminaries

While most (if not all) fluid flows in nature live in three spatial dimensions, some systems exist which are assumed to be more or less two-dimensional (2D). It is either rotational effects, negligible vertical dimensions as compared to horizontal dimensions, density stratification effects, or a combination of these causes which render the motion two- rather than three-dimensional. Let us immediately add the restriction of constant fluid density, the so-called incompressibility condition. As such, the 2D Navier-Stokes equations supplemented with the incompressibility condition are thought to be

an appropriate model for systems as diverse as the large-scale atmospheric flow, Tennekes [139], to the flow in extremely thin films of soap, see Goldburg *et al.* [58]. With these restrictions in hand, we turn to examine the phenomenology of our system.

To study a viscous flow we first have to push the fluid into motion, e.g., by means of an initial condition. We only need to know the exact conditions of the fluid in terms of pressure and velocity at one convenient moment of our choosing, at which we set time equal to zero. If we apply an initial condition and then let the flow evolve without interfering, we speak of a freely decaying flow; eventually the fluid will come to rest because its kinetic energy is depleted by viscous dissipation. Contrarily, in a forced flow some kind of external forcing mechanism, like a mechanical stirring device or a blowing wind, continuously adds kinetic energy, balancing the viscous dissipation. It is these forced flows which we are mainly concerned with in the sequel. Specifically, we are interested in the phenomenology of forced flows enclosed by rigid walls.

An important guideline for our observations is the dimensionless Reynolds number, Re, which measures the relative strength of viscous damping to nonlinear processes. It will be shown later how this number arises, here we are content with its formula,

$$Re = \frac{U\ell}{\nu}, \tag{1.1}$$

where U is a characteristic velocity scale, usually a root-mean-square velocity, ℓ a characteristic length scale, e.g., the length of the flow domain and ν the kinematic viscosity parameter. It is the Reynolds number which tells one how many degrees of freedom a flow contains and which, consequently, determines what type of phenomenology one can observe. Even though Re is essentially finite for a viscous flow, it can still be a huge number, e.g. for the atmosphere one may encounter a dazzling integral-scale Reynolds number of $Re = \mathcal{O}(10^{10})$. It is exactly the possibility of such large Reynolds numbers that prohibits calculations of highly turbulent flows, as the number of computational modes in a detailed computation should equal or exceed the number of degrees of freedom of such flows.

So let us imagine a small experiment, assuming we observe a fluid, subject to a controllable external forcing. The simplest motion, associated to low values of the Reynolds number, is stationary and laminar, the flow is ordered, does not change in time and behaves in a completely predictable way. Based on our present observations of the flow and knowing that we have isolated the fluid from the rest of the world, we can safely predict its future behavior for all eternity; it remains exactly the same as what we observe.
Suppose next that we increase the intensity with which we force the flow, supplying more energy to the flow and thereby increasing the Reynolds number. The stationary behavior is now replaced by a time-dependent motion. Although the nature of this time dependency is ordered and regular, e.g., in the form of repetitive or periodic motion, it is not possible to exactly predict for which forcing amplitude this behavior will occur and what form it precisely has.
Again we increase the intensity of the forcing, this time supplying so much energy to the flow that order in the temporal signal is destroyed. The resulting flow is time-dependent, but now so in an irregular, erratic way. In other words the flow has become chaotic, or, if we supply even more energy, turbulent.

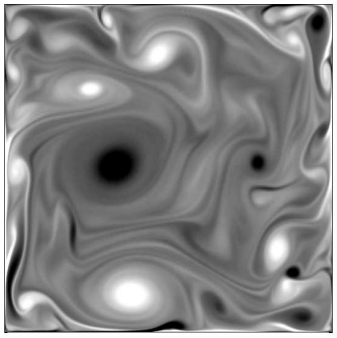

Figure 1.1: *A snapshot of the vorticity field of a 2D turbulent flow in a bounded domain, black indicates negative values, white means positive values. Note the presence of intense boundary layers and many vortices of varying size and strength.*

In daily vocabulary turbulent is synonymous to disordered, uncontrolled, or even violent (English dictionary). As used by physicists, however, turbulence refers to something much more complex than just a random or disordered process. Within a sea of disorder, organized structures may arise in the form of eddies, or vortices. These vortices form, interact and die out from the smallest to the largest spatial scales, from the sink hole vortex one can observe when a bathtub is emptied to the devastating hurricane storms which may affect entire nations. Here, the distinction between two- and three-dimensional flows becomes apparent, as their turbulent phenomenologies are strikingly different.
A key concept in the 2D phenomenology is that, under the right circumstances, a self-organization of the flow may take place. Small eddies of equal sign merge to form ever larger structures. Typically, the eddies have the form of a single core, known as a monopolar vortex, or of two counter rotating cores, known as a dipolar vortex. More exotic configurations may also arise, as, e.g., the tripolar vortex observed by Van Heijst and Kloosterziel [146], which consists of a large core with two counter-rotating satellites. In the turbulent sea surrounding the larger vortices, small-scale structures abound, sometimes, as a result of shearing of large vortices, in the form of elongated patches, known as filaments. An example of these structures is given in Figure 1.1, which depicts the vorticity field[1] during a turbulent flow on a bounded square domain, for modest Reynolds number, $Re \simeq 5000$. The plot is a computational result and shows both the presence of intense boundary layers and filamentary structures as well as many vortices of varying size, strength and sign.

It is exactly the creation of coherent vortices that lends a flow its aesthetical beauty and, at the same time, makes the 2D turbulence problem so complex. Specifically, the influence of these structures on the turbulent dynamics is poorly understood. Let us, however, take a brief look at some mechanisms that are thought to drive these dynamics and constitute the most important theory of 2D turbulence to have emerged so far.

Heuristic turbulence theory

Conjectures on the transfers of energy and squared vorticity by the non-linear dynamics and the associated scaling behavior of the energy spectrum were posed in the late

[1]The vorticity is the rotation of the velocity field, it is an especially suitable quantity for the visualization and analysis of a two-dimensional flow field consisting of vortices and small-scale structures.

sixties of the previous century, by Kraichnan [74], Leith [78] and Batchelor [10], hereafter collectively referred to as KLB-theory. We repeat the Kraichnan argument for an infinite domain, assuming that an ideal random forcing pumps a fixed amount of energy and squared vorticity into the flow. The forcing acts at a fixed length ℓ_f within the inertial range; the part of the spectrum that is dominated largely by the non-linear dynamics and remains unaffected by viscous dissipation processes. These latter processes are assumed to act only on the smallest length scales, below the so-called cut-off length, ℓ_η. On dimensional grounds, this latter length follows from the spectral enstrophy dissipation rate η and the kinematic viscosity ν, as

$$\ell_\eta = \left(\frac{\nu^3}{\eta}\right)^{1/6}.$$

Based on the assumption of locality of length scale interactions, KLB-theory conjectures that a transport, or cascade, of energy towards larger wavelengths takes place in the range $\ell \gg \ell_f$. The transfer process is known as the inverse energy cascade, because it is exactly opposite to the downward-in-wavelength transfer of energy in three-dimensional turbulence.
Let $\mathbf{u}(t,\mathbf{x})$ denote the fluid velocity vector at time t and position $\mathbf{x} = (x,y)$ in a domain Ω. One can define its Fourier transform as

$$\hat{\mathbf{u}}(t,\mathbf{k}) = \int_\Omega \mathbf{u}(t,\mathbf{x}) e^{-i\mathbf{k}\cdot\mathbf{x}} \mathrm{d}A,$$

for discrete wave vector $\mathbf{k} = (k_1,k_2) \in \mathbb{Z}^2\backslash\{0\}$. KLB-theory predicts that, in the inverse cascade range, the spectral energy $E(k) \equiv |\hat{\mathbf{u}}(t,\mathbf{k})|^2$ scales with wavenumber $k = |\mathbf{k}|$. On dimensional grounds the scaling must be

$$E(k) = c_0 \epsilon^{2/3} k^{-5/3} \quad \text{for} \quad k \ll k_f,$$

where ϵ is the spectral energy dissipation rate, $k_f = 2\pi\ell_f^{-1}$ the forcing wavenumber and $c_0 = \mathcal{O}(1)$ a non-dimensional constant.
Instead, in two dimensions it is the squared vorticity, or enstrophy, that is transported downward in length scale, also referred to as the direct cascade. Starting at the forcing length ℓ_f, enstrophy is transferred to progressively smaller wavelengths. Above the forcing wavenumber, the spectral enstrophy dissipation η is used to obtain the scaling

$$E(k) = c_1 \eta^{2/3} k^{-3} \quad \text{for} \quad k_f \ll k \ll k_\eta,$$

where $c_1 = \mathcal{O}(1)$ is another non-dimensional constant and $k_\eta = 2\pi\ell_\eta^{-1}$. Because nonlinear interactions in two dimensions take place in the form of triads of wavenumbers, in which one wavenumber emits, one wavenumber receives and the intermediate wavenumber transmits energy or enstrophy, the cascades of these latter quantities are mutually exclusive. According to KLB-theory one cannot observe enstrophy transport in the inverse cascade range and, likewise, one cannot observe energy transport in the direct cascade range.
Furthermore, the enstrophy transfer persists indefinitely, achieving a statistically steady state, where input is balanced by destruction due to viscosity. The energy transfer, on the other hand, is not balanced by dissipative processes, but rather continues until it reaches an infinite wave length, for which it needs an infinite amount of time. As such, it lives in a quasi steady-state. Infinite domains are, however, not encountered

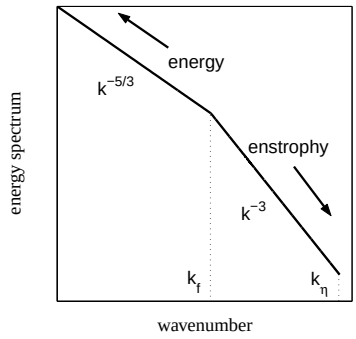

Figure 1.2: *Double logarithmic energy spectrum, showing the dual cascade of energy and enstrophy and the associated -5/3 and -3 scaling behavior, where k_f denotes the forcing wavenumber and k_η the dissipation wavenumber.*

in physical reality and Kraichnan conjectured that a piling-up of energy in the largest wavelength mode would occur in a finite domain, a so-called condensation regime. Summarizing, the KLB situation is shown in Figure 1.2.

Let us examine the physical picture corresponding to the somewhat abstract cascade ideas. The transfer of energy to ever larger wavelengths is generally thought to be associated to the self-organization of energy-containing vortices into ever larger structures. An alternative view was forwarded by Paret and Tabeling [107] and by Boffetta *et al.* [14], who suggested that the inverse cascade is manifested in a clustering, rather than a merging, of like-signed vortices.
The enstrophy transfer, as described by Batchelor [10], is brought about by the amplification of vorticity gradients due to the extension of iso-vorticity lines by the large-scale flow field. This explanation may seem slightly cryptical, but recall the description of filaments containing large amounts of vorticity. If such a filament is wound around a large vortex it is both stretched in one direction and squeezed in the other, as would happen with an elastic band which is stretched tightly around a large package of mail. Naturally, the vorticity gradients in our stretched filament are enlarged such that viscous dissipation becomes important.

Any theory stands or falls with its confirmation or rejection by experimental evidence and KLB-theory with its prediction on scaling exponents, has been widely tested in both laboratory experiments and computational models. Hence, we consider next some of the experimental and numerical techniques, used to study (quasi) 2D turbulence. An extensive literature exists, see also the overview of laboratory experiments by Kellay and Goldburg [69], the review by Tabeling [133] or the forthcoming overview by Carnevale [21] and we limit our summary to work that is directly relevant for the remaining part of the thesis.

Laboratory Experiments and Computational Models

In one of the first experiments on quasi-2D turbulence, Sommeria and Verron [130, 129] used a set-up in which magnetic (Lorentz) forces assume the role of the Coriolis forces in a rotating experiment, suppressing vertical motions in a thin layer of mercury contained within a square tank. Several interesting phenomena were observed, including an inverse cascade of energy and what seemed to be a condensation regime, in the form of a domain-filling circulation cell. More than a decade later, Paret and

Tabeling [107, 106] used an array of magnets underneath a square tank to excite a turbulent flow in a shallow fluid layer, in which three-dimensional motion was suppressed by density stratification. Again a domain-filling circulation cell occurred, possibly corresponding to a condensation regime. Furthermore, an inverse energy cascade was observed and evaluation of vorticity statistics seemed to confirm KLB-scaling. These experiments could be conducted for a limited span of time only, due to three-dimensional mixing effects and subsequent loss of stratification. It was argued in this context by Satijn *et al.* [124], that bottom-drag may, in effect, lead to a non-negligible three-dimensional structure of the flow, depending on the fluid depth and the Reynolds number.

An alternative set-up was constructed by Kellay *et al.* [70, 68], studying various aspects of turbulence in a thin soap film, see also Goldburg *et al.* [58], Rutgers [121] and Martin *et al.* [91]. These experiments rejected KLB-scaling in the inverse cascade range, but confirmed it in the direct cascade range. However, Rutgers *et al.* [122] showed that the presence of air-drag probably caused the observed deviations from KLB scaling. An open problem for these particular experiments is the occurrence of soap-film thickness variations, violating the incompressibility condition.

With exception of the soap-film experiments, which suffer mostly from fluid-air interactions, all experimental set-ups have rigid walls and bottoms that cause the generation of fluid boundary layers. The interactions of the flow with the rigid container bottom and side walls and the questionable two-dimensionality of the experiments are in clear violation with the fundamental assumptions of KLB-theory. Even so, some of the predictions following from KLB-theory were more or less confirmed in laboratory experiments, which is a remarkable fact by itself.

The first direct numerical simulations (DNS) of forced 2D flows under periodic boundary conditions were presented by Lilly [82], apparently confirming KLB-theory. However, these results were questionable due to a very limited computational resolution. Some time elapsed before higher resolution computations became available, as, e.g., those by Frisch and Sulem [54], who observed an inverse cascade range, and those by Legras *et al.* [77], who noted both deviations from KLB-scaling in the direct cascade range and the presence of coherent structures, see also the forthcoming overview by Carnevale [21].

While boundary effects are excluded in a double-periodic domain, one is still stuck with a largest computational mode, effectively limiting the size of the system. Indeed, the usual (quasi-stationary) end-state seems to be a condensation regime, but contrary to the laboratory experiments, here the condensation is in the form of a domain-filling dipolar vortex, as demonstrated by, e.g., Mattheus *et al.* [92] for flows decaying over long times and by Hossain *et al.* [64] for forced flows. Several methods have been applied to prevent the piling-up of energy in the largest mode, as, e.g., the introduction of Ekman damping for the lowest computational modes by Maltrud and Vallis [87], essentially a linear damping mechanism, or the use of hypoviscosity by Borue [15], in which an inverse higher-order dissipation operator is added to the equations of motion. In the latter case the normal viscous dissipation is usually replaced by a higher-order dissipation operator, referred to as hyperviscosity. Besides removing unwanted energy condensation, the latter mechanism also serves to effectively extend the inertial range, confining viscous dissipation to smaller scales. A major drawback of these methods

is, however, that one deliberately alters the equations of motion, such that the resulting flow is no longer a pure Navier-Stokes solution.
Whatever the computational model used, there is still considerable debate amongst the experts concerning the KLB-conjectures. Predictions on spectral scaling exponents in forced flows and the effect of intermittency, or coherent structures, on these exponents have been questioned for both the inverse cascade regime, see Borue [16], Boffetta *et al.* [14], Frisch and Sulem [54], Maltrud and Vallis [87], Smith and Yakhot [127] or Rutgers [121], as well as for the direct cascade regime, see Borue [15], Chen *et al.* [23], Ishihara and Kaneda [65, 67], Legras *et al.* [77], Lindborg and Alvelius [83], Maltrud and Vallis [87] or Ohkitani [102]. Furthermore, the locality of length scale interactions in the inverse cascade range, see Maltrud and Vallis [88] or Danilov and Gurarie [33, 32], and even the very possibility of a direct enstrophy cascade, see Tran and Bowman [142], have been subject of debate. Of course, the limits $t \to \infty$ and $\nu \to 0$ are notoriously hard to achieve in both laboratory and computational experiments; departures from classical theory can still be blamed on the failure to achieve either of these limits.

Chapter outline

In the following parts of this Chapter we discuss the inevitable mathematical side of the problem, proceeding with a formulation of the governing equations in Section 1.2.1 and a summary of some functional analytic aspects in Section 1.2.2, i.e., mainly the associated function spaces and important norm-inequalities. Equipped with the language of Section 1.2.2 we return to several aspects of the theory of viscous 2D flows in Section 1.3, considering *a priori* estimates on several integral quantities and consequences of the fact that laboratory or computational domains are finite and possibly equipped with no-slip walls. Finally, we conclude this chapter with an outline of the remaining part of the thesis in Section 1.4.

1.2 Mathematical fundaments

1.2.1 Evolution equations

Suppose an incompressible fluid of unit density, $\rho = 1$, fills a two-dimensional domain $\Omega \in \mathbb{R}^2$. We require the domain-boundary $\partial\Omega$ to be sufficiently smooth (that is, locally Lipschitz-continuous of, at least, order C^1, see, e.g., Zeidler [155]). Looking at this fluid from an inertial frame of reference any movement of the domain with respect to the surrounding universe can be disregarded. Thus a fluid flow in Ω can be described by the Eulerian velocity $\mathbf{u}(t, \mathbf{x}) = (u(t, \mathbf{x}), v(t, \mathbf{x}))$ and the scalar kinetic pressure field $p(t, \mathbf{x})$ at time t and position $\mathbf{x} = (x, y)$, while it evolves according to the Navier Stokes equations

$$\partial_t \mathbf{u} + (\mathbf{u} \cdot \nabla)\mathbf{u} + \nabla p - \nu \Delta \mathbf{u} = \boldsymbol{f} \qquad \text{in} \quad \mathcal{W} \equiv \Omega \times [0, T], \tag{1.2}$$

where $\nu > 0$ is the kinematic viscosity parameter and $\boldsymbol{f}(t, \mathbf{x})$ an external forcing mechanism. No additional fluid is created and no existing fluid is destroyed within the domain, leading to the continuity condition

$$\nabla \cdot \mathbf{u} = 0 \qquad \text{in} \quad \mathcal{W}. \tag{1.3}$$

An initial condition

$$\mathbf{u}(0, \mathbf{x}) = \mathbf{u}_0(\mathbf{x}), \quad \mathbf{x} \in \Omega \quad (\mathbf{u}_0 \quad \text{given}) \tag{1.4}$$

and the Dirichlet boundary conditions

$$\mathbf{u}(t, \mathbf{x}) = 0, \quad \mathbf{x} \in \partial\Omega, \quad \forall t, \tag{1.5}$$

known as the no-slip condition and denoted in short-hand as $\mathbf{u}(\cdot, \partial\Omega) = 0$, are added to complete the problem. The equations are non-dimensionalized, extending the range of applicability to a wide scala of physical phenomena. Each variable is the product of a specific physical scale and a primed, non-dimensional variable; $\mathbf{x} = \mathbf{x}'\hat{\ell}$, $t = t'\hat{T}$, $\mathbf{u} = \mathbf{u}'\hat{U}$, $p = p'\hat{U}^2$ and $\boldsymbol{f} = \boldsymbol{f}'\hat{T}\hat{U}^{-1}$. Applying these terms to the dimensional equations, multiplying with $\hat{\ell} = \hat{U}\hat{T}$ and dropping primes and hats, yields again equation (1.2), where ν is now replaced by the inverse of the dimensionless Reynolds number, which is defined as $Re = (U\ell/\nu)$, see also formula (1.1).
Equation (1.2) represents the so-called primitive variable formulation. Eliminating the pressure from the evolution balance, we shall mainly use the vorticity equation in the sequel. The scalar vorticity is defined as

$$\omega(t, \mathbf{x}) := (\nabla \wedge \mathbf{u}(t, \mathbf{x})) \cdot \mathbf{e}_3 = \partial_x v - \partial_y u, \tag{1.6}$$

where $\mathbf{e}_3 \perp \mathbb{R}^2$, the unit vector perpendicular to the plane. Taking the rotation of equations (1.2) and applying several vector identities yields the velocity-vorticity formulation, or vorticity equation for short,

$$\partial_t \omega + (\mathbf{u} \cdot \nabla)\omega - (1/Re)\Delta\omega = q. \tag{1.7}$$

where $q(t, \mathbf{x}) = (\nabla \wedge \boldsymbol{f}(t, \mathbf{x})) \cdot \mathbf{e}_3$. By taking the limit $\nu \to 0$, one ends up in the regime of ideal hydrodynamics, which is guided by the Euler equations

$$\frac{D\omega}{Dt} \equiv \partial_t \omega + (\mathbf{u} \cdot \nabla)\omega = q. \tag{1.8}$$

For $q = 0$ and no-slip or periodic conditions, all vorticity integrals of the form $\int_\Omega \omega^n \mathrm{d}A$ are conserved quantities of the dynamics, so-called inviscid invariants.
Finally, the stream function is a scalar potential, $\psi(t, \mathbf{x})$, related to the velocity components $u = \partial_y \psi$ and $v = -\partial_x \psi$, and to the vorticity through a Poisson equation

$$\omega = -\Delta\psi. \tag{1.9}$$

1.2.2 Function spaces and inequalities

In two dimensions the Eulerian fluid velocity $\mathbf{u}(t, \mathbf{x})$ is a real, vector-valued function, defined at position $\mathbf{x} \in \Omega \subset \mathbb{R}^2$ and time $t \in \mathbb{R}$ in some simply connected domain Ω with boundary $\partial\Omega$. In the sequel, we take Ω to be either the square domain

$$\mathcal{D} := \left\{\mathbf{x} \in \mathbb{R}^2 \mid -d/2 \le x \le d/2, -d/2 \le y \le d/2\right\}$$

with length d, or the circular domain

$$C := \left\{\mathbf{x} \in \mathbb{R}^2 \mid |\mathbf{x}| < r\right\}$$

with radius r.
Some properties of the function spaces associated to the Navier-Stokes problem with appropriate boundary conditions are recalled below. The reader is referred to the research volumes by Doering and Gibbon [35] and Foias *et al.* [49], or the monographs by Temam [137, 138], for a comprehensive overview.

Function spaces and norms

The basics are first the spaces $[C^m(\Omega)]^2$ of continuous vector-valued functions in Ω, with partial derivatives up to order m, where possibly $m = \infty$, see the classical book by Adams [2]. If one imposes the Dirichlet condition, $\mathbf{u}(\cdot, \partial\Omega) = 0$, (and $\mathbf{u}(t, \mathbf{x})$ is also zero elsewhere outside Ω), one has

$$\mathbf{u} \in [C_0^\infty(\Omega)]^2$$

and functions $\mathbf{u}(t, \mathbf{x})$ are said to have compact support.
As a next step, we assume that the spatial root-mean-square of the function $\mathbf{u}(t, \mathbf{x})$ is finite, in other words, $\mathbf{u}(t, \mathbf{x})$ is square-integrable. Such a demand is fulfilled if our function lives in the Lebesgue space $[L_2(\Omega)]^2$, which has innerproduct and norm

$$(\mathbf{u}, \mathbf{u}) := \int_\Omega \mathbf{u}(t, \mathbf{x}) \cdot \mathbf{u}(t, \mathbf{x}) \mathrm{d}A < \infty \quad \text{and} \quad \|\mathbf{u}\|_{2,\Omega} \equiv (\mathbf{u}, \mathbf{u})^{1/2},$$

where $\mathrm{d}A = \mathrm{d}x\mathrm{d}y$. The latter innerproduct represents a physically important quantity; it equals exactly twice the domain-integrated kinetic energy, $2E(t) \equiv (\mathbf{u}, \mathbf{u})$. Hence, stating that $\mathbf{u} \in L_2$, it is implicitly assumed that the kinetic energy of a flow remains finite for all times. Likewise, for the scalar vorticity one has the innerproduct

$$(\omega, \omega) := \int_\Omega \omega(t, \mathbf{x}) \omega(t, \mathbf{x}) \mathrm{d}A.$$

Again, this innerproduct has a special meaning, as it equals twice the global enstrophy of a flow, $2Z(t) \equiv (\omega, \omega)$.
Extending the Lebesgue spaces to include p-integrable functions, $[L_p(\Omega)]^2$ for $p \in [1, \infty]$, the associated norms are denoted as

$$\|\mathbf{u}\|_{p,\Omega} := \left(\int_\Omega |\mathbf{u}|^p \mathrm{d}A \right)^{1/p} < \infty,$$

and, if $p = \infty$,

$$\|\mathbf{u}\|_{\infty,\Omega} := \sup_{\mathbf{x}\in\Omega} |\mathbf{u}(\mathbf{x})|.$$

For these spaces one has $L_1 \subset L_2 \subset \ldots \subset L_\infty$ and consequently

$$\|\mathbf{u}\|_{1,\Omega} \leq \|\mathbf{u}\|_{2,\Omega} \leq \ldots \leq \|\mathbf{u}\|_{\infty,\Omega}.$$

If we now return to the Navier Stokes problem, recall that it was assumed that $\mathbf{u}(t, \mathbf{x})$ is divergence-free. The two demands on $\mathbf{u}(t, \mathbf{x})$ (square-integrability and zero-divergence) can be denoted as

$$H = \{\mathbf{u} \in [L_2(\Omega)]^2 | \nabla \cdot \mathbf{u} = 0\}.$$

However, our language should be further extended to also include p-integrability of (higher-order) derivatives of $\mathbf{u}(t, \mathbf{x})$, which is achieved with the Sobolev spaces

$$[W^{m,p}(\Omega)]^2 := \left\{ \mathbf{u} \in [L_p(\Omega)]^2 \mid D^\alpha \mathbf{u} \in [L_p(\Omega)]^2, \text{ for } 0 \leq \alpha \leq m \right\},$$

for partial derivatives $D^\alpha \mathbf{u}$ up to order m. To include the Dirichlet boundary conditions, denote by $[W_0^{m,p}(\Omega)]^2$ the closure of $C_0^\infty(\Omega)$ in $[W^{m,p}(\Omega)]^2$. Again (semi-)norms are associated to these spaces, for $1 \leq p < \infty$,

$$\|\mathbf{u}\|_{m,p,\Omega} := \left\{ \sum_{0\leq\alpha\leq m} \|D^\alpha \mathbf{u}\|_{p,\Omega}^p \right\}^{1/p} < \infty.$$

As before, a special notation is used to allow for the zero-divergence condition,

$$V = \{\mathbf{u} \in [W_0^{1,2}(\Omega)]^2 \mid \nabla \cdot \mathbf{u} = 0\}.$$

With the most important function spaces defined, we turn to a special case, driven by the presence of rigid boundaries. For $p \in [1, \infty]$ the spaces $L_p(\partial\Omega)$ include real-valued functions defined on the domain boundary $\partial\Omega$. For these spaces the norms

$$\|\cdot\|_{p,\partial\Omega} := \left(\int_{\partial\Omega} |\cdot|^p \mathrm{d}s \right)^{1/p}, \quad 1 \leq p < \infty,$$

are finite and furthermore $L_p(\partial\Omega)$ enjoys all the properties of the spaces $L_p(\Omega)$. A trace theorem relates the norms $\|\cdot\|_{m,p,\Omega}$ over functions in $W^{m,p}(\Omega)$ to $\|\cdot\|_{q,\partial\Omega}$, for $mp = n$ and $p \leq q < \infty$ one has the imbedding

$$W^{m,p}(\Omega) \to L_q(\partial\Omega),$$

where n equals the spatial dimension of Ω.

Inequalities

Related to the function spaces defined above, we recall several functional inequalities. The Hölder inequality,

$$\int_{\Omega} |uv| \mathrm{d}A \leq \left(\int_{\Omega} |u|^p \mathrm{d}A \right)^{1/p} \left(\int_{\Omega} |v|^q \mathrm{d}A \right)^{1/q},$$

for $p^{-1} + q^{-1} = 1$, where the case $p = q = 2$ corresponds to the classical Schwarz inequality.

The Poincaré-Friedrichs (P-F) inequality relates the L_2-norms of $\mathbf{u}(t, \mathbf{x})$ and its tensor gradient, $\nabla \mathbf{u}(t, \mathbf{x})$, while taking the domain-geometry into account,

$$\|\mathbf{u}\|_{2,\Omega}^2 \leq \lambda_1^{-1} \|\nabla \mathbf{u}\|_{2,\Omega}^2.$$

The constant λ_1 is the smallest eigenvalue of the negative Laplacian and for $\mathbf{u}(\cdot, \partial\Omega) = 0$, within the domain $\Omega = \mathcal{D}$ we use the estimate given by Galdi [55], $\lambda_1^{-1} \leq d^2/2\pi^2$. However, if $\Omega = \mathcal{C}$, the circular domain, this constant equals the first-zero of the zero-th order Bessel function of the first kind $\lambda_1 = (j_{0,1})^2 \simeq 5.7831$.

Now the L_2-norm of $\nabla \mathbf{u}(t, \mathbf{x})$ equals the root-mean-square vorticity, which can be shown using the continuity equation and generalized integration-by-parts,

$$\begin{aligned} \|\nabla \mathbf{u}\|_{2,\Omega}^2 &= \int_{\Omega} \Big((\partial_x u)^2 + (\partial_x v)^2 + (\partial_y u)^2 + (\partial_y v)^2 \Big) \mathrm{d}A \\ &= \int_{\Omega} \Big((\partial_x v)^2 + (\partial_y u)^2 - 2 \partial_x u \partial_y v \Big) \mathrm{d}A = \|\omega\|_{2,\Omega}^2. \end{aligned} \tag{1.10}$$

Also $\|\Delta \mathbf{u}\|_{2,\Omega}^2 = \|\nabla \omega\|_{2,\Omega}^2$, such that the P-F inequality is also applicable to the L_2-norm of the vorticity gradient. As noted by Doering and Gibbon [35], such equalities do not hold in every L_p, e.g., for $p = \infty$ one has $\|\omega\|_{\infty,\Omega} \leq \|\nabla \mathbf{u}\|_{\infty,\Omega}$.
In this respect, recall for the L_∞-norm Agmon's inequality [2],

$$\|\mathbf{u}\|_{\infty,\Omega} \leq \left(2 \|\mathbf{u}\|_{2,\Omega} \|\nabla \mathbf{u}\|_{2,\Omega} \right)^{1/2}. \tag{1.11}$$

The Young inequality can be derived from $0 \leq (a - b)^2$ and reads as

$$ab \leq \frac{\varepsilon}{p} a^p + \frac{1}{(p' \varepsilon^{p'/p})} b^{p'}$$

for all $a, b, \varepsilon > 0$ with $p \in]1, \infty[$ and $p' = p/(p-1)$.

Physical theories of turbulence usually deal with the statistical behavior of a flow and, hence, it is important to consider averages. Usually, it is tacitly assumed that ensemble averages may be replaced by combined space and time averages, whereas such an ergodicity assumption remains to be proved for the Navier-Stokes equations, see Foias [48] for a discussion. On the other hand, Foias *et al.* [49] showed how, using the

concept of asymptotic limits, the ergodicity question can be circumvented. Let us start with defining the average $a(T)$ of a time-dependent function $b(t)$, as

$$a(T) \equiv \frac{1}{T} \int_0^T b(t) \mathrm{d}t$$

The supremum limit, or largest limit point, is then denoted as

$$\langle b(t) \rangle := \limsup_{T \to \infty} a(T),$$

with the properties,

$$\limsup_{T \to \infty} |a(T)| \leq \sup_{T \geq 0} |a(T)| \quad \text{and} \quad \langle b(t) \rangle \leq \infty \; \forall \; t.$$

Now we are interested in ensemble averages, but only for the case that our statistics are stationary. Let μ be a suitable probability distribution, than equivalence of the ensemble average with respect to μ and the asymptotic limit can be shown, e.g. for the quantity $\|\mathbf{u}\|_{2,\Omega}$

$$\int \|\mathbf{u}\|_{2,\Omega} \mathrm{d}\mu(\mathbf{u}) = \langle \|\mathbf{u}\|_{2,\Omega} \rangle.$$

Because the statistics are supposed to be stationary, the average of time derivatives should be zero.

1.3 Aspects of the theory of viscous flows

Energy and degrees of freedom

We turn our attention first to the kinetic energy $E(t) := \frac{1}{2}(\mathbf{u}, \mathbf{u})$, and its evolution equation in a general domain Ω,

$$\dot{E}(t) = -\nu \|\omega\|_{2,\Omega}^2 + (\boldsymbol{f}, \mathbf{u}), \tag{1.12}$$

the L_2-innerproduct of the Navier-Stokes equations with $\mathbf{u}(t, \mathbf{x})$. Here we use the fluxie notation to denote the time-derivative of a global quantity, $\dot{a} = \mathrm{d}a/\mathrm{d}t$. Energy is supplied to the flow by means of the innerproduct $(\boldsymbol{f}, \mathbf{u})$, whereas it is destroyed by the viscous dissipation term, which scales with the mean-square vorticity, or enstrophy, $Z(t) := \frac{1}{2}(\omega, \omega)$. If no external forces are present a standard result, by the P-F inequality and formal integration over time, is the exponential energy decay,

$$E(t) \leq E(t_0) \exp{(-2\nu\lambda_1 t)}, \tag{1.13}$$

see, e.g., Foias *et al.* [49]. This fact establishes an *a priori* control over the root-mean-square velocity scale, $U \equiv \|\mathbf{u}\|_{2,\Omega} \leq \|\mathbf{u}_0\|_{2,\Omega}$ and, hence, over the integral-scale Reynolds number, Re. It does not take much imagination to realize that such a control is lost for forced flows.
Instead, the Reynolds number is replaced by the dimensionless generalized Grashof number, introduced by Foias *et al.* [50],

$$Gr := \frac{\|\boldsymbol{f}\|_{2,\Omega}}{\nu^2 \lambda_1}, \tag{1.14}$$

and named after the analogous Grashof number in Rayleigh-Bénard convection.

As mentioned in Section 1.1, our concern with the Reynolds number comes from the fact that it scales with the number of degrees of freedom, N_f, of a flow. Arguably, one of the most important discoveries in the theory of turbulence is that for a finite viscosity, $\nu > 0$, N_f is finite.
Although the heuristic KLB-theory already assumes finite dimensionality with the introduction of a minimal length scale, a first rigorous proof was established by Foias and Temam [51] and later, using different methods, by Lieb [81] and Ruelle [119]. These estimates were improved by Constantin *et al.* [30], who used the energy dissipation length $\ell_{\mathcal{E}}$, which, from dimensional analysis, has the form

$$\ell_{\mathcal{E}} = \left(\frac{\nu^3}{\lambda_1 \mathcal{E}} \right)^{1/4}$$

where the constant λ_1 arises through dimensional arguments and where the asymptotically averaged energy dissipation is defined as

$$\mathcal{E} \equiv \nu \left\langle \|\omega\|_{2,\Omega}^2 \right\rangle .$$

Hence, the number of degrees of freedom in a turbulent flow can be characterized as

$$N_f \simeq \left(\frac{d}{\ell_{\mathcal{E}}} \right)^2 .$$

An upper bound on the number N_f in terms of the parameter Gr on a no-slip domain is achieved by a classical estimate following from the energy balance (1.12) with time-independent forces $\boldsymbol{f}(\mathbf{x})$, see, e.g., Temam [136, 137]. Majorizing the right hand side of equation (1.12) with the Schwarz, P-F and Young inequalities, one obtains

$$2\dot{E}(t) + 2\nu \|\nabla \mathbf{u}\|_{2,\Omega}^2 \leq 2\|\boldsymbol{f}\|_{2,\Omega} \|\mathbf{u}\|_{2,\Omega} \leq \frac{1}{\nu\lambda_1} \|\boldsymbol{f}\|_{2,\Omega}^2 + \nu \|\nabla \mathbf{u}\|_{2,\Omega}^2 .$$

Subtracting the term $\nu\|\nabla \mathbf{u}\|_{2,\Omega}^2$ and taking averages, such that the time derivative drops out, one ends up with,

$$\nu \left\langle \|\omega\|_{2,\Omega}^2 \right\rangle \leq \nu^3 \lambda_1 Gr^2 ,$$

where we used that $\|\omega\|_{2,\Omega} = \|\nabla \mathbf{u}\|_{2,\Omega}$. Because the right hand side is defined in terms of external parameters, the latter expression is a direct bound on the number of degrees of freedom, $N_f \leq d^2 \lambda_1 Gr$. On a double periodic domain however, one has the much smaller bound

$$N_f \leq c_1 Gr^{2/3} \left(1 + \log Gr\right)^{1/3} .$$

This logarithmic correction arose first in the purely mathematical work of Constantin and Foias [30], but Ohkitani [101] showed later it could also be derived from the framework of the KLB-theory itself.

Vorticity gradients

In three spatial dimensions vortex stretching acts to generate enstrophy in the main body of the flow, a mechanism that is absent in 2D turbulence. Indeed, a whole different process takes place in 2D, as compared to the 3D evolution. Instead of the vorticity, it is the vorticity gradient $\nabla\omega(t,\mathbf{x})$ that may be amplified in the bulk of a 2D flow, by an alignment with the rate-of-strain tensor,

$$R_{ij} = \partial_{x_j} u_i + \partial_{x_i} u_j,$$

were we briefly use the index notation for vectors $\mathbf{u} = (u_1, u_2)$ and $\mathbf{x} = (x_1, x_2)$. In the inviscid integral evolution balance for the vorticity gradients one observes this alignment,

$$\dot{P}(t) = -\int_{\Omega} \partial_{x_i}\omega R_{ij} \partial_{x_j}\omega \mathrm{d}A.$$

These observations allowed the construction of KLB-theory, which is a high-wavenumber dissipation scaling theory based on the averaged enstrophy dissipation

$$\chi \equiv \nu \left\langle \|\nabla\omega\|^2_{2,\Omega} \right\rangle,$$

where the instantaneous innerproduct quantity $P(t) := \frac{1}{2}(\nabla\omega, \nabla\omega)$ is known as the palinstrophy. A minimal wavelength, below which viscosity completely rules the dynamics, can be defined on dimensional grounds,

$$\ell_\chi = \left(\frac{\nu^3}{\lambda_1 \chi}\right)^{1/6},$$

which, on a double-periodic domain, equals the KLB dissipation length ℓ_η.

Consequences of a finite domain

Whatever the set-up used to study a two-dimensional fluid flow, a maximum length is present, either because any laboratory experiment is bounded or because one has a gravest mode in a computational model. It is interesting to consider how this affects the KLB-theory, specifically in the presence of no-slip boundaries.

First of all, recall that it was hypothesized by Kraichnan [74], that the presence of a finite domain length would lead to a so-called condensation regime. Due to the inverse energy cascade a pile-up, or condensation, of energy in the largest accessible mode was expected to occur.

Recently, it was argued by Tran and Bowman [142] that a direct enstrophy cascade with a -3 exponent cannot occur on any finite domain, such that it remains a feature of turbulence on an infinite domain and KLB-theory only. The core of their argument is related to the fact that the Poincaré-Friedrichs (P-F) inequality can be applied on a finite domain. Furthermore, these authors argued that coherent vortices can only form because spectral scaling is steeper than -3 in the direct cascade range. This latter argument is the world turned upside down; usually it is assumed that the -3 cascade scaling is in itself correct while the presence of coherent structures may require some logarithmic corrections to spectral scaling, as argued by Kraichnan [75]. Simulations of a pure

Navier-Stokes flow on a double periodic domain by the same authors seems to confirm these ideas [143].

On the other hand, in a domain Ω where the velocity is equipped with the no-slip condition at the boundary $\partial\Omega$, an additional process takes place, as enstrophy may be produced at the domain walls, corresponding to the second term in the right-hand-side of the enstrophy balance,

$$\dot{Z}(t) = -\nu\|\nabla\omega\|_{2,\Omega}^2 + \nu\int_{\partial\Omega}\omega\partial_{\mathbf{n}}\omega \mathrm{d}s + (\omega, q), \tag{1.15}$$

where the unit vector $\mathbf{n} \perp \partial\Omega$. For flows on a double-periodic domain the integral over $\partial\Omega$ in the right-hand-side of balance (1.15) equals zero. Similar to the exponential energy decay there is, by the P-F inequality, an exponential enstrophy decay on a double-periodic domain when there is no external forcing present, $q = 0$. Right away, it also becomes clear that the presence of the boundary term violates the constant-flux condition on the enstrophy required in KLB-theory. Using the definition of the averaged enstrophy dissipation χ, we follow the same procedure as we used earlier for the energy equation. The aim is to obtain an averaged version of equation (1.15), for which the innerproduct term in the right-hand-side is rewritten with, respectively, the Schwarz, Young and P-F inequalities, obtaining

$$(\omega, q) \leq \|\omega\|_{2,\Omega}\|q\|_{2,\Omega} \leq \frac{\nu\lambda_1}{2}\|\omega\|_{2,\Omega}^2 + \frac{\|q\|_{2,\Omega}^2}{2\nu\lambda_1} \leq \frac{\nu}{2}\|\nabla\omega\|_{2,\Omega}^2 + \frac{\|q\|_{2,\Omega}^2}{2\nu\lambda_1}.$$

Thus applying the last line to equation (1.15) and averaging the result, one finally ends up with the balance equation

$$\chi \leq \frac{\left\langle\|q\|_{2,\Omega}^2\right\rangle}{\lambda_1\nu} + 2\nu\left\langle\int_{\partial\Omega}\omega\partial_n\omega \mathrm{d}s\right\rangle.$$

As a consequence, it is rather difficult to compare estimates of the KLB dissipation length ℓ_χ on a bounded domain with its spectral analogue ℓ_η. In fact, Foias *et al.* [49] argued that, on a no-slip domain, the classical spectral length estimate is very close to the length scale estimate used to obtain a bound on the degrees of freedom in any domain, $\ell_\mathcal{E} \simeq \ell_\eta$.

1.4 Outline of the thesis

The modest aim of this thesis is to investigate the effects of no-slip walls on forced 2D flows. In the process we hope to help bridging the large gap between wall-bounded laboratory experiments on one hand and the ideal world of theories of 2D flows on the other. Hence, we explore the properties of a forced, purely two-dimensional flow, confined by rigid walls to a simple, square geometry, where the rigid walls are emulated by the no-slip boundary condition.
The following Chapter contains a short review of the numerical tools and applied forcing schemes. The so-called route to turbulence under a stationary forcing mechanism is the theme of the third Chapter. We study, as a function of the kinematic viscosity parameter, the types of flow one encounters, progressing from a steady-state towards turbulent flows. In the fourth Chapter we examine the turbulent phenomenology of

intermediate Reynolds number flows, mainly in terms of the most important integral flow-quantities. Here, the flow is kept alive by a stochastic forcing model, resulting in a very different phenomenology as compared to the flows under stationary forcing. However, not all information on the dynamics can be extracted from domain integrated quantities and hence, local vorticity scaling behavior is studied in the fifth Chapter, by means of structure functions. The resulting scaling behavior is then compared to ideal KLB-scaling as well as scaling results for periodical domains. Finally we summarize our results in the sixth Chapter.

Chapter 2

Numerical tools

Men have become the tools of their tools
Henry D. Thoreau (1817 - 1862)

2.1 Introduction

Our main computational tool is a pseudo-spectral code solving the 2D velocity-vorticity equation on the square domain $\mathcal{D} = [-1, 1]^2$, under no-slip boundary conditions, developed by Clercx [24]. In this chapter the basic architecture of the code is briefly outlined, for details consult Clercx [24] and also Canuto *et al.* [20]. In addition, some properties of the stirring forces are discussed.

2.1.1 Layout of the numerical scheme

The set of equations to solve consists of the vorticity equation (1.7), the incompressibility condition (1.3), the no-slip boundary condition (1.5), the definition of the scalar vorticity (1.6) and an appropriate initial condition $\omega_0(\mathbf{x})$. Using some vector identities and incompressibility, Daube [34] showed that these equations are equivalent to the vorticity equation (1.7), complemented by the set

$$\begin{aligned} \Delta\mathbf{u} &= -(\nabla\omega) \wedge \mathbf{e}_3, \quad \text{in} \quad \mathcal{D} \times [0, T] \\ \omega(\cdot, \partial\mathcal{D}) &= \mathbf{e}_3 \cdot \nabla \wedge \mathbf{u}(\cdot, \partial\mathcal{D}) \\ \omega(0, \mathcal{D}) &= \mathbf{e}_3 \cdot \nabla \wedge \mathbf{u}(0, \mathcal{D}) \\ \mathbf{u}(\cdot, \partial\mathcal{D}) &= 0, \end{aligned} \tag{2.1}$$

essentially adding a Poisson equation (2.1) in each of the velocity components $u(t, \mathbf{x})$ and $v(t, \mathbf{x})$ to the problem.
A drawback is, however, that the Dirichlet condition for the velocity on $\partial\mathcal{D}$ cannot be cast into an associated condition for the vorticity. This problem is resolved by the influence matrix technique, which was originally designed by Kleiser and Schuman [73] to obtain pressure boundary conditions for the primitive variable Navier-Stokes equations. For an overview of the method, see Canuto *et al.* [20] and references therein.

Temporal discretization scheme

The code uses a semi-implicit Adams-Bashforth Crank-Nicolson (ABCN) time discretization scheme, which is more or less standard for spectral DNS codes. The nonlinear and forcing terms in the flow evolution equations are marched in time with a second-order explicit AB method, the other terms are marched in time with the implicit CN method, such that the time discretized vorticity equation reads as

$$\left(\Delta - \frac{2Re}{\delta t}\right)\omega^{n+1} = Re\left[3((\mathbf{u}\cdot\nabla)\omega + q)^n - ((\mathbf{u}\cdot\nabla)\omega + q)^{n-1}\right] - \left(\frac{2Re}{\delta t} + \Delta\right)\omega^n \qquad (2.2)$$

where δt denotes the time step and index n denotes discrete time, see also Canuto *et al.* [20]. As is immediate from the scheme, all quantities in the right-hand side are known at time n and the scheme is thus a Helmholtz equation in ω^{n+1}. Once equation (2.2) is solved, one next uses ω^{n+1} to solve the Poisson equations (2.1) in $u^{n+1}(\mathbf{x})$ and $v^{n+1}(\mathbf{x})$, reading as

$$\Delta u^{n+1}(\mathbf{x}) = -\partial_y \omega^{n+1}, \quad \Delta v^{n+1}(\mathbf{x}) = \partial_x \omega^{n+1}.$$

The loop is completed by using u^{n+1}, v^{n+1} and ω^{n+1} to solve the Helmholtz equation once more, at $n+2$.
Because the ABCN scheme is second order accurate, $\mathcal{O}(\delta t^2)$, and the earlier values u^{n-1}, v^{n-1} and ω^{n-1} are unknown at $n = 0$, the first time step uses a Runge-Kutta scheme to pertain accuracy. As we are free to 'switch-on' the forcing at a time later than $n = 0$, q^n does not have to be evaluated during the Runge-Kutta step.

Spatial discretization method

The spatial discretization scheme is a spectral method based on Chebyshev polynomials of the first kind,

$$T_n(x) = \cos(n \arccos(x)). \qquad (2.3)$$

Hence, the vorticity can be expanded as

$$\omega(t, \mathbf{x}) = \sum_{n=0}^{N}\sum_{m=0}^{M} \hat{\omega}_{mn}(t) T_n(y) T_m(x),$$

obtaining a similar expression for the velocity coefficients $\hat{\mathbf{u}}_{mn}(t)$, where the number of modes in a square domain is equal for both directions, $N = M$. The coefficients $\hat{\mathbf{u}}_{mn}(t)$ and $\hat{\omega}_{mn}(t)$ are obtained by a collocation procedure, where $\mathbf{u}(t, \mathbf{x})$ and $\omega(t, \mathbf{x})$ are evaluated at the Gauss-Lobatto grid-points (x_i, y_j)

$$x_i = \cos(i\pi/N), \quad y_j = \cos(j\pi/N), \quad \text{for} \quad 0 \le i, j \le N. \qquad (2.4)$$

Figure 2.1 shows such a non-equidistant Gauss-Lobatto collocation grid, for resolution $N = 32$. As can be seen from the Figure, the grid-point density increases towards the boundary, where the grid interval is of order $\mathcal{O}(N^{-2})$.
Transformations between physical and spectral space are executed with fast fourier

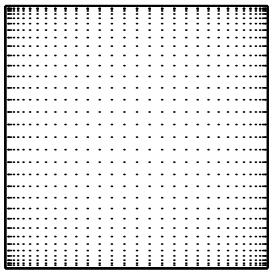

Figure 2.1: *The Gauss-Lobatto collocation grid for modest resolution ($N = 32$).*

transforms (FFT). The spectral convolutions needed to calculate the nonlinear term would require $\mathcal{O}(N^4)$ product operations, a highly undesirable by-product of any spectral method. To by-pass this effect, the nonlinear term is calculated in physical space at each of the Gauss-Lobatto points, such that the cost of multiplication is reduced to $\mathcal{O}((N \log N)^2)$ product operations, see Canuto *et al.* [20]. Even so, problems arise in the form of aliasing errors, which are solved by the so-called padding technique, developed by Orszag [103].

The boundary conditions are imposed by the Lanczos tau method. The coefficients of the two highest-order Chebyshev modes of u, v and ω in both directions are explicitly used to satisfy boundary conditions, as these modes do not contribute significantly to the total Chebyshev expansion sum, see Canuto *et al.* [20] for details.

A problem arises because no explicit boundary value for the vorticity is known *a priori*. To overcome this difficulty the vorticity value at the boundary has to be enforced by means of the influence matrix technique. Details of this technique are discussed by Daube [34] and Clercx [24], but we briefly describe it here.
In essence, with the influence matrix technique one splits the vorticity field in a particular solution and a summation of complementary solutions at the boundary points, where the corner points are excluded

$$\omega = \hat{\omega} + \sum_{i=1}^{P} \alpha_i \tilde{\omega}_i. \tag{2.5}$$

A similar expression is obtained for the velocity components. The particular solution $\hat{\omega}$ is determined by solving equation (2.2), whilst setting $\hat{\omega} = 0$ at $\partial\mathcal{D}$. Once $\hat{\omega}$ is known, a particular solution for the velocity $\hat{\mathbf{u}}$ can be determined from the Poisson equations. Now, generally speaking, the particular solution for the velocity is not divergence free, $\nabla \cdot \hat{\mathbf{u}} \neq 0$, and, if one defines $\hat{\zeta} = \mathbf{e}_3 \cdot \nabla \wedge \hat{\mathbf{u}}$, the rotation of the latter solution is not equal to the particular solution for the vorticity, $\hat{\zeta} \neq \hat{\omega}$.
Next, the complementary solutions $\tilde{\omega}_i$ are obtained by solving equation (2.2) with $\tilde{\omega}_i = \delta_{ij}$, where j refers to boundary points and δ_{ij} is the Kronecker delta function. Solving the corresponding Poisson equations yields the complementary velocity solutions $\tilde{u}_i$ and $\tilde{v}_i$.
Defining $\tilde{\zeta} = \mathbf{e}_3 \cdot \nabla \wedge \tilde{\mathbf{u}}$, one demands that the usual relation between vorticity and velocity holds on the boundary,

$$\hat{\zeta}_j - \hat{\omega}_j + \sum_{i=1}^{P} \alpha_i M_{ji} = 0 \quad \forall j \in [1, P].$$

where the influence matrix M has elements $M_{ji} = \left(\tilde{\zeta}_i - \tilde{\omega}_i\right)_j$, such that one obtains

$$\alpha_i = -\sum_{j=1}^{P} \left(M^{-1}\right)_{ij} \left(\hat{\zeta}_j - \hat{\omega}_j\right). \tag{2.6}$$

The coefficients α_i are then used to determine the value of the vorticity at the boundary, through equation (2.5), after which one solves once more equation (2.2) and the Poisson equations for the velocity components.

However, numerical instability problems arise because the highest-order Chebyshev modes are used in the procedure to determine the boundary values of the vorticity. Because the solver for the Helmholtz equation (2.2) and the Poisson equations relating the vorticity and the velocity components does not use these highest-order modes, their solutions are outside the mathematical framework described by Daube, generating errors in the form of high frequency residuals. Eventually these errors propagate to all lower order modes as well, as the modes are coupled through the equations. To overcome this problem the Tau correction is applied, in which a second set of complementary solutions $\bar{\omega}$ is added to definition (2.5), following a similar procedure for the velocity. The influence matrix technique is then extended to obtain also the coefficients for the second set of complementary solutions, but here one not only imposes the usual relation between velocity and vorticity, but additionally sets the high frequency errors equal to zero. For a detailed discussion on the removal of the high-frequency residuals, see Clercx [24].

Finally, the Helmholtz equation (2.2) and the Poisson equations are solved in spectral space. These equations can be reworked into linear matrix equations for spectral vorticity coefficients $\hat{\omega}$,

$$\mathbf{A}\hat{\omega} + \hat{\omega}\mathbf{B} = \mathbf{F},$$

which is solved with the Haidvogel-Zang algorithm [62]. Diagonalizing either $\mathbf{A}$ or $\mathbf{B}$, the N one-dimensional Helmholtz equations can be solved with recursion relations for the Chebyshev coefficients, obtaining a quasi-tridiagonal system that can be solved efficiently by a modified Thomas algorithm. The matrices $\mathbf{A}$, $\mathbf{B}$ and $\mathbf{F}$ are obtained explicitly by using the analytical forms for the partial derivatives of Chebyshev polynomials. A similar procedure is followed for the Poisson equations, see Canuto *et al.* [20] for details.

Parallel computations

Yin parallelized the available Chebyshev code, using the message passing interface (MPI) language. The parallelization of the non-linear term was based on earlier work on a Fourier code; a description can be found in [153, 154]. The core of the parallelized code is a parallel task distribution scheme; within each time loop the calculation of the non-linear term in the vorticity equation is distributed to four processors. For two spatial dimensions the arrays are hardly large enough to make further parallelization efficient, as too much time is consumed by inter-processor communication. For details, see Yin [153].
Parallel computations were executed on the TERAS, a system consisting of two 512-CPU SGI Origin 3800 systems and on the Aster, an SGI Altix 3700 system, consisting

of 416 CPUs. Both are so-called Cache-Coherent Non Uniform Memory Access machines (CC-NUMA). Memory access is non uniform (NUMA), because each processor can access its own memory faster than that of another processor. The contents of the various processor caches should be coherent (CC), however, this requires extra hardware and a cache coherency protocol.

2.1.2 A note on numerical accuracy

We start with pointing out that with spatial resolution N, we refer to the number of active modes only, ignoring the extra number of modes needed in the dealiasing procedure. Stability for the outlined discretization scheme follows from a CFL-like criterion,

$$\delta t \leq \frac{9}{N^2},$$

where N denotes the number of nodes, which appears in squared form because the grid interval near the boundary scales like $\mathcal{O}(1/N^2)$. This demand on the time-stepping is worse as compared to computations on a double periodic domain. For instance, Matthaeus *et al.* [92] report a resolution of $(512)^2$ modes, with $\delta t = 4.88 \times 10^{-4}$, whereas the same resolution on a no-slip domain requires a time step of $\delta t \simeq 3.4 \times 10^{-5}$.
To make sure all scales relevant to the dynamics of the flow are well-resolved, it was argued by Maassen [85] that the total number of grid points N_m, satisfies

$$N_m > \left(\frac{\tilde{k}_\chi}{\pi} \right)^2, \tag{2.7}$$

where $\tilde{k}_\chi$ is an instantaneous enstrophy dissipation wavenumber, defined as

$$\tilde{k}_\chi = \frac{d}{2} \left(\frac{\|\nabla \omega\|_{2,\Omega}^2}{\nu^2} \right)^{1/6}.$$

However, this practical estimate was derived for decaying flows on more or less heuristical grounds. Let us, therefore, recall what is known from rigorous mathematics. We require the definition of the number of determining nodes N_d, see Foias [48]. Say one uses a finite number of nodes m, such that

$$\int_\Omega (\mathbf{u}_1(t,m) - \mathbf{u}_2(t,m)) \, \mathrm{d}A \to 0 \quad \text{as} \quad t \to \infty, \tag{2.8}$$

where $\mathbf{u}_1(t,m)$ and $\mathbf{u}_2(t,m)$ are Galerkin projections of the velocities $\mathbf{u}_1(t,\mathbf{x})$ and $\mathbf{u}_2(t,\mathbf{x})$, each associated to a slightly different initial condition. If now the limit (2.8) implies that also

$$\int_\Omega (\mathbf{u}_1(t,\mathbf{x}) - \mathbf{u}_2(t,\mathbf{x})) \, \mathrm{d}A \to 0 \quad \text{as} \quad t \to \infty,$$

the number m equals the number of determining nodes, $m = N_d$. Unfortunately, the upper bound estimate on N_d is a lot worse than that for the degrees of freedom N_f,

which was based on $\ell_{\mathcal{E}}$ rather than ℓ_{χ}. Foias *et al.* [49] prove that, on a no-slip domain one has for domain dependent constant C_0,

$$N_d \geq C_0 Gr^2, \tag{2.9}$$

a rather depressing result from a computational point of view, that remains to be improved [49]. The relation between the different quantities is

$$N_d > N_m > N_f,$$

where N_m appears in squared form because it refers to the number of modes in one spatial direction. While no solution is established here, the preceding discussion should make clear that the computational resolution remains a complicated issue. While making sure the estimate (2.7) is obeyed, we by no means satisfy the condition (2.9) and we remain exposed to the risk of computational undersampling.

2.2 Forcing protocols

The first numerical simulations of forced two-dimensional turbulence on a double-periodic domain were presented by Lilly in 1969 [82], who used a discrete time-dependent first order Markov chain forcing protocol. In such a Markov process a limited band of wave numbers is excited, where the present state is correlated to the state at a previous time with an additional random phase component. As a physical analogue one can think of several mechanical stirring devices moving through a fluid at a slow rate in random order and with random amplitude. Much later, the Markovian forcing model was evaluated in some detail by Maltrud and Vallis [87, 88] and used by Oetzel and Vallis [100], Clercx *et al.* [26], Ishihara and Kaneda [65, 67] and, on a spherical domain, by Nozawa and Yoden [98, 99].
Other types of stochastic forcing mechanisms include white-noise-in-time Gaussian processes, applied at a single wave number by Borue [15] and over a band of wave numbers by Frisch and Sulem [54] and Smith and Yakhot [127, 128].
A much simpler, static-in-time deterministic forcing model was used in the three-dimensional periodic computations by Kida *et al.* [72] and in a two-dimensional periodic setting by Babiano *et al.* [6] and Ohkitani [102], assigning a fixed amplitude to one or several Fourier modes.
Overholt and Pope [104] designed a time-dependent deterministic forcing model, arguing that stochastic models do not perform well in simulating inertial range dynamics, whereas Wells *et al.* [151] simply applied periodic oscillations to the largest computational modes on a bounded domain.
Eswaran and Pope [38] and later Lindborg and Alvelius [4, 83], introduced remarkably complex forcing schemes to control the inner-product quantity $(\boldsymbol{f}, \mathbf{u})$, allowing the definition of a forcing defined Reynolds number. We argue, however that the number Gr is, in fact, the most general means by which the effect of an external forcing can be measured. As noted by Foias *et al.* [49], in the case of a time-dependent forcing $\boldsymbol{f}(t, \mathbf{x})$, one should use a slightly different version of the generalized Grashof number,

$$\tilde{Gr} := \left(\frac{\sup \|\boldsymbol{f}\|_{2,\Omega}}{\nu^2 \lambda_1} \right), \tag{2.10}$$

where the supremum is taken over time and $\lambda_1^{-1} \leq \left(d^2/2\pi^2\right)$, which takes into account the time-dependency of the forcing scheme.

In the sequel we use either the static-in-time single wave number forcing, or the Markov-chain forcing model. So let us first discuss these forcing protocols in detail, after which we provide the appropriate conversion formula to implement a Fourier process into a Chebyshev scheme.

Static-in-time forcing

The simplest forcing protocol is a static-in-time fixed amplitude forcing of a single Fourier wave number, where it is understood that we apply the forcing $q(\mathbf{x})$ to the vorticity equation. Exciting with a contant amplitude A_0, a single Fourier wave number, $k_f = |\mathbf{k}_f|$ one has

$$q(\mathbf{x}) = 2A_0 \left(\cos\left(k_1 x\right) + \cos\left(k_2 y\right)\right), \quad \text{for} \quad \mathbf{k}_f = (k_1, k_2), \tag{2.11}$$

of which a plot is given in Figure 2.2. Additional parameters in the forced vorticity equation are thus A_0 and k_f.

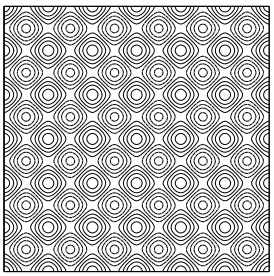

Figure 2.2: *Iso-contour plot of the forcing field $q(\mathbf{x})$, for $A_0 = 0.05$ and $k_f = 6$. Contour levels range from -1 to 1, with an interval of 0.2, where dashed lines represent negative values.*

Time-dependent Markov-chain model

In discrete-time ($n \in \mathbb{Z}^+$) notation, a first order Markov process with a complex exponential random phase and amplitude A_0,

$$q(n) = rq(n-1) + \left(1 - r^2\right)^{1/2} A_0 e^{\imath\pi\psi(n)}, \tag{2.12}$$

is weighted by the correlation coefficient r,

$$r = \frac{1 - \delta t/2\tau}{1 + \delta t/2\tau}.$$

If the diffusion timescale τ equals half the time step δt, $r = 0$ and the process becomes random-in-time, whereas $\tau \to \infty$ results in static-in-time forcing.

Here, $\psi(n) \in \mathbb{R}$ is a realization of the zero-mean Gaussian White Noise random variable Ψ. Thus $\langle\psi(n)\rangle_\Psi = 0$, where the mean $\langle\cdot\rangle_\Psi$ is taken with respect to the probability distribution of realizations, $P_\Psi(\psi)$ [112].

A continuous-time version of (2.12) is obtained by multiplying with $(1 + \delta t/2\tau)$ and some algebraic manipulation, resulting in the trapezoidal scheme approximation

$$\frac{q(n) - q(n-1)}{\delta t} = \frac{-1}{2\tau}\left(q(n) + q(n-1)\right) + \left(\frac{2}{\tau\delta t}\right)^{1/2} A_0 e^{\imath\pi\psi(n)},$$

to the first-order stochastic differential equation

$$\frac{\mathrm{d}}{\mathrm{d}t}q(t) = \frac{-1}{\tau}q(t) + \lim_{\delta t\to 0}\left(\frac{2}{\tau\delta t}\right)^{1/2} A_0 e^{\imath\pi\psi(t)},$$

which is a so-called Langevin equation. Integrating over $[0, t]$ while setting $q(0) = 0$, gives

$$q(t) = A_0 \lim_{\delta t\to 0}\left(\frac{2}{\tau\delta t}\right)^{1/2} \int_0^t e^{\imath\pi\psi(s)} e^{(s-t)/\tau}\mathrm{d}s.$$

The Markovian scheme introduces three new free parameters into the vorticity equation, A_0, τ and k_f. An example is shown in two iso-contour snapshots of $q(t, \mathbf{x})$ in Figure 2.3, for $A = 6.0$, $\tau = 0.1$ and $7 \leq k_f \leq 9$.

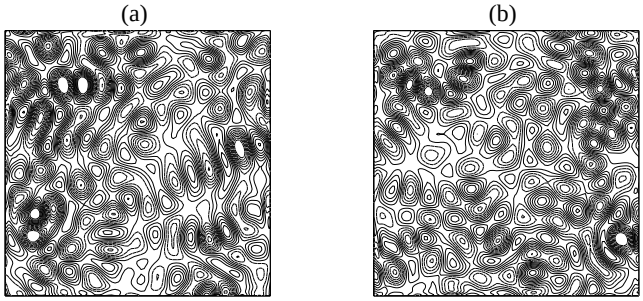

Figure 2.3: *Iso-contour plots of the forcing field $q(t, \mathbf{x})$ at $t = 450$ (a) and $t = 500$ (b), see text for details. Contour levels range from -7 to 7, with an interval of unity, where dashed lines represent negative values.*

Mapping $\boldsymbol{f}$ to q

On a double periodic domain, the scalar forcing field, q, is inserted directly into the discrete Fourier transformed vorticity equation, applying it to a spherical shell of wave numbers $|\mathbf{k}| \in [a, b]$, with $\mathbf{k} \in \mathbb{Z}^2\backslash\{0\}$. Note that the resulting (pseudo) scalar function, $q : \mathbf{k} \mapsto \mathbf{k} \times \boldsymbol{f}$, such that $q \perp \boldsymbol{f}$. Vector forcing function $\boldsymbol{f}(t, \mathbf{x}) \in \mathbb{R}^2$ is obtained with a Helmholtz decomposition

$$\boldsymbol{f} = \mathbf{k} \cdot \mathbf{v} + \mathbf{k} \times \mathbf{A} \quad \text{with} \quad \mathbf{k} \cdot \mathbf{A} = 0.$$

Because the forcing should be divergence free, $\mathbf{k} \cdot \boldsymbol{f} = 0$, one must have $\mathbf{v} = 0$, to obtain

$$\begin{aligned} q &= \mathbf{k} \times (\mathbf{k} \times \mathbf{A}) \\ &= -(\mathbf{k} \cdot \mathbf{k})\mathbf{A}, \end{aligned}$$

such that,

$$\boldsymbol{f}(t,\mathbf{k}) = -|\mathbf{k}|^{-2}\begin{vmatrix} \mathbf{e}_1 & \mathbf{e}_2 & \mathbf{e}_3 \\ k_1 & k_2 & 0 \\ 0 & 0 & q(t,\mathbf{k}) \end{vmatrix} = q(t,\mathbf{k})|\mathbf{k}|^{-2}(-k_2,k_1). \tag{2.13}$$

Conversion formula

The forcing schemes lined out above are defined in terms of Fourier wave numbers and should be converted before they can be plugged into the Chebyshev code, requiring an expansion of Fourier coefficients in Chebyshev polynomials. On the domain $\mathcal{D} := [-1,1]^2$ an arbitrary scalar function $g : \mathcal{D} \to \mathbb{R}$, has Chebyshev coefficients

$$g_{mn} = \pi^{-2} c_m c_n \int_{\mathcal{D}} g(\mathbf{x}) \frac{T_m(x)}{\sqrt{1-x^2}} \frac{T_n(y)}{\sqrt{1-y^2}} \mathrm{d}A, \quad \mathbf{x} \in \mathcal{D}. \tag{2.14}$$

Here and further on $(m,n) \in [0,M]^2 \subset \mathbb{N}^2$ and $c_m = 2 \,\forall\, m \in [1,M[$ and $c_0 = c_M = 1$, with Chebyshev polynomials of the first kind of order m given by equation (2.3). On the double-periodic domain, the scalar forcing field q was given in terms of its discrete Fourier coefficients $q(t,\mathbf{k})$, applied to a limited wave number band $|\mathbf{k}| \in [a,b]$. Thus $q(t,\mathbf{x})$ is defined as

$$q(t,\mathbf{x}) = \sum_{|\mathbf{k}|\in[a,b]} q(t,\mathbf{k}) e^{\imath \mathbf{k}\cdot\mathbf{x}}, \quad \mathbf{x} \in [0,2\pi]^2, \tag{2.15}$$

and should be substituted in (2.14). Evaluating at the Gauss-Lobatto collocation points,

$$x = \cos\theta_1, \quad y = \cos\theta_2, \quad \text{for} \quad \theta_1 = \frac{\pi m}{M}, \quad \theta_2 = \frac{\pi n}{M} \tag{2.16}$$

and using the Chebyshev polynomials (2.3) one obtains

$$g_{mn} = \pi^{-2} c_m c_n \sum_{|\mathbf{k}|\in[a,b]} q(t,\mathbf{k}) \int_{[0,\pi]^2} e^{\imath(k_1\cos\theta_1 + k_2\cos\theta_2)} \cos(m\theta_1)\cos(n\theta_2)\mathrm{d}\theta_1\mathrm{d}\theta_2. \tag{2.17}$$

This result can be rewritten using a Jacobi-Anger expansion, see e.g., Arfken [5]

$$e^{\imath k_1 \cos\theta_1} = J_0(k_1) + 2\sum_{l\in\mathbb{N}} \imath^l J_l(k_1)\cos(l\theta_1),$$

where $J_l(k_1)$, is the l^{th} order Bessel function of the first kind again, see e.g., Arfken [5]. Using the orthogonality property of the cosine function

$$\pi^{-1}\int_0^\pi \cos(l\theta_1)\cos(m\theta_1)\mathrm{d}\theta_1 = \tfrac{1}{2}\delta_{lm},$$

where δ_{lm} denotes the Kronecker delta, the integrals in (2.17) can now be determined component wise;

$$\pi^{-1}\int_0^\pi e^{\imath k_j\cos\theta_j}\cos(m\theta_j)\mathrm{d}\theta_j = \imath^m J_m(k_j) \quad j = 1,2.$$

Henceforth, entries in the Chebyshev coefficient matrix are expressed as a summation over Fourier coefficients and Bessel functions

$$g_{mn} = c_m c_n \sum_{|\mathbf{k}| \in [a,b]} q(t, \mathbf{k}) \imath^{m+n} J_m(k_1) J_n(k_2), \tag{2.18}$$

where $c_0 = 1$ and $c_m = 2 \, \forall \, m \in [1, M]$. Finally, (2.18) can be decoupled in even-even to odd-odd Chebyshev modes, to ensure an efficient numerical algorithm [24].

Chapter 3

Roadmap to chaotic flow

Never make anything simple and efficient when a way can be found
to make it complex and wonderful.
Anonymous

3.1 Introduction

Of general interest is the behavior at large times, $t \to \infty$, of any solution $\omega(t, \mathbf{x})$ to the two-dimensional vorticity equation as a function of a physical parameter ϵ. Suppose, for now, that the value of this parameter determines the strength of some external forcing mechanism. Gradually increasing the value of ϵ, one expects to encounter a sequence of markedly different flows. At the extremes, the smallest parameter values lead to stationary solutions $\omega(\mathbf{x})$ and sufficiently high values lead to turbulence. However, the phenomenological road connecting these extremes is not generally known.
Originally, the discussion was brought alive by Landau [76], who reasoned that the complexity of a fluid flow would build-up for increasing values of ϵ as follows:

$$\text{steady} \to \text{periodic} \to \text{2-periodic} \to \ldots \to n\text{-periodic},$$

where each transition is a Hopf-bifurcation that adds another frequency to the flow; an n-periodic motion thus contains n independent frequencies. Landau conjectured that turbulence is a limit state of quasi-periodic motion with an ever-increasing number of frequencies, where $n \to \infty$ as $\epsilon \to \infty$.
However, Newhouse, Ruelle and Takens [120, 96] argued that the above picture is probably incorrect; quasi-periodic motion seems to be a non-generic property of dissipative dynamical systems, implying that these motions may not occur at all. (Their precise argument states that 3-periodic motion is unstable to small C^2-perturbations, whereas 4-periodic motion is unstable to small C^∞-perturbations). Rather, before reaching the limit $\epsilon \to \infty$ one would observe that the flow becomes chaotic and lies on a 'strange attractor', an attracting set with a specific geometrical structure, see, e.g., the overview by Ruelle [118]. This implies furthermore that the frequency spectrum is no longer discrete, with separate peaks at the excited frequencies, but that it has become continuous with a high noise-level.

Let us, before reviewing some results known from the literature, give an example of the different types of motion, mentioned above. Usually one observes a system in the

form of time series, even though the behavior of, e.g. a fluid flow represents a spatio-temporal system, time series measured somewhere within the system may give a good idea of its total behavior. In Figure 3.1 we show a sequence of four different types of motion in time, where the signals were created artificially. Units on the axes are lacking, as we are only interested in the form of the signals and not so much in quantifying the systems we consider. The first two plots in the sequence are familiar and unexciting if one is interested in dynamics. Figure 3.1(a) shows a stationary state where nothing changes in time, whereas Figure 3.1(b) displays a purely periodic signal, in this case a sine. However, Figure 3.1(c) shows already a stranger behavior; it is the result of adding two sines with a fundamentally different frequency (in this case $f_0 = 2.2$ and $f_1 = 1/3$) and is a form of the quasi-periodic motion mentioned by Landau [76]. Then, Figure 3.1(d) displays a chaotic signal that cannot be mimicked by a superposition of periodic signals, it looks random, yet some order can be distinguished. In fact, it is the output signal of the logistic equation, see e.g. Verhulst [147] for details,

$$y_n = A y_{n-1} \left(1 - y_{n-1}\right),$$

where the present value of the system y_n depends on the previous value y_{n-1} in a non-linear (quadratic) way. The value of the control-parameter A determines what type of behavior results, several regimes can be identified and in this specific case we used the value $A = 3.9$, which is in the chaotic regime.

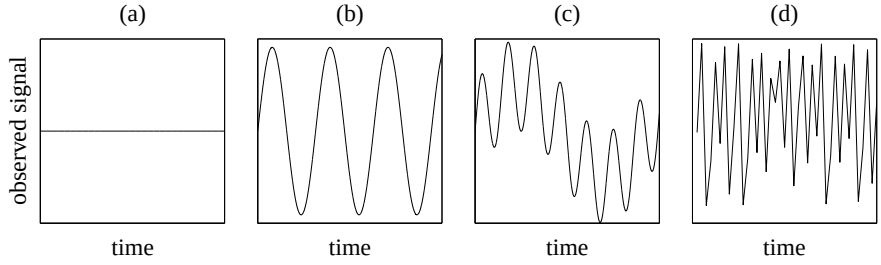

Figure 3.1: *Artificial signals showing stationary (a), periodic (b), double-periodic (c) and chaotic (d) behavior.*

So let us now return to what is known for the behavior of fluid flows. While no experimental evidence was ever found for Landau's conjecture, Ruelle-Takens-Newhouse scenarios were observed in various degrees of accuracy in Rayleigh-Bénard convection experiment, see Ahlers [3], Swinney and Gollub [60, 132], Gollub and Benson [59] and Libchaber *et al.* [80], and in Taylor-Couette experiments, see Brandstäter *et al.* [17].

However, in their convection experiments Libchaber *et al.* also observed phase-locking, where the ratio of the fundamental frequencies in a 2-periodic flow locks to the same rational number until the system becomes chaotic, a phenomenon unexplained by Ruelle-Takens-Newhouse theory. Furthermore, Walden *et al.* [149] recorded quasi-periodic motion with four and even five independent frequencies in a Rayleigh-Bénard convection experiment, showing that the Hopf bifurcation leading from quasi-periodicity to chaos may not always occur. Also in electromagnetically forced quasi two-dimensional (2D) flows of large aspect ratio studied by Tabeling *et al.* [134] no clear evidence for

the Ruelle-Takens scenario was found. For these latter flows, the transition sequence depended on the initial number of driven vortices.
Based on early observations of the phase-locking phenomenon, Feigenbaum [45, 46] sketched the route to chaos in terms of an infinite cascade of period-doubling bifurcations. One should thus observe a (quasi-)periodic state in which more and more subharmonics of the base frequency are added to the flow for each parameter change, until the system reaches chaos. Subsequently, the Feigenbaum scenario was observed in several Rayleigh-Bénard convection experiments, by Gollub and Benson [59], Giglio *et al.* [57] and, for low Chandrasekhar numbers, by Libchaber *et al.* [80]. However, a system may not be confined to a single route to chaos. Indeed, in two-parameter Rayleigh-Bénard problems, as studied by Libchaber *et al.* and by Gollub and Benson, or Taylor-Couette flows as studied by Buzug *et al.* [19] and Pfister *et al.* [108], several routes to chaos may exist side by side, whereas hybrid behavior can also occur.

On the computational side, following the ground-breaking work of Lorenz [84], numerical experiments were largely based on finite mode truncations of the Navier-Stokes equations, leading to systems of coupled ordinary differential equations, see Gallavotti [56] for an overview. It is, however, uncertain how such truncated solutions relate to full Navier-Stokes solutions, as it was shown by Treve and Manley [145] that the chaos observed in the severely truncated Lorenz model is a consequence of its small number of modes, rather than its dynamics. On the other hand, a study of the Lorenz model gave rise to a whole new road-to-turbulence theory, proposed by Manneville and Pomeau [89, 90]. These authors observed how ordered, periodic behavior, or laminar flow, was disturbed in irregular intervals by violent events, known as bursts, in which the system takes on a chaotic appearance. Gradually, as the guiding parameter is changed, the intermittent bursts become more and more frequent, until the systems is fully chaotic. Such behavior was also observed by Gollub and Benson [59] in a convection experiment, at about the same time the associated intermittency-theory was developed, and by Dubois *et al.* [36].
Kida *et al.* [72] expored the road to turbulence as a one-parameter problem in a three-dimensional periodic domain by means of DNS. Decreasing the value of the viscosity parameter under constant forcing revealed a remarkably complex behavior, including low and high dimensional chaotic motions and finally turbulence. Not surprisingly, due to the complexity of the guiding equations, the transition sequence observed by these authors did not correspond directly to any theory, although some resemblance was seen to occur with the earlier experimental work of Walden *et al.* [149]. Feudel and Seehafer [47] presented data from 2D DNS experiments on a periodic domain, where the amplitude of an external forcing served as control parameter, observing transition sequence which included phase locking phenomena and travelling waves. Applying stress-free boundary conditions in one and periodic conditions in the other direction Braun *et al.* [18] mimicked the laboratory experiments of Tabeling *et al.* with purely 2D computations. For these large aspect ratio flows a period doubling cascade to chaos was observed.

Finally, a reminder that chaos is not turbulence. Where the latter is generally agreed to possess a very large number of degrees of freedom, it was shown by Lorenz [84] that chaos may occur for as little as three degrees of freedom. Low-dimensional chaos in no way explains the high-dimensional turbulence, but may be encountered as a pre-turbulent state.

Route to turbulence in a finite 2D domain

The present chapter is mainly inspired by the work of Kida *et al.* [72], exploring the phenomenology of a continuously forced viscous flow as a function of the kinematic viscosity parameter ν. Applying the no-slip boundary conditions on the velocity, the value of ν is progressively decreased in a series of DNS experiments on a square domain. To keep matters simple, we use the time-independent single wavenumber forcing described in Section 2.2, keeping the forcing amplitude and wavenumber fixed at $A_0 = 0.05$ and $k_f = 6$. This set-up corresponds to a chess-board pattern of 36 driven vortices of alternating sign. Zero-vorticity initial conditions are applied, to make sure the resulting phenomenology arises due to the action of the forcing only.

The overall transition sequence for decreasing values of the kinematic viscosity parameter down to $\nu = 1/5000$ can, roughly speaking, be summed up as follows;

$$\text{steady} \rightarrow \text{periodic} \rightarrow \text{quasi-periodic} \rightarrow \text{chaos} \rightarrow \text{intermittent} \rightarrow \text{chaos}.$$

Essentially, the route to chaos is a two-parameter problem, depending on both the forcing wavenumber and the kinematic viscosity parameter, but for convenience, we cast these into a single control or bifurcation parameter, $\nu' = (1/\nu k_f)$. In this way we obtain a sequence of increasing values, where $\nu = 1/5000$ corresponds to the maximum value $\nu' = 833.3$. Starting with low values of ν', the flow changes from a steady state to periodic and quasi-periodic motion before the system enters its first chaotic state. These different states of motion refer to the spatio-temporal behavior of the flow but are most clearly recognized in measured time series of, e.g., the value of the vorticity at a given point in the domain. This part of the sequence corresponds neatly to the Ruelle-Takens scenario described before, our results are reported in Molenaar *et al.* [94].
During the first chaotic state measured signals are irregular, but of similar amplitude as compared to the preceding periodic motions. If, however, the value of the control parameter is further increased the first chaotic state is disturbed by progressively more frequent and violent events, known as intermittent bursts, during which the measured signal may have a much larger amplitude than usual. Such a behavior is generically known as intermittency and hence the second part of the transition sequence is more like a complicated form of the Manneville-Pomeau intermittency scenario. Finally these bursts push the system into a second chaotic state.

Chapter outline

The roadmap to the rest of this chapter is as follows; Section 3.2 is devoted to several aspects of the stationary solutions and Section 3.3 gives an overview of the time-dependent solutions, where periodic solutions are discussed in more detail in Section 3.4 and intermittent solutions in Section 3.5. We end the chapter with a stability analysis of the system with respect to small initial perturbations and sensitivity to changes in computational resolution in Section 3.6. The introduction proceeds next with a short summary on aspects of nonlinear dynamical systems theory and an overview of several tools required for their analysis.

3.1.1 Non-linear dynamical systems

Some elements of nonlinear dynamical systems are summed up here in a brief synthesis, the reader is referred to, e.g., Doering and Gibbon [35], Temam [138] or Verhulst [147] for details. A dynamical system is autonomous if it can be described by the set of ordinary differential equations

$$\frac{\mathrm{d}\mathbf{x}}{\mathrm{d}t} = \boldsymbol{g}(t, \mathbf{x}, \epsilon), \tag{3.1}$$

where ϵ is a control-parameter, $\mathbf{x}$ the n-dimensional state vector and $\boldsymbol{g}$ a sufficiently smooth vector field. In phase space, that is, in the n-dimensional space containing all possible system states, the long-term behavior of the system is known as its local attractor. The collection of all these states associated to all admissible initial conditions is known as the global attractor and denoted by $\mathcal{A}$. In other words, $\mathcal{A}$ is the set towards which all solutions from all possible initial conditions converge in due time. Although the global attractor is an abstract mathematical concept, its importance is immediately clear if one realizes that its 'dimension' is directly related to N_f, the number of degrees of freedom in the system, see, e.g., Robinson [114],

$$N_f \sim D_{frac}(\mathcal{A}).$$

Here the fractal dimension, also known as the box-counting dimension or limit capacity, is defined as

$$D_{frac}(\mathcal{A}) \equiv \limsup_{\delta \to 0} \frac{\log N(\mathcal{A}, \delta)}{\log(1/\delta)}, \tag{3.2}$$

where $N(\mathcal{A}, \delta)$ is the number of balls, of radius $\delta > 0$, needed to cover $\mathcal{A}$. Thus $D_{frac}(\mathcal{A})$ counts the number of balls of radius δ that each contain one point of $\mathcal{A}$.
The simplest local attractor is a fixed point, or steady state (S). Referring back to the notation in equation (3.1), a fixed point simply corresponds to $\boldsymbol{g}(\mathbf{x}, \epsilon) = 0$, where the control parameter is smaller than some limit value, $\epsilon < c_2$. Instead of a single stationary state, a sequence of such states may exist, denoted as S^I, S^{II}, ..., S^N, associated to different values of the control parameter.
The transition to time-dependent motion, due to small changes in the control parameter, is denoted as, $S \to P$, in this particular case known as a Hopf bifurcation, leading to a limit cycle, or periodic behavior with one fundamental frequency (P). Quasi-periodic motion is denoted as QP_n, where n corresponds to the number of excited incommensurate frequencies, where the transition $P \to QP_2$ is a secondary Hopf, or Neimark-Sacker bifurcation. For QP_2, phase space trajectories lie on a 2-torus, a donut shape, and for QP_n, $n > 2$ on a hyper-torus. Chaotic motion is denoted with C^I and C^{II}, where the former indicates a low- and the latter a high-dimensional motion. The transition $QP_3 \to C$ corresponds to the break-up of a 3-torus into a so-called chaotic attractor, e.g., the product of a Cantor set with an interval of $\mathbb{R}$ [120].

3.1.2 Tools of the trade: analysis of computational data

It may be somewhat confusing in the following Sections that the analysis of a dynamical system exhibiting a complex spatio-temporal behavior is largely based on temporal observations (time series). This approach is only possible due to an important theorem by Takens, see also the earlier work of Farmer [44] and the Navier-Stokes related discussion by Robinson [114], stating that the system dynamics can be recovered from

time-delayed point-measurements. Hence, we briefly discuss the analysis techniques applied to our computational data. Again, our overview is far from exhaustive and the reader is referred to, e.g., Mullin [95], Schuster [126], Abarbanel [1] or Thompson and Stewart [140] for details.

A first indication of the behavior encountered in experiments is, apart from a visual inspection of the measured time series itself, the corresponding discrete power spectrum $P_s(f)$. For an arbitrary function $g(n)$, measured at discrete time n, the power spectrum at frequency $f = (n/N\Delta t)$, where Δt is the sampling time, is denoted as

$$P_s(f) = \lim_{N\to\infty} \left| \sum_{n=0}^{N-1} g(n) e^{-if} \right|^2 .$$

Typically, a data sequence is divided in overlapping blocks of N-points for each of which $P_s(f)$ is estimated. The overall spectrum is the average of these separate power spectra, with resolution $f_\Delta = (1/N\Delta t)$. The maximum or Nyquist frequency is $f_{Nyq} = 2/\Delta t$. Periodic motion results in a distinct peak in the power spectrum, with each additional period adding another spectral peak, whereas chaotic behavior leads to a broadband spectrum.
Note that every spectral peak is necessarily an integer multiple of f_Δ and the ratio of two peaks will always be a rational number, $f_1/f_2 = p/q \in \mathbb{Q}$. But in a quasi-periodic motion two or more incommensurate frequencies occur, that is, frequencies for which $f_1 = \alpha f_2$, such that $\alpha \notin \mathbb{Q}$. Some extra testing is thus needed to determine the nature of the periodic behavior. To gain a better understanding of the system, we have

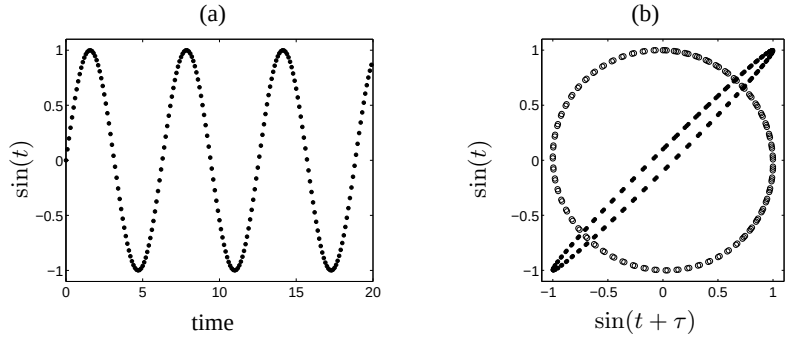

Figure 3.2: *A sample time series (a) and its phase portrait for two different lags, $\tau = \Delta t$ (solid circles) and $\tau = 16\Delta t$ (circles) (b).*

to reconstruct its phase-space behavior. As mentioned before, the motion of the system trajectories through phase-space can be reconstructed from a measured time series by the delayed embedding technique, a method devised by Packard *et al.* [105] and Roux *et al.* [117]. In two dimensions one plots a time series $X(n)$ against a delayed version of itself $X(n + \tau)$. The lag $\tau = m\Delta t$, for integer m and sampling time Δt, corresponds to a local minimum in the average mutual information, $\min_i(I(\tau))$, where $i = 1$ denotes the first and $i = 2$ the second minimum. Using the scheme by Fraser and Swinney [52], see also Abarbanel [1], the average mutual information is a measure

of the predictability of observation $X(n+\tau)$, given the earlier observation $X(n)$,

$$I(\tau) = \sum_{X(n),X(n+\tau)} P(X(n), X(n+\tau)) \log_2 \left(\frac{P(X(n), X(n+\tau))}{P(X(n))P(X(n+\tau))} \right).$$

$P(X(n), X(n+\tau))$ is the joint probability density function (PDF) for measurements taken at n and $n+\tau$ to result in values $X(n)$ and $X(n+\tau)$, whereas the individual PDFs for $X(n)$ and $X(n+\tau)$ are denoted by $P(X(n))$ and $P(X(n+\tau))$. If two measurements are completely independent the mutual information equals zero, $I(\tau) = 0$. To check the sensitivity of the resulting embedding with respect to the applied delay, a comparison was made with the delay set at $\min_2(I(\tau))$, the second local minimum of $I(\tau)$. In general, these larger delay times yielded no additional information on the phase space behavior. For a sample time series, Figure 3.2(a), we show the effect of choosing a different time lag in the corresponding phase portrait, Figure 3.2(b). Clearly, the lag $\tau = \Delta t$ yields insufficient information and a distorted phase portrait, one would expect the phase portrait of a sinusoidal signal to describe a circle, as is the case for $\tau = 16\Delta t$. Note that neither the circle nor the ellipsoid are completely filled with points, as we used only a short time series.

The integer embedding dimension of the attractor, D_{emb}, is likely to be higher than two. Hence, one should determine the integer value $D_{emb} = m$ at which the attractor is completely unfolded. That is, if the attractor is mapped by coordinates $\mathbf{X}_m(n) = (X(n), X(n+\tau), \ldots, X(n+m\tau))$, which integer m is required to conserve its topology correctly?
To answer this question, one can apply the global false nearest neighbor technique (FFN), developed by Kennel *et al.* [71]. In short, with FFN one compares if the nearest neighbor to a point in a phase space of dimension $D_{emb} = m-1$, remains a nearest neighbor if $D_{emb} = m$. If this is not the case, the proximity for $D_{emb} = m-1$ was not caused by the dynamics, but rather by an insufficient unfolding of the attractor and the points are false nearest neighbors. Hence, one compares the Euclidian distance of the nearest neighbors $\mathbf{X}_{m-1}(n)$ and $\mathbf{Y}_{m-1}(n)$ in dimension $m-1$ to their distance in dimension m,

$$R_m(n) = \frac{|X(n+m\tau) - Y(n+m\tau)|}{\|\mathbf{X}_{m-1}(n) - \mathbf{Y}_{m-1}(n)\|},$$

where $\|\cdot\|$ is the Euclidian norm. A threshold value must be defined which $R_m(n)$ should exceed to identify a false nearest neighbor. Here we follow the suggestion by Abarbanel [1] that $R_m(n) > 15$, whereas a consistency check was made with $R_m(n) > 10$. Once the fraction of false nearest neighbors reaches zero for dimension m, it remains zero for all $n > m$ and one has unfolded the attractor at embedding dimension $D_{emb} = m$.

The actual dimension of the system is by no means required to be integer. In fact it is likely to be non-integer, or fractal. In the previous Subsection we introduced the fractal dimension D_{frac}, as the true dimension of the global attractor. Several other definitions of dimension exist, and in our analysis we use the correlation dimension D_{corr}, a refinement of D_{frac}, which rather estimates the collection of N cubes of side δ, such that the chances p_i of finding independently two phase space points in the same cube add up to a cumulative minimum $P(\mathcal{A}, \delta)$,

$$D_{corr}(\mathcal{A}) \equiv \limsup_{\delta \to 0} \frac{\log P(\mathcal{A}, \delta)}{\log(\delta)}, \tag{3.3}$$

where

$$P(\mathcal{A}, \delta) = \sum_{i=1}^{N} p_i^2.$$

As one considers correlation integrals for each pair of points in phase space, the distance between these points should be a consequence of the phase space geometry only. Because the phase space is reconstructed from a single time series, temporally correlated points should thus be excluded from the analysis, as these would bias the estimate of the correlation integral. Thus a suitable temporal lag Δl, known as the Theiler window, has to be taken between adjacent pairs in a time series during the calculation of D_{corr}, see Provenzale *et al.* [111] for details. Provenzale *et al.* argued that a reasonable estimate for the Theiler window comes from the space-time separation plot. This latter plot displays, for an m-dimensional phase space, contours of the fraction of points closer than separation distance r in phase space as a function of the temporal window Δl. In each case several values were used for Δl, to test for convergence of results.

Embedding a point-measured time series in m-dimensional phase space, the Poincaré section plots the intersection of phase space trajectories with a hyperplane of dimension $m - 1$, for crossings of the same sign. Each next point $\mathbf{y}$ in the Poincaré section is the image of a previous point $\mathbf{x}$ under action of the Poincaré return map, that is, $P : \mathbf{x} \mapsto \mathbf{y}$. We use an algorithm developed by Hegger *et al.* [63], to produce these sections. If the system follows a limit cycle a linear approximation P' can be made in the vicinity of the fixed point,

$$\tilde{\mathbf{x}} = P(\tilde{\mathbf{x}}),$$

through which the limit cycle crosses the hyperplane, see Thompson and Stewart [140]. For an attracting limit cycle the eigenvalues of P' lie within the unit circle and progressive crossings of the hyperplane asymptotically approach $\tilde{\mathbf{x}}$, see Figure 3.3. Such limit cycles are structurally stable; small perturbation of the system lead to the same behavior.

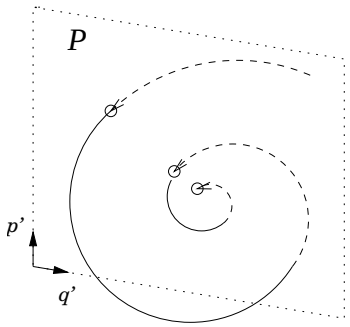

Figure 3.3: *A trajectory spiralling towards a fixed-point in three-dimensional phase-space. The intersections with the Poincaré plane P, spanned by p' and q', reveal the structure of the system attractor.*

On the other hand, when the system becomes chaotic, structure is lost in the Poincaré section. To determine the extent of the chaos one can measuring how fast phase space trajectories diverge, which requires an estimate of the largest Lyapunov exponent ϕ_{max}. Ideally, one would like to measure the complete Lyapunov spectrum, but for higher dimensional systems this is very hard to achieve. Instead one can use ϕ_{max}, assuming the average separation $d(t)$ of trajectories as a function of time is exponential,

such that

$$d(t) = c_0 e^{\phi_{max} t},$$

where c_0 is a constant that normalizes the initial separation. On the other hand, dimension estimates, like D_{corr}, give an idea of the complexity of he system. To estimate ϕ_{max} and D_{corr} we use a method and software developed by Rosenberg *et al.* [115, 116], who also explain why one should rather estimate ϕ_{max} than quantify chaos by the popular Grassberger-Procaccia algorithm [61].

Since Wolf *et al.* [152] applied a method for calculating Lyapunov exponents to a Taylor-Couette experiment, debate followed on the validity of estimates for such high-dimensional systems as fluid flows. Indeed, there seem to be severe constraints on the estimates of both D_{corr} and ϕ_{max}. Without repeating the technical details here, Eckmann and Ruelle [37] showed that the number of points N in a time series, required to provide a reliable estimate of these quantities is, respectively,

$$N > 10^{D_{corr}/2} \quad \text{and} \quad N > 10^{D_{emb}}.$$

Clearly, these conditions generate problems for the analysis of higher dimensional chaotic or turbulent motions. Considering the high spatial resolution required at high Reynolds numbers, such lengthy time series are far beyond present-day computational resources. On the other hand, as was already noted by Brandstäter *et al.* [17], while the system has a very high dimensional phase space, the actual motion may yet be confined to a relatively low dimensional attractor. The time series in our analysis are in the range up to $N \leq 60000$, dimension estimates above $D_{corr} = 9.3$ and estimates of ϕ_{max} for $D_{emb} > 4$ are thus unreliable.

3.2 Stationary solutions

For values of the control parameter $\nu' \leq 125.0$, the computational solutions converge to steady states, see Figure 3.4. At parameter value $\nu' = 83.3$ the flow field essentially equals the forcing field, a checkerboard pattern of 36 monopolar vortices of alternating sign. This field preserves all the rotation and reflection symmetries of the square, forming the dihedral symmetry group $\mathbf{D}_4$. However, for $\nu' = 100.0$ a symmetry breaking pitchfork bifurcation[1] has changed the flow configuration to a large circulation cell, which fills the interior of the domain, with small secondary vortices at fixed locations near the corners. The reflection symmetries are broken, but not the rotational symmetries, forming the subgroup $\mathbf{Z}_4 \subset \mathbf{D}_4$.

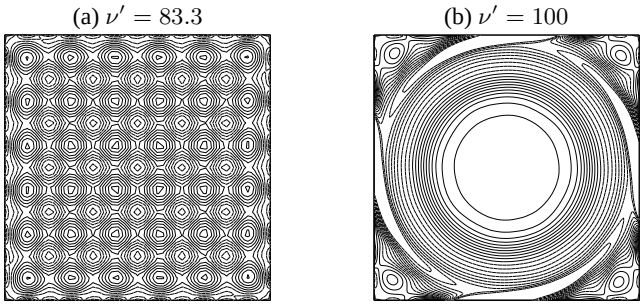

Figure 3.4: *Normalized iso-vorticity plots for $\nu' = 83.3$ (a) and $\nu' = 100$ (b), carrying $\mathbf{D}_4$ and $\mathbf{Z}_4$ symmetry respectively, where contours range from -1 to 1 with an interval of 1 and dashed lines represent negative values.*

Let us suppose that the observed solutions are time-independent, but that the inertial term in the evolution equation is no longer negligible as compared to the dissipation and forcing terms. For this case we want to get some idea about the stability of the non-homogeneous stationary solutions with respect to time-dependent perturbations of small amplitude. The stability is determined with the energy method, consult e.g. Doering and Gibbon [35] for details. For once we do not consider the vorticity equation, but rather the original Navier-Stokes equation, with stationary solution $\mathbf{U}(\mathbf{x})$ and perturbation $\tilde{\mathbf{u}}(t, \mathbf{x})$, to avoid the integrals over the boundary that arise in the enstrophy equation. The velocity-pressure pair $\mathbf{U}(\mathbf{x})$, $P(\mathbf{x})$ is a fixed point in phase space and the equation of motion reads as

$$\mathbf{U} \cdot \nabla \mathbf{U} + \nabla P = \nu \Delta \mathbf{U} + \boldsymbol{f},$$

where it also holds that $\nabla \cdot \mathbf{U} = 0$. Taking the domain-integrated innerproduct of this latter equation with $\mathbf{U}$, the energy equation reads as

$$(\nabla \mathbf{U}, \nabla \mathbf{U}) = \nu^{-1}(\boldsymbol{f}, \mathbf{U}),$$

where we can rearrange the innerproduct in the right-hand-side with the Schwarz and P-F inequalities and the generalized Grashof number (1.14) respectively,

$$\nu^{-1}(\boldsymbol{f}, \mathbf{U}) \leq \|\nabla \mathbf{U}\|_{2,\mathcal{D}} \frac{\|\boldsymbol{f}\|_{2,\mathcal{D}}}{\lambda_1^{1/2} \nu} = \nu \lambda_1^{1/2} Gr \|\nabla \mathbf{U}\|_{2,\mathcal{D}}.$$

[1] That is, if such a bifurcation is compatible with the Navier-Stokes equations, see Saut and Temam [125].

Now with $\|\nabla\mathbf{U}\|_{2,\mathcal{D}}^2 = (\nabla\mathbf{U}, \nabla\mathbf{U})$, combining the last two lines, one has by Agmon's inequality (1.11)

$$\nu\lambda_1^{1/2}Gr \geq \|\nabla\mathbf{U}\|_{2,\mathcal{D}} \geq \lambda_1^{1/4}\left(\|\mathbf{U}\|_{2,\mathcal{D}}\|\nabla\mathbf{U}\|_{2,\mathcal{D}}\right)^{1/2} \geq \frac{\lambda_1^{1/4}}{\sqrt{2}}\|\mathbf{U}\|_{\infty,\mathcal{D}}.$$

We proceed with the introduction of small perturbations, which are added to the stationary velocity and pressure fields

$$\begin{aligned}\mathbf{u}(t,\mathbf{x}) &= \mathbf{U}(\mathbf{x}) + \tilde{\mathbf{u}}(t,\mathbf{x})\\ p(t,\mathbf{x}) &= P(\mathbf{x}) + \tilde{p}(t,\mathbf{x})\end{aligned}$$

and which satisfy

$$\begin{aligned}\partial_t\tilde{\mathbf{u}} + \tilde{\mathbf{u}}\cdot\nabla\tilde{\mathbf{u}} + \mathbf{U}\cdot\nabla\tilde{\mathbf{u}} + \tilde{\mathbf{u}}\cdot\nabla\mathbf{U} &= -\nabla\tilde{p} + \nu\Delta\tilde{\mathbf{u}}\\ \nabla\cdot\tilde{\mathbf{u}} &= 0,\end{aligned}$$

together with the appropriate boundary condition $\tilde{\mathbf{u}}(\cdot,\partial\mathcal{D}) = 0$. A sufficient stability criterion is that the energy of the perturbation vanishes for $t\to\infty$, which can be established from the energy balance

$$\frac{\mathrm{d}}{\mathrm{d}t}\tfrac{1}{2}\|\tilde{\mathbf{u}}\|_{2,\mathcal{D}}^2 = -\nu\|\nabla\tilde{\mathbf{u}}\|_{2,\mathcal{D}}^2 - \int_{\mathcal{D}}(\tilde{\mathbf{u}}\cdot\nabla\mathbf{U})\cdot\tilde{\mathbf{u}}\mathrm{d}A.$$

The problem is now that the right hand side should not exceed the negative perturbation-energy $-\|\tilde{\mathbf{u}}\|_{2,\mathcal{D}}^2$, to guarantee an exponential decay in time and ensure stability,

$$-2\nu\|\nabla\tilde{\mathbf{u}}\|_{2,\mathcal{D}}^2 - 2\int_{\mathcal{D}}(\tilde{\mathbf{u}}\cdot\nabla\mathbf{U})\cdot\tilde{\mathbf{u}}\mathrm{d}A \leq -\|\tilde{\mathbf{u}}\|_{2,\mathcal{D}}^2. \tag{3.4}$$

Note that, by generalized partial integration, the Hölder inequality and our earlier estimate, we obtain

$$\begin{aligned}-2\int_{\mathcal{D}}(\tilde{\mathbf{u}}\cdot\nabla\mathbf{U})\cdot\tilde{\mathbf{u}}\mathrm{d}A &= 2\int_{\mathcal{D}}\mathbf{U}\cdot\tilde{\mathbf{u}}\cdot(\nabla\tilde{\mathbf{u}})\mathrm{d}A\\ &\leq 2\|\mathbf{U}(\mathbf{x})\|_{\infty,\mathcal{D}}\|\tilde{\mathbf{u}}\|_{2,\mathcal{D}}\|\nabla\tilde{\mathbf{u}}\|_{2,\mathcal{D}}\\ &\leq 2\lambda_1^{-1/2}\|\mathbf{U}(\mathbf{x})\|_{\infty,\mathcal{D}}\|\nabla\tilde{\mathbf{u}}\|_{2,\mathcal{D}}^2\\ &\leq \frac{2\nu\sqrt{2}}{\lambda_1^{1/4}}Gr\|\nabla\tilde{\mathbf{u}}\|_{2,\mathcal{D}}^2.\end{aligned} \tag{3.5}$$

Now we search for the smallest value of the quantity

$$\frac{2\nu\|\nabla\tilde{\mathbf{u}}\|_{2,\mathcal{D}}^2 + 2\int_{\mathcal{D}}(\tilde{\mathbf{u}}\cdot\nabla\mathbf{U})\cdot\tilde{\mathbf{u}}\mathrm{d}A}{\|\tilde{\mathbf{u}}\|_{2,\mathcal{D}}^2},$$

which should be greater or equal to unity to meet our demands for stability. Hence, with our estimate (3.5) the infimum of this latter quantity reads as

$$\inf\left(\frac{2\nu\|\nabla\tilde{\mathbf{u}}\|_{2,\mathcal{D}}^2 - \left(2\nu\sqrt{2}/\lambda_1^{1/4}\right)Gr\|\nabla\tilde{\mathbf{u}}\|_{2,\mathcal{D}}^2}{\|\tilde{\mathbf{u}}\|_{2,\mathcal{D}}^2}\right) \geq 2\nu\left(\lambda_1 - \sqrt{2}\lambda_1^{3/4}Gr\right) \geq 1,$$

such that the stability demand (3.4) is only satisfied if

$$\left(\frac{2\nu\lambda_1 - 1}{2\nu\lambda_1^{3/4}\sqrt{2}} \right) \geq Gr. \tag{3.6}$$

We check the stability condition (3.6) with computations, allowing the system to reach

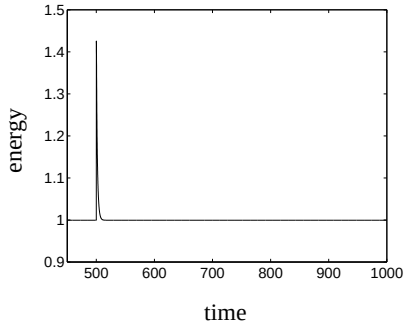

Figure 3.5: *Normalized energy time series* $E_n(t) = E(t)/\langle E(t) \rangle$ *for* $\nu = 1/5$.

a steady state first, after which a small perturbation is applied during a short interval. Using the unscaled viscosity $\nu = 1/5$, with $A_0 = 5 \times 10^{-3}$ and $k_f = 6$, such that $\|\boldsymbol{f}\|_{2,\mathcal{D}} \simeq 0.06$, the corresponding evolution of the normalized energy, E_n, is shown in Figure 3.5(a). The perturbation is applied at $t = 500$, when the system has already reached a steady state. Subsequently, the perturbation energy falls off to zero, such that the energy of the system sinks back to its stationary state value. Note that, with $\lambda_1^{-1} \leq (d^2/2\pi^2)$, the generalized Grashof number becomes $Gr \lesssim 0.3$.

3.3 Time-dependent solutions

Leaving the stationary solutions behind, in the following two Sections we analyze the phenomenology within the interval $125.0 \leq \nu' \leq 833.3$, in which the system explicitly depends on time. The upper limit to this range is set by computational rather than phenomenological considerations, rendering our explorations far from complete. Recall that the transition sequence for the time-dependent motions is

$$\text{periodic} \rightarrow \text{quasi-periodic} \rightarrow \text{mild chaos} \rightarrow \text{intermittent} \rightarrow \text{strong chaos}.$$

Three examples of the encountered phenomenology are given in normalized instantaneous contour plots of iso-vorticity lines, Figure 3.6. The phenomenology for the periodic and mild-chaotic motions is dominated by a large circulation cell, Figure 3.6(a). The intermittent states consist of low-intensity phases, during which the phenomenology is dominated by a large circulation cell, and high-intensity, during which the cell may break up into smaller cores, Figure 3.6(b). Finally, Figure 3.6(c) shows the flow in a strongly chaotic state and the configuration has changed accordingly, to include several small cores in the center of the domain. For each value of the control parameter Table 3.1 indicates the observed type of behavior and the associated computational resolution N. As in the work of Kida *et al.* [72], the value of the control parameter is decreased in discrete steps; it should be kept in mind that other types of behavior may live between each pair of adjacent values.

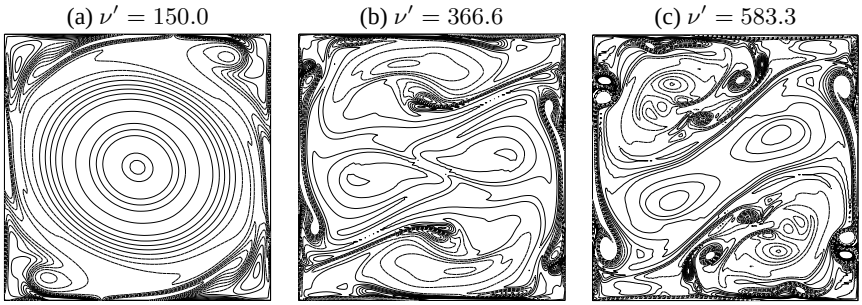

Figure 3.6: *Normalized iso-vorticity plots for $\nu' = 150.0$ (a), $\nu' = 366.6$ (b), and $\nu' = 583.3$ (c) where contours range from -10 to 10 with an interval of 1 and dashed lines represent negative values. In all plots $t \simeq 500$.*

Table 3.1: Control parameter ν', computational resolution N, a characterization of system state at large times, see Section 3.1.1 for an explanation of the symbols, and remarks on phenomenology. For all computations $T_{end} = 1000$.

ν'	N	State	Remarks
125.0	160	P	Monopole, symmetry subgroup $\mathbf{Z}_4$
133.3	”	”	symmetry subgroup $\mathbf{Z}_2$
150.0	”	”	
166.6	”	”	
183.3	”	”	
191.6	”	QP_2	Second fundamental frequency
200.0	”	”	
216.6	”	”	Jump to second QP_2 branch
225.0	”	”	
233.3	”	”	
250.0	”	”	
258.3	”	QP_3	Third fundamental frequency
266.6	”	C^I	First chaotic state
283.3	”	”	
291.6	”	I^M	Intermittent solutions
300.0	”	I^{II}	
316.6	”	I^I	
333.3	180	I^{II}	
350.0	”	I^M	
366.6	”	”	Monopole broken-up to quadrupole
383.3	”	”	
400.0	200	”	Quadrupole broken-up
416.6	”	”	
500.0	256	”	
583.3	”	C^{II}	Second chaotic state
666.6	”	”	
833.3	”	”	

3.4 Periodic flows

3.4.1 Time series and power spectra

As mentioned above, solutions in the sub-range $125.0 \leq \nu' \leq 266.6$ are time-dependent in a periodic way. Within this sub-range, the following transition sequence is found

$$S \rightarrow P \rightarrow QP_2 \rightarrow QP_3 \rightarrow C^I,$$

corresponding rather well to the Ruelle-Takens-Newhouse [120, 96] scenario. At the lower end of the range, for $\nu' = 125.0$, a transition takes place from the second steady state S to a single periodic state P, shown in Figure 3.7(a), in a time series of the normalized enstrophy, $Z_n(t)$. For several subsequent values of the control parameter, down to $\nu' \leq 183.3$, the flow remains single-periodic, although an increasing number of integer multiples of the base frequency are also excited.
Then, for $\nu' \geq 191.6$, the periodic attractor is replaced with the more complex, double- and triple-periodic motions QP_2 and QP_3. As can be clearly seen in Figure 3.7(b) for $\nu' = 200.0$ and, with more effort (c) for $\nu' = 258.3$, these states are still ordered and regular. The observed fundamental frequencies and their most important integer multiples in the quasi-periodic state are listed in Table 3.2. Finally, at $\nu' = 266.6$, periodic behavior is replaced by low dimensional chaos, Figure 3.7(d).

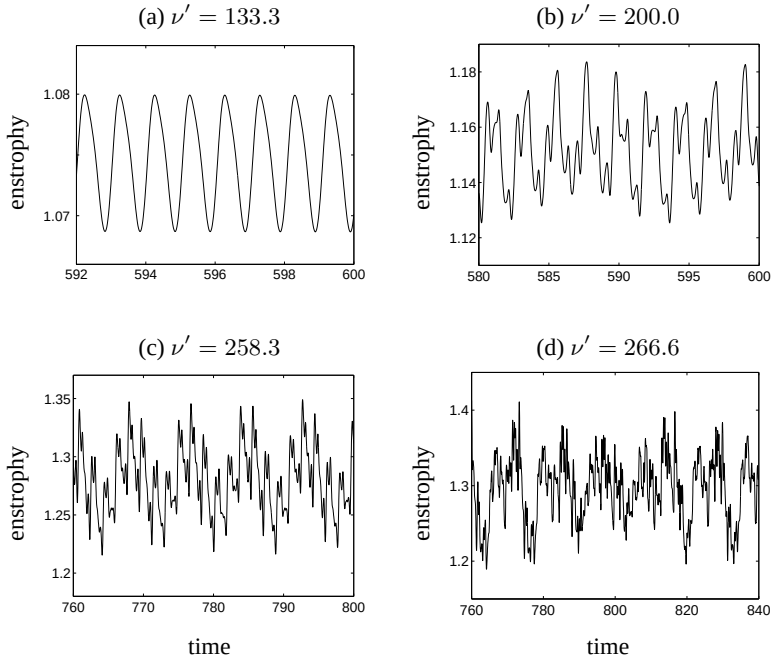

Figure 3.7: *Part of the normalized enstrophy time series, $Z_n(t) = Z(t)/\langle Z(t)\rangle$ for a periodic flow (a), a double-periodic flow (b), a triple-periodic flow (c) and a chaotic flow (d). Note the increasing amplitude of the motions*

Let us now consider in more detail the sequence described above. The first parameter value for which the solution becomes time-periodic, $\omega(t) = \omega(t + T_0)$, is found at

Table 3.2: Control parameter ν', fundamental frequencies $f_2 < f_1 < f_0$ (Hz) and their most important integer multiples, sums and differences, in increasing order in the periodic state. Low dots . . . means higher frequencies are present but not denoted.

ν'	$f_2 < f_1 < f_0$ (Hz)	Multiples, sums and differences
125.0	0.781	2
133.3	0.963	2,3
150.0	1.120	2,3
166.6	1.218	2,3
183.3	1.303	2,3,4
191.6	0.425, 1.359	$f_1 - 3f_0$, $f_1 - f_0$, $2f_1$, $f_1 + f_0$, $3f_1$, $4f_1$
200.0	0.453, 1.416	$f_1 - f_0$, $f_1 + f_0$, $f_1 + 3f_0$, $2f_1 + 2f_0$, $2f_1 + 3f_0$
216.6	0.509, 1.473	$2f_0$, $2f_1 - 2f_0$, $2f_1$, $3f_1 - 2f_1$, . . .
233.3	0.506, 1.554	$f_0 + f_1$, $2f_1$, $2f_1 + f_0$, $3f_1$, . . .
250.0	0.510, 1.643	$(f_1 - f_0)/2$, $f_1 - f_0$, $2f_1 - 3f_0$, . . .
258.3	0.552, 0.679, 1.119	$f_1 - f_0$, $2f_2 - 2f_1$,$2f_2 - f_1$, . . .

$\nu' = 125.0$, where the resulting motion has period $T_0 \simeq 1.2804$. The mechanism by which the transition occurs is a supercritical Hopf bifurcation, (see e.g., Mullin [95]) which maintains the spatial $\mathbf{Z}_4$ symmetry. Using overlapping windows of 512 points, the corresponding power spectrum was determined from 16000 data points of the normalized enstrophy time series. A single peak can be observed at the base frequency f_0 and a smaller peak at $2f_0$, Figure 3.8(a). The corresponding vorticity field (not shown) is dominated by a large circulation cell with $\mathbf{Z}_4$ symmetry.

For subsequent values of the control parameter, down to at least $\nu' = 183.3$, Figure 3.8(b), the single-periodic state persists, but here the harmonics $3f_0$ and $4f_0$ are also excited. Furthermore, small frequency shifts occur, progressively increasing the base frequency with each step. This growth of the fundamental frequency of the P state, for decreasing values of ν', is shown in Figure 3.9.
A symmetry breaking bifurcation leads to $\mathbf{Z}_2$ symmetry within the P state (the subgroup $\mathbf{Z}_2 \subset \mathbf{Z}_4$ denotes symmetry with respect to rotations over π). This corresponds to observations of a Taylor-Couette flow, where, in spite of a symmetrical forcing scheme, symmetry-breaking bifurcations occurred [95]. Remarkably, the $\mathbf{Z}_2$ symmetry is preserved for all following values of the control parameter, down to the maximum value $\nu' \leq 833.3$. For $\nu' = 150.0$ one sees the reduced symmetry in a contour plot of the corresponding normalized vorticity field, Figure 3.6(b). The central cell is slightly distorted and the secondary vortices in the corners are no longer fixed at the same position.
For $\nu' \geq 191.6$ a Neimark-Sacker bifurcation has led the flow onto a branch of quasi-periodic states, initizing a QP_2 motion. Besides several higher harmonics of the largest fundamental frequency $f_0 \simeq 1.36$, several sums and differences of integer multiples of f_0 and the smaller frequency $f_1 \simeq 0.425$ are now also excited, Figure 3.8(c). The QP_2 state lives in the range $191.6 \leq \nu' \leq 250.0$, where the value of the largest fundamental frequency increases for progressive values of the bifurcation parameter, as can be seen in Figure 3.9. With the onset of the QP_2 motion a long-time undulation appears in the system, at a subharmonic of the largest base frequency, $f_0/8$.
However, in the interval $216.6 \leq \nu' \leq 250.0$ the long-time undulation has disappeared, whereas a strong spectral peak is now present at twice the largest fundamental

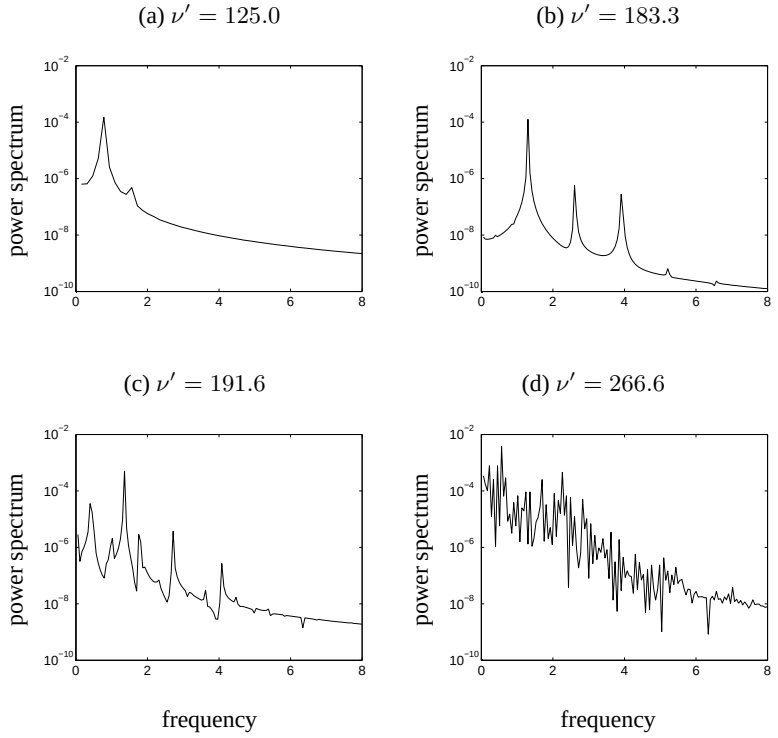

Figure 3.8: *Power spectra of vorticity time series for* $\nu' = 125.0$ *(a),* $\nu' = 183.3$ *(b),* $\nu' = 191.6$ *and* $\nu' = 266.6$ *(d).*

frequency, $2f_0$. The frequency f_1 remains nearly constant in a 'locked' state within this parameter range, see Table 3.2.
Another Hopf bifurcation occurs, leading to a QP_3 state, which is observed at $\nu' = 258.3$. Two of the new base frequencies are close to the fundamental frequencies of the previous QP_2 state, the third frequency enters at an intermediate value.

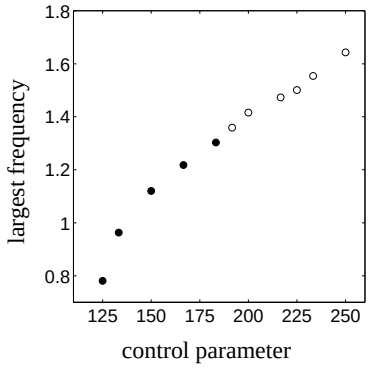

Figure 3.9: *Largest fundamental frequency* f_0 *as a function of the control parameter* ν'*. Solid circles (•) symbolize single-periodic motion, circles (○) denote quasi-periodic motion.*

For $\nu' = 266.6$ a final Hopf bifurcation has taken place, and the time series take on

a chaotic appearance, Figure 3.7(d). Even though the transient state is similar to that observed for $\nu' = 258.3$ and the system initially relaxes towards a QP_3 state of motion, this state becomes unstable and falls off into a chaotic regime. The corresponding power spectrum, Figure 3.8(d), has a strongly increased noise-level over a wide range of frequencies before it falls off, in contrast with the spectra observed earlier for the periodic motions, which have a nearly 'discrete' appearance.

Interestingly, no QP_n state with $n > 3$ was observed in our computations. According to Ruelle-Takens theory, such motions with $n = 4$ and even with $n = 3$ are unstable with respect to small perturbations and, as such, may not occur at all. On the other hand, it is very well possible that a QP_n state for $n > 3$ can be found for values of the control parameter situated between those considered here. As such, it can not be ruled out that QP_n motion may live under pre-chaotic state parameter values.

3.4.2 Phase space reconstruction

Using vorticity time series $\omega(t, \mathbf{x})$, measured at fixed locations in the flow, we reconstruct the phase space behavior of the system. For each progressive value of the control parameter the delay τ, determining $\min_1(I(\tau))$, see Section 3.1.2, is listed in Table 3.3, along with the embedding dimension D_{emb}, as determined by the false nearest neighbor technique. Due to the low embedding dimension, $D_{emb} = 3$, completely unfolded phase portraits can be made for the P state, of which we give two examples in Figure 3.10. Recall that the true dimension of the system may be non-integer, or fractal, a fact we return to later on.

At parameter value $\nu' = 125.0$ a fixed point in phase space becomes unstable and bifrucates to a limit cycle. It was clear from the spectral analysis that the branch of limit cycles persists at least to value $\nu' = 183.3$. Observe then, how the system spirals towards the limit cycle at $\nu' = 125.0$, in Figure 3.10(a), and recall the simple form of the corresponding spectrum, Figure 3.8(b). The qualitative difference with the P attractor at $\nu' = 150.0$ becomes clear from Figure 3.10(b), where the limit cycle has changed its orientation.
To explore the structure of the system in phase space and the stability properties of the attractors, we plot Poincaré sections, in Figure 3.11. Recall that the Poincaré map defines a discrete dynamical system associated to the continous dynamical system defined by the equations of motion. A limit cycle in phase space is a fixed point of the Poincaré map; the corresponding trajectory in the Poincaré section may be seen to asymptotically approach this fixed point. The limit cycle at $\nu' = 125.0$, Figure 3.11(a), shows such a discrete trajectory of the Poincaré map, asymptotically approaching a fixed point.
At $\nu' = 133.3$, Figure 3.11(b), an initial folding of the trajectory occurs, but eventually the system moves towards another nodal point, in the lower left corner of the plot.
Decreasing the control parameter to $\nu' = 166.6$ one sees again the result of folding action in Figure 3.11(c); the system seems to approach a saddle point, but as it moves away from this saddle point it finds its true attractor in the form of another nodal point, to which it asymptotically converges. This picture is somewhat resemblant of the forced oscillator discussed by Thompson and Stewart [140].
In Figure 3.11(d), for $\nu' = 183.3$, the system is close to a break-up of the limit cycle, as is apparent from the 'blurred' state of the trajectory in the Poincaré section. Even so, it still evolves to a nodal point.

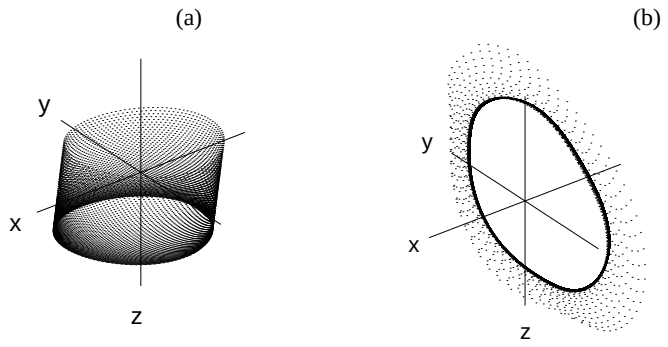

Figure 3.10: *Three-dimensional phase space trajectories, showing completely unfolded attractors;* $\nu' = 125.0$ *(a) and* $\nu' = 150.0$ *(b).*

Apart from the latter situation, the encountered limit cycles are hyperbolic, that is, possessing a linearized Poincaré map with two real eigenvalues within S^1, the unit circle in the complex plane. This suggests a structural stability of the system; small perturbations will result in a limit cycle with the same stability properties, an observation we discuss in Section 3.6, see Thompson and Stewart [140] for details.

A dramatic change is brought about by the Neimark-Sacker bifurcation, when the control parameter is changed to $\nu' = 191.6$, Figure 3.11(e), resulting in a QP_2 attractor. First of all, this Poincaré section is not completely unfolded, but rather a projection onto the plane, as the embedding dimension of the system has increased to $D_{emb} = 4$ and the true Poincaré section should thus be three-dimensional. The QP_2 attractor fills a 2-torus and the Poincaré section accordingly reveals a closed loop or limit cycle, with the outlying points caused by transients.
When the bifurcation parameter equals $\nu' = 200.0$ the Poincaré section, Figure 3.11(f), shows again a closed loop, as was the case for $\nu' = 191.6$, but here the projection onto the plane results in a somewhat twisted trajectory. For $\nu' = 216.6$ (not shown) the system explores an even larger region of phase space, whereas more sums of multiples of f_0 and f_1 have been added to the flow.
For the interval $233.3 \leq \nu' \leq 266.6$, we project several attractors onto the $(\omega(t), \omega(t+\tau))$-plane along with the Poincaré sections, in Figure 3.12. None of these plots shows a completely unfolded attractor, as $D_{emb} = 4$ in all cases, but nevertheless some essential topological features become clear.
Recall from the previous Section that two different types of QP_2 motion were ob-

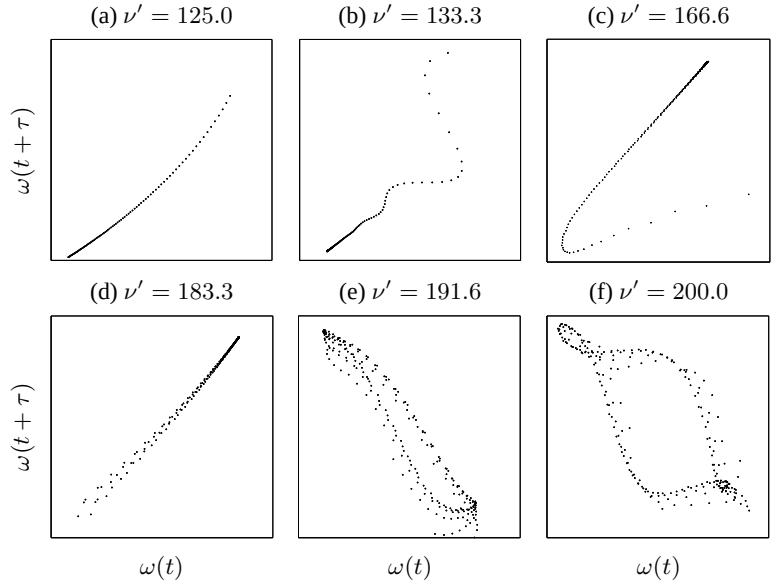

Figure 3.11: *Poincaré trajectories, attracted to fixed points (a), (b), (c) and (d), and to limit cycles (e) and (f).*

served, below and above the value $\nu' = 216.6$. This change within the QP_2 state is interpreted as a jump from one branch of quasi periodic solutions to another, resulting in a different Poincaré map. At $\nu' = 233.3$ the phase portrait, shown in Figure 3.12(a), looks somewhat like the phase portrait of the QP_2 attractor observed by Cumming and Linsay [31] in a nonlinear electronic resonator. Here the system has jumped to a different branch of QP_2 solutions and the corresponding Poincaré section, Figure 3.12(e), reveals a structure that looks more or less like three nodal points, along with quite some outlying crossings of the plane, instead of the closed loop observed before. The QP_2 attractor found at parameter value $\nu' = 250.0$, Figure 3.12(c), has an even more complicated structure than that at value $\nu' = 233.3$, but still this is a system with two rather than three incommensurate frequencies. The corresponding Poincaré section, Figure 3.12(d), clearly shows how the system is asymptotically attracted to three nodal points, at which phase space trajectories cross the Poincaré plane.

While the projection of the QP_3 attractor onto the plane, Figure 3.12(e), seems to be similar to a similar projection of the QP_2 attractor, the Poincaré section, Figure 3.12(f), clearly reveals the differences between these states. Indeed, the QP_3 phase portrait should be rotated in three-space to appreciate its structure. Remarkably, one can observe three well-defined initial 'tails', which may be inherited from the previous QP_2 state.
Then, at $\nu' = 266.6$ the system spirals into chaos, but not all of the structure of the preceding periodic attractor is lost in the phase portrait, Figure 3.12(g), whereas the embedding dimension remains unaltered, $D_{emb} = 4$. Hence we denote this low-dimensional chaos with C^I. A similar state was described by Thompson and Stewart [140] to be low-dimensional behavior that has certain order, as well as a random component. But the random component follows from the system dynamics only, no

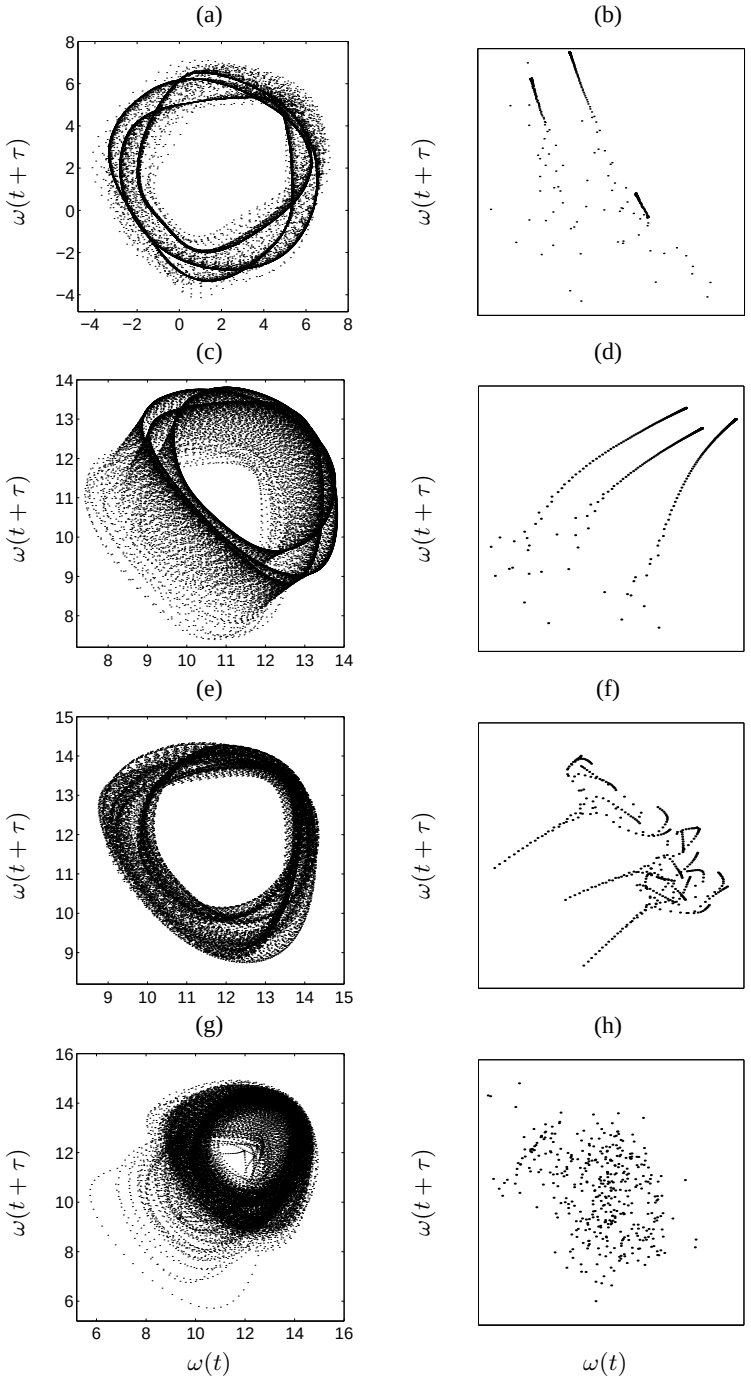

Figure 3.12: *Projection of the attractor onto the* $(\omega(t), \omega(t+\tau))$*-plane (left column) for* $\nu' = 233.3$ *(a),* $\nu' = 250.0$ *(c),* $\nu' = 258.3$ *(e) and* $\nu' = 266.6$ *(g). The corresponding Poincaré sections, hyper-planes in* $(\omega(t), \omega(t+\tau), \omega(t+2\tau))$*-space (right column), graphs (b), (d), (f) and (g).*

stochastic impurities were introduced into the system by means of forcing or initial condition. A close-up of the main part of the Poincaré section, Figure 3.12(h) shows that structure is lost and the Poincaré map is not properly linearizable. This state is very similar to what Libchaber *et al.* [80] observed in a Bénard convection experiment; incomplete decay of 3-torus onto a strange attractor.

For the (quasi-) periodic motions, phase space trajectories should, on average, remain at a fixed distance. In a logarithmic graph of the stretching factors ϕ, see Section 3.1.2, which slope determines the maximum Lyapunov exponent ϕ_{max}, see Section 3.1.2, one should therefore observe a relaxation to a constant value, see also Rosenstein *et al.* [115]. Indeed one sees such a behavior for, e.g., the QP_2 motion found at $\nu' = 200.0$, in Figure 3.13(a), yielding a zero estimate for ϕ_{max}. Here the logarithm of the stretching factors was determined over 20000 data points, for several values of the delay, to test the sensitivity of the results with respect to this parameter. Specifically, the Figure shows the curves for $\tau = 4\Delta t$ and $\tau = 5\Delta t$, where Δt is the sampling interval.
The Theiler window, Δl, is a temporal lag that excludes temporally correlated points from the estimation procedure for the correlation dimension, D_{corr}, see Section 3.1.2. The value of Δl follows from a space-time separation plot, of which an example is shown in Figure 3.13(b), for $\nu' = 200.0$. In the Figure one clearly sees the recurrent, periodic behavior, reflected in temporal correlations, whereas a minimal estimate for the Theiler window roughly equals $\Delta l = 30\Delta t$.

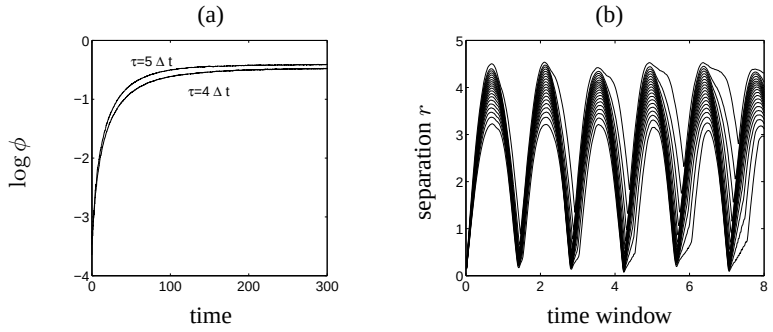

Figure 3.13: *Logarithm of the stretching factors ϕ for two delays (a) and the corresponding space-time separation plot (b), at parameter value $\nu' = 200.0$. The space-time separation plot shows, as a function of the minimal temporal separation window of points in a time series, the fraction of points that is closer than some separation distance in m-dimensional phase space. Fractions increase from 0.1 (bottom curve) to 1 (top curve) in steps of 0.05.*

As expected, purely periodic motions result in low-dimensional phase space behavior, where D_{corr} is slightly larger than unity, see Table 3.3. While one subsequently expects the value $D_{corr} = 2$ for motion on a 2-torus, somewhat larger estimates are found, for the interval $191.6 \leq \nu' \leq 216.6$. Remarkably, the value of the correlation dimension then falls off to about $D_{corr} \simeq 1.5$ for $225.0 \leq \nu' \leq 250.0$, even though the motion is still quasi-periodic at these parameter values. The phenomenon is caused by the jump to a different branch of QP_2 solutions, also observed in the Poincaré sections, compare, e.g., Figure 3.11(f) and Figure 3.12(d).
A QP_3 motion should, ideally, result in a correlation dimension $D_{corr} = 3$, see also

the example given by Rosenstein *et al.* [116]. Indeed, with $D_{corr} \simeq 2.9$, the estimate is close to the expected value. Finally, the chaotic motion at $\nu' = 266.6$ is of a slightly higher dimension than the preceding periodic flows.

Table 3.3: For each value of the control parameter ν', estimates are given for the discrete delay $(\tau/\delta t)$ and the correlation dimension D_{corr}.

ν'	state	$(\tau/\Delta t)$	D_{emb}	D_{corr}
125.0	P	37	3	1.4 ± 0.1
133.3	”	43	”	1.3 ± 0.2
150.0	”	18	”	1.1 ± 0.1
166.6	”	35	”	1.1 ± 0.2
183.3	”	33	”	1.2 ± 0.1
191.6	QP_2	24	4	2.7 ± 0.2
200.0	”	22	”	2.6 ± 0.1
216.6	”	19	”	2.5 ± 0.3
225.0	”	21	”	1.5 ± 0.2
233.3	”	12	”	1.5 ± 0.1
250.0	”	22	”	1.6 ± 0.1
258.3	QP_3	18	”	2.9 ± 0.1
266.6	C	17	”	3.6 ± 0.2

Summarizing, the Ruelle-Takens-Newhouse scenario seems to be fulfilled in the parameter range up to $\nu' < 266.6$, where chaos results from the destruction of a 3-torus. Remarkably, Braun *et al.* [18] observed chaos after the destruction of a 2-torus in a 2D flow of large aspect ratio, with one periodic and one no-slip direction. On the other hand, Feudel and Seehafer [47] did observe a 3-torus in the route to chaos on a double-periodic square domain.
The chaotic motions discussed so far are low-dimensional and still far removed from turbulence. In the next Section we examine, for decreasing values of the control parameter, the mechanisms that are thought to bring the flow to high-dimensional chaos.

3.5 Intermittent flows

3.5.1 Time series

The C^I chaotic state, observed at parameter value $\nu' = 266.6$, is also found for $\nu' = 283.3$. Increasing, however, the value of the control parameter to $\nu' = 291.6$, a dramatic change has taken place; the C^I state is disturbed by irregular violent bursts of large amplitude, collectively referred to as a I^I regime, reminiscent of the intermittent motions observed by Manneville and Pomeau [90]. In Figure 3.14 we show a close-up of a true C^I state and a laminar I^I state in parts of two vorticity time series, along with the corresponding power spectra. In Figure 3.14(a) one sees the C^I behavior of the flow at $\nu' = 283.3$, where the spectrum, Figure 3.14(b), is taken over 4096 data points and averaged over overlapping windows of 1024 points, around $t = 375$. Similarly, for $\nu' = 316.6$, Figures 3.14(c) and (d) display a part of a vorticity time series and the power spectrum, during a laminar phase of the evolution. The power spectrum is again taken over 4096 points in the laminar interval. Qualitatively, the laminar part of the I^I state is similar to the C^I state, but in the I^I state the laminar intervals are disturbed by

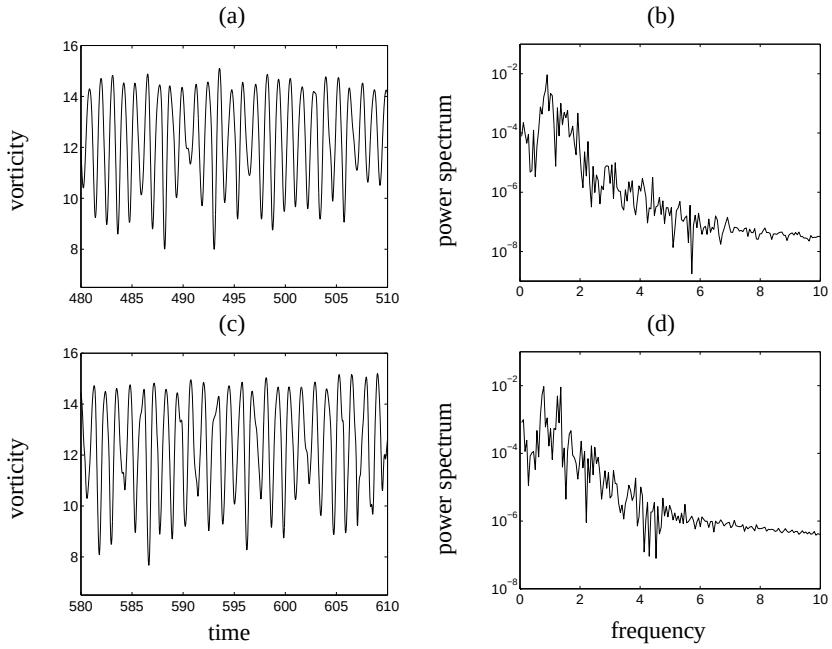

Figure 3.14: *Vorticity time series for $\nu' = 283.3$ (a) and $\nu' = 316.6$ (c), with the corresponding power spectra shown in (b) and (d) respectively.*

violent bursts, with intensities of up to ten times the mean value. In Figure 3.15(a) the overall behavior of a normalized vorticity time series in the I^I state at $\nu' = 316.6$ is shown. Note the length of the laminar phase as compared to the bursts and the intensity of these bursts.
Then, for parameter value $\nu' = 300.0$, the system has jumped to a different type of intermittent behavior, denoted as I^{II}. This second type of intermittent motion, is shown in a normalized vorticity time series in Figure 3.15(b), for $\nu' = 333.3$. Here, laminar intervals take on a more or less regular appearance, but last much shorter than in the I^I state, while high-intensity bursts appear more frequently but are generally less violent, as compared to the laminar behavior. With decreasing parameter values, the laminar part of the I^{II} state lasts shorter with a less regular distribution, whereas bursts appear more frequent.
Pure I^{II} flows were observed for parameter values $\nu' = 300.0$, $\nu' = 333.3$ and $\nu' = 383.3$, a pure I^I flow only for $\nu = 316.6$, while a combination of the two was found at intermediate parameter values. This mixed state is denoted with the symbol I^M. During the mixed state a I^{II} state may suddenly give way to a laminar I^I motion, followed by a violent burst, after which the system may either go through another I^I cycle or return to the I^{II} state.

While the two intermittent regimes are generally different, some comparable phenomenological aspects are observed in both states. Minima in the energy and enstrophy time series coincide in both regimes. The peaks in these time series do, however, not coincide; enstrophy peaks usually occur when the energy shows a sharp decline. This feature can be explained as follows; during the laminar phase the energy of the system

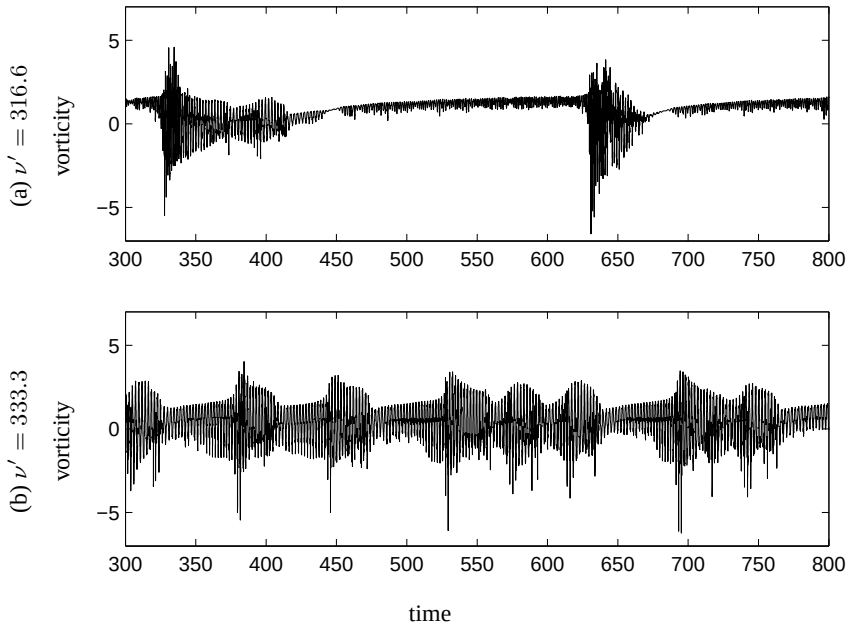

Figure 3.15: *Vorticity time series, normalized by the root-mean-square, displaying the qualitative difference between the two types of intermittency for I^I (a) and I^{II} (b).*

can gradually build-up to peak values. In this case the flow field is dominated by a stable central circulation cell, possibly with several accompanying satellite vortices of opposite sign. Such a stable configuration, and the central cell in particular, may carry increasing amounts of energy. However, depending on the value of control parameter ν', this configuration is either severely altered or even destroyed during a high intensity event, resulting in a sharp fall-off of the energy, whereas the small-scale structures produced in the event generate a peak in the enstrophy time series.

Consequently, the flow field $\omega(t, \mathbf{x})$ takes on an ever more complicated structure during the bursts. At the lower end of the subrange, for $\nu' = 300.0$, $\nu' = 316.6$ and $\nu' = 333.3$ (not shown), a large core of the central circulation cell still remains intact at all times. But in this state secondary vortices have detached from the corners of the domain and are moving closer to the interior of the domain. Then, for $\nu \geq 366.6$, Figure 3.6(b), the central structure is finally broken into two cores.

The differences between the laminar phases in the I^{II} and I^I states are visualized in two contour plots in Figure 3.16(a) and (b), for, respectively $\nu' = 300.0$ and $\nu' = 316.6$. In the I^{II} laminar phase, $\nu' = 300.0$, a shedding of small, secondary vortices has taken place, which move as satellites with the central cell. On the contrary, secondary vortices are visible in the I^I laminar phase, but these remain at more or less fixed locations during the evolution, whereas the central cell is somewhat larger than in the I^{II} laminar phase.

Another instrument to characterize a time series is the second-order structure function

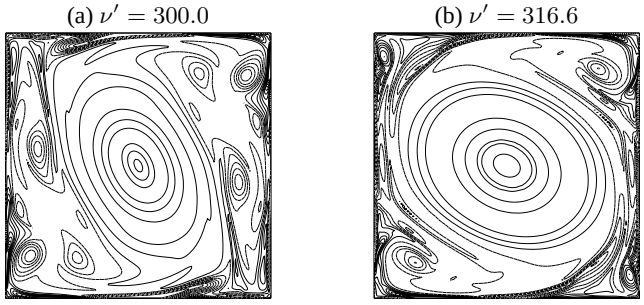

Figure 3.16: *Iso-vorticity contour plots of the laminar phase for $\nu' = 300.0$ (a) and $\nu' = 316.6$ (b). Contour lines in (a) range from -30 to 30 with an interval of 3 and from -50 to 50 with an interval of 5 in (b); negative values are represented by dashed lines.*

$S_2(n)$, which, as a function of the time-lag n, reads as

$$S_2(n) = \frac{1}{T} \int_0^T \left(\omega(t + n\Delta t) - \omega(t)\right)^2 \mathrm{d}t.$$

In various systems $S_2(n)$ may scale with n as follows,

$$S_2(n) \propto n^{2D},$$

where D is the scaling exponent. As discussed by Provenzale *et al.* [111] for the motion

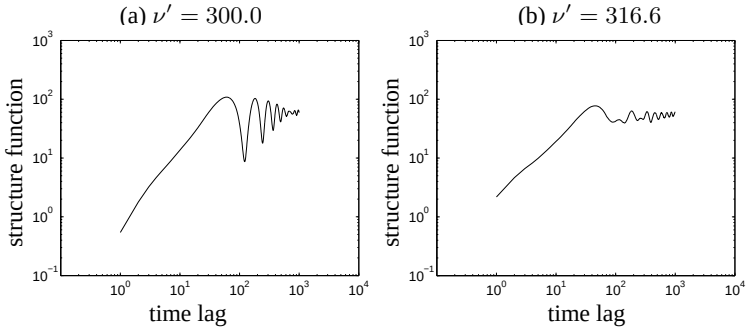

Figure 3.17: *Scaling behavior of second-order structure function $S_2(n)$ with time lag n, for the I^{II} state (a) and the I^I state (b).*

on a strange attractor, with increasing values of n one observes the following behavior of $S_2(n)$; first $D = 1$ for small n. Then, for slightly larger n, the structure function oscillates and finally converges to a constant value, corresponding to the limited region of phase space explored by the system. For the intermittent motions I^I and I^{II}, Figure 3.17 displays the scaling of the second-order structure function. At $\nu' = 300.0$ (I^{II} state), Figure 3.17(a), $S_2(n)$ has a scaling behavior that is roughly similar to the description by Provenzale *et al.*; a short interval has scaling exponent that is slightly larger than unity, after which progressively smaller oscillations convergence to a constant value. For $\nu' = 316.6$, Figure 3.17(b), the oscillating phase is virtually absent,

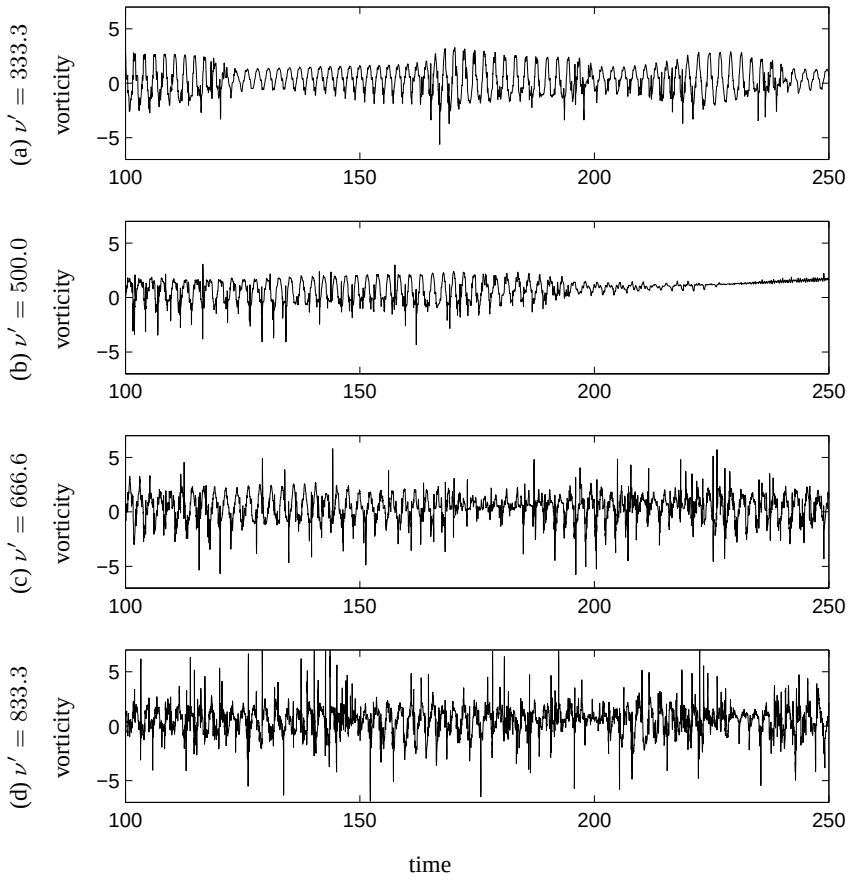

Figure 3.18: *Vorticity time series, normalized by its root-mean-square, for* $\nu' = 333.3$ *(a),* $\nu' = 500.0$ *(b),* $\nu' = 666.6$ *(c) and* $\nu' = 833.3$ *(d).*

whereas the initial scaling is closer to the expected $D = 1$. The structure-functions for the mixed motions I^M (not shown), display a scaling that is a combination of those shown in Figure 3.17; a $D = 1$ initial scaling, followed by oscillations.

The intermittent motions are observed in the range $291.6 \leq \nu' \leq 500.0$, but at parameter value $\nu' = 583.3$ the system has become predominantly chaotic. In this state of motion, designated as C^{II} and associated to a high-dimensional phase space behavior, laminar phases are short and rare events. In Figure 3.18 the normalized vorticity evolution is shown in the same time interval, for several parameter values. While laminar, low-intensity motions are recognizable for $\nu' = 333.3$ and $\nu' = 500.0$, Figures 3.18(a) and (b), these types of motions have disappeared for $\nu' = 666.6$ and $\nu' = 833.3$, Figures 3.18(c) and (d). Furthermore, the overall intensity of the vorticity increases significantly from $\nu' = 333.3$ to $\nu' = 833.3$, moving from intermittent motions to a new phase of chaos.

3.5.2 Phase space reconstruction

An important question is whether the I^I, I^{II} and mixed I^M types of motion result in different types of phase space behavior and, if so, how these differences can be quantified. As in the previous Section, we determine the quantities τ and D_{emb}. These quantities are listed in Table 3.4, along with the system state, and used to construct phase portraits and Poincaré sections to answer our questions. While it is hard to draw firm conclusions, the I^{II} state generally requires higher embedding dimensions than the I^I state. The more complicated phase space behavior encountered in the present parameter range is resembled by a higher embedding dimension; the number D_{emb} is seen to grow fast with decreasing values of the viscosity parameter once $\nu' \geq 283.3$. As such, it is not possible to produce completely unfolded phase portraits and once more we have to be satisfied in general with a projection onto the $(\omega(t), \omega(t+\tau))$-plane.

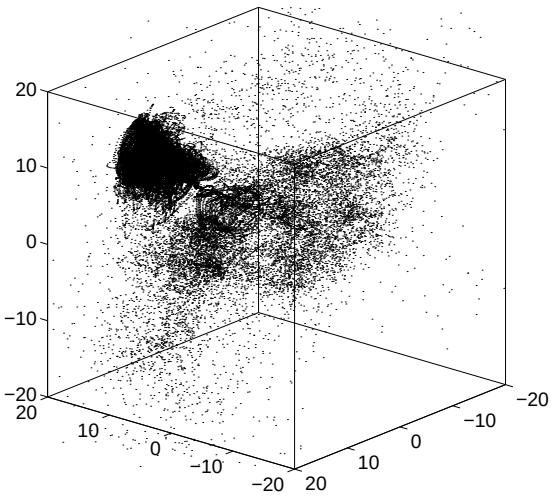

Figure 3.19: *Three-dimensional embedding, for $\nu' = 316.6$, in $(\omega(t), \omega(t+\tau), \omega(t+2\tau))$-space.*

Let us however, first look at a three-dimensional $(\omega(t), \omega(t+\tau), \omega(t+2\tau))$ embedding of the pure I^I-attractor occurring at $\nu' = 316.6$, in Figure 3.19. Note that the axes are drawn at arbitrary levels, zooming in on the central area of the attractor. Here we recognize, with some effort, in the dense area in the upper left-hand corner a structure very similar to the C^I-attractor observed in Figure 3.12(g) in the previous Section. This structure is caused by the long intervals with laminar C^I motion in the I^I state. Remarkably, the connection between the laminar area and the surrounding cloud caused by the violent bursts appears in the form of a very well-defined trajectory. This seems to be a characteristic feature of the I^I motion, as it does not occur for the pure I^{II} state.

Even though the intermittent motions observed here are generally of higher dimension than the systems discussed by Manneville and Pomeau, certain characteristics seem to be similar. During the laminar motions of the C^I cycle the system is close to an old attractor, such that the system displays some kind of memory of its previous states. This behavior was recognized by Manneville and Pomeau in their Lorenz model, where intermittent solutions possessed some memory of an old limit cycle. However, neither of the two distinct types of intermittency observed in our computations can directly be related to the three types of intermittency proposed in the Manneville-Pomeau theory.

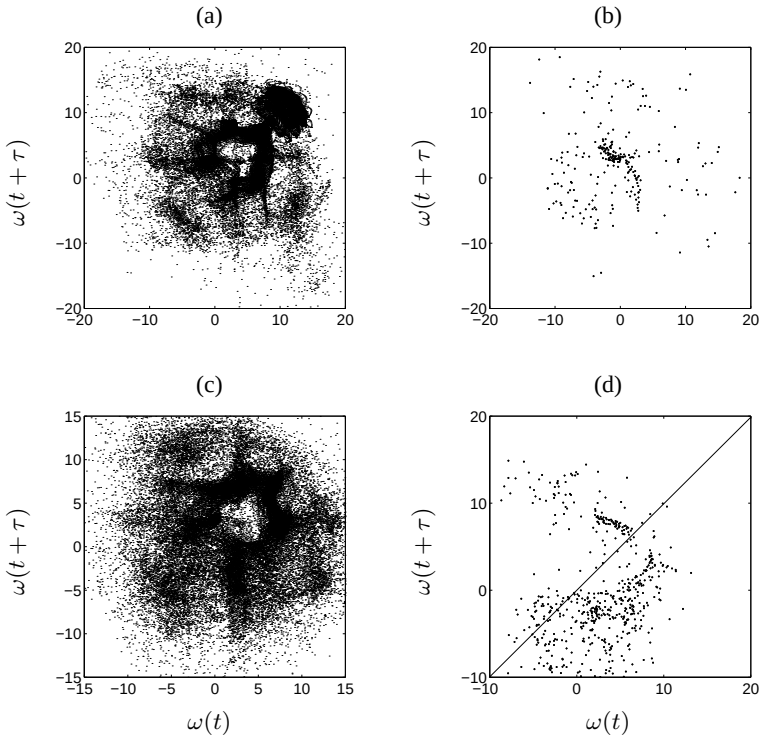

Figure 3.20: *Close-up of a projection of the attractor onto the* $(\omega(t), \omega(t+\tau))$*-plane, for* $\nu' = 291.6$ *(a) and* $\nu' = 333.3$ *(c). The corresponding Poincaré sections, (b) and (d), are slices through* $(\omega(t), \omega(t+\tau), \omega(t+2\tau))$*-space.*

Figures 3.20(a) and (c) display close-ups of the central part of the attractor for, respectively, $\nu' = 291.6$ and $\nu' = 333.3$. Not surprisingly, the pure I^{II}-attractor, observed for $\nu' = 333.3$, has a very different form as compared to the pure I^{I}-attractor in Figure 3.19. On the other hand, the mixed I^{M} phase portrait in Figure 3.20(a) has some features in common with the I^{II} phase portrait, specifically the spider-web structure in the central area of the projection, which is caused by the laminar part of the I^{II} motions. The dense 'blob' of points in the upper right-hand corner is caused by the I^{I} laminar motions, which are confined to a rather narrow region of phase space.
The corresponding Poincaré sections result from the crossing of trajectories in a three-dimensional phase space embedding with a plane and are shown in Figures 3.20(b) and (d). With some imagination a 'butterfly structure' can be seen in Figure 3.20(b), with the dense crossing caused by laminar motions forming the body and the outlying crossings caused by the bursts forming the wings of the butterfly. Even though the system at $\nu' = 316.6$ is in a pure I^{I} state, the Poincaré section in that case has a similar butterfly-like structure, but for the other I^{M} states this structure is lost.
In Figure 3.20(d) a diffuse parabolic curve can be distinguished. However, it cannot be established beyond doubt whether this is truly a characteristic of the dynamics or if the structure arises due to the incomplete unfolding of the Poincaré section. In low-dimensional problems the part of a parabola falling below the bi-sectrix, shown in the

Figure as a solid line, corresponds to brief intervals of laminar motion. Overall, the picture could correspond to the intermittency of the first type, as observed by Manneville and Pomeau [90], where a real eigenvalue of the linearized Poincaré map crosses the unit circle, but again, the high dimensionality of the problem prohibits firm conclusions.

For the higher dimensional attractor found at parameter value $\nu' = 350.0$, Figure 3.21(a), the spider-web structure has evolved beyond recognition. Here the thick column protruding from the central region contains the laminar C^I-like motions. A close-up for $\nu' = 400.0$, Figure 3.21(b), shows this column and the very high density of phase space points it contains more clearly.
From the Poincaré section at $\nu' = 350.0$ and $\nu' = 400.0$ (not shown) it is even less straightforward to draw conclusions; again any occurring patterns of crossings could be caused by incomplete unfolding rather than the dynamics.

Table 3.4: Control parameter ν', the system state, discrete delay $(\tau/\delta t)$ determining $\min_1(I(\tau))$, embedding dimension D_{emb} and the correlation dimension D_{corr}.

ν'	state	$(\tau/\Delta t)$	D_{emb}	D_{corr}
283.3	C^I	16	4	-
291.6	I^M	33	6	2.7 ± 0.2
300.0	I^{II}	32	8	2.8 ± 0.2
316.6	I^I	26	5	4 ± 0.5
333.3	I^{II}	32	6	-
350.0	I^M	48	10	3 ± 0.2
366.6	I^M	-	-	-
383.3	I^{II}	43	10	5 ± 0.5
400.0	I^M	54	11	-
416.6	I^M	51	5	3.5 ± 0.3
500.0	I^M	51	6	-
583.3	C^{II}	29	-	-
666.6	”	35	-	-
833.3	”	32	-	-

As mentioned in Section 3.1.2, it may be impossible to obtain reliable estimates for the correlation dimension D_{corr} and the maximum Lyapunov exponent ϕ_{max} if the dimension of the system grows beyond certain limits for progressive values of the control parameter. Indeed, we run up to this problem for the flows discussed in the present Section. While the estimate $D_{corr} = 3.6$ was obtained for the C^I motion at $\nu' = 266.6$, no clear estimate is obtained for the same type of motion at $\nu' = 283.3$. Given that the embedding dimension remains unaltered, it can be assumed, however, that the value of D_{corr} will be close to the estimate at $\nu' = 266.6$. On the other hand, under $\nu' = 266.6$ no value for ϕ_{max} was obtained, whereas the system at $\nu' = 283.3$ yields $\phi_{max} \simeq 0.08$. This latter value is comparable with the estimate for the famous Rössler attractor, but much lower than that for the Lorenz attractor, which is close to 1.5, see Wolf *et al.* [152]. The first intermittent motions, encountered at $\nu' = 291.6$ and $\nu' = 300.0$, yield much lower correlation dimension estimates than their respective embedding dimensions would suggest. However, no *a priori* expected values exist for these states. Unfortunately it is thus not possible to relate our estimates to known val-

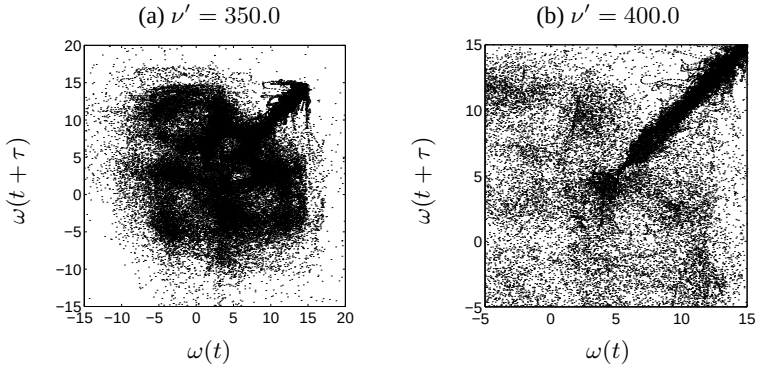

Figure 3.21: *Close-up of a projection of the attractor onto the* $(\omega(t), \omega(t+\tau))$*-plane, for* $\nu' = 350.0$ *(a) and* $\nu' = 400.0$ *(b).*

ues for different systems. Problems arise due to the dual character of the time series; while the laminar motions may be low-dimensional the chaotic bursts may not, thus 'fooling' the method applied to estimate D_{corr}. In terms of the quantity D_{corr} there is no marked difference between the I^I and I^{II} states, as far as the estimates are reliable.

Summarizing, while the Ruelle-Takens-Newhouse scenario guides the system from stationarity to low-dimensional chaotic solutions, it is a type of intermittency scenario that moves the flow from low- to high-dimensional chaos. A complicated sequence of transitions leads the system from one type of intermittency to the next, where each phase is associated to a different pattern in phase space.

3.6 Stability analysis

Computational resolution

To determine the influence of variations in the computational resolution N on the observed phenomenology, a series of simulations was executed with constant time step $\delta t = 0.000135$ and increasing spatial resolution. As before, the forcing parameters are fixed at $A_0 = 0.05$ and $k_f = 6$, whereas the bifurcation parameter equals $\nu' = 250.0$, which is in the regime of double-periodic solutions. Increasing the value of the computational resolution in each direction from $N = 129$ to $N = 257$, Table 3.5 lists the measured value of the fundamental frequencies. While no variation is recorded in f_0, the value of the second frequency, f_1, is overestimated for the lowest resolution $N = 129$. Within the resolution of the power spectrum the higher resolution computations seem well-resolved.

Forcing wavenumber

Although the route to chaos was treated as a one-parameter problem in the previous Sections, it is essentially a two-parameter problem, where different transition sequences may be found if the position in (k_f, ν)-space is altered. In this respect, it was already observed by Tabeling *et al.* [134], that a different number of driven vortices in

Table 3.5: Fundamental frequency f_0 for each computational resolution N.

N	129	161	181	201	217	257
f_0	1.643	1.643	1.643	1.643	1.643	1.643
f_1	0.540	0.510	0.509	0.510	0.510	0.510

a quasi 2D flow of large aspect ratio may lead to a different route to chaos. Hence, we briefly consider the transition sequence that can be observed if the forcing wavenumber is changed to $k_f = 4$, keeping the amplitude fixed at $A_0 = 0.05$. The forcing mechanism now consists of 16 driven vortices of alternating sign, arranged in a linear array. Again, the phenomenology is dominated by a large circulation cell and the transition sequence to low-dimensional chaos consists of periodic and quasi-periodic motions. However, the fundamental frequencies associated to these motion are different from the situation for $k_f = 6$ and the transitions are found at different values of the kinematic viscosity. E.g., if one defines once more the control parameter $\nu' = (1/k_f\nu)$, at $\nu' = 200.0$ one now finds QP_2 motion with $f_0 = 2.209$ and $f_1 = 1.133$, as opposed to the values $f_0 = 1.416$ and $f_1 = 0.453$, found for $\nu' = 200.0$ under $k_f = 6$.

Initial condition

To test the stability of the observed time-dependent solutions with respect to small initial perturbations, the initial condition $\omega_0(\mathbf{x}) = 0$ was replaced by a Gaussian white-noise vorticity field of amplitude $\tilde{a}$. These tests were executed for control parameter $\nu' = 250.0$, with forcing parameters $A_0 = 0.05$ and $k_f = 6$, computational resolution $N = 181$ and time step $\delta t = 2.7 \times 10^{-4}$.

The main consequence of the random initial conditions is a breaking of the $\mathbf{Z}_2$ symmetry in the vorticity field. Once such a symmetry-breaking has occurred the system may, however, return to a nearly symmetric flow field at a given moment during the evolution, depending on the strength of the initial perturbation. Figure 3.22(a) and (b) show contour plots of the vorticity field prior to and just after a symmetry breaking becomes visible in the entire domain.

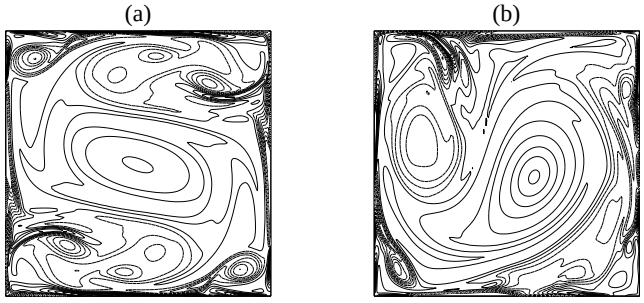

Figure 3.22: *Iso-vorticity contour plots revealing for $\nu' = 250.0$ and $\tilde{a} = 0.01$, before (a) and after (b) a $\mathbf{Z}_2$ symmetry breaking becomes visible in the entire flow field. Contour lines range between -30 and 30 with an interval of 3 and negative values are represented by dashed lines.*

So let us discuss the encountered phenomenology for increasing values of the second control parameter $\tilde{a}$. The end state for parameter value $\tilde{a} = 0.0$, already discussed in Section 3.4, is a QP_2 motion, a quasi-periodic motion with two incommensurate frequencies, one at $f_1 = 1.076$ and one at $f_0 = 0.509$. However, for parameter value $\tilde{a} = 0.0001$, the $\mathbf{Z}_2$ symmetry is broken during the transient state, which lasts up to $t \simeq 300$, after which the system returns to a nearly symmetric state and enters a stable QP_2 motion. The largest base frequency equals again $f_1 = 1.076$, but contrary to the case for $\tilde{a} = 0.0$ a long-time undulation is now present at $f_0/9$. Hence, while the system seems to behave rather different under influence of the initial perturbation, several of its spectral characteristics are surprisingly well-preserved.

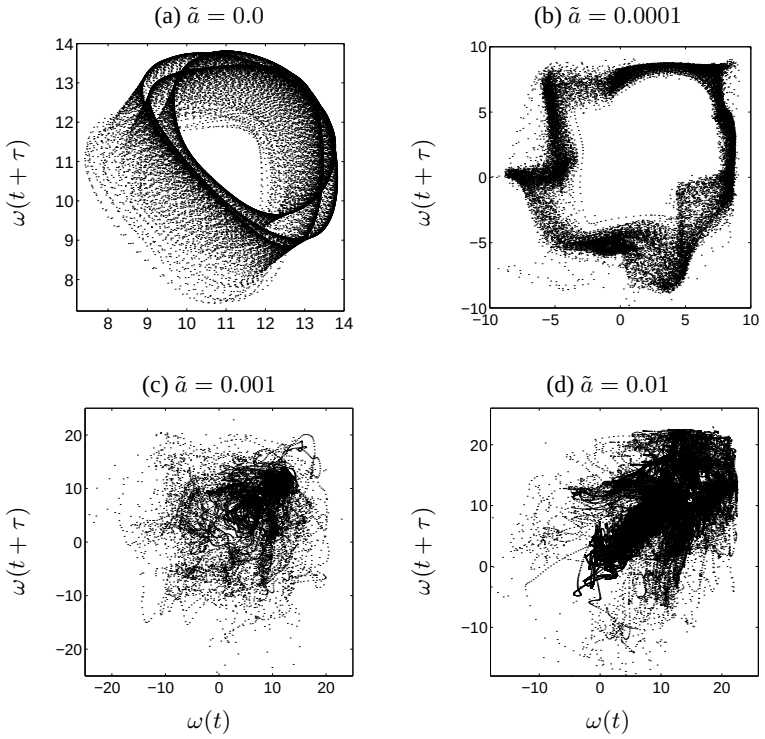

Figure 3.23: *Phase portraits for* $\nu' = 250.0$ *and* $\tilde{a} = 0.0$ *(a),* $\tilde{a} = 0.0001$ *(b),* $\tilde{a} = 0.001$ *(c) and* $\tilde{a} = 0.01$ *(d), projected on the* $(\omega(t), \omega(t+\tau))$*-plane.*

On the other hand, it is interesting to compare the phase portrait for $\tilde{a} = 0.0001$, Figure 3.23(b), with the phase portrait for $\tilde{a} = 0.0$, Figure 3.23(a). While the delay is roughly equal to the delay in the unperturbed system, $\tau = 25\delta t$, the phase portrait is dramatically different.

If the second control parameter is increased tenfold to $\tilde{a} = 0.001$, the flow moves from one large-scale instability to the next with laminar phases in between, similar to the unperturbed system in the intermittent state I^I. Accordingly, the phase portrait reveals a complicated motion through phase space, where trajectories spiral around a core of laminar motions, Figure 3.23(c). The effect of an increase in one control parameter is thus quite profound; the system has moved towards a state of motion similar to that

encountered for $\tilde{a} = 0.0$ and $\nu' = 316.6$. In the vorticity field the instabilities cause symmetry breaking, but during the laminar phases the flow is nearly symmetric; the initial noise is not strong enough to force a definite change.

The evolution for $\tilde{a} = 0.01$, is again spectacularly different from the evolution starting with zero initial conditions, breaking of $\mathbf{Z}_2$ symmetry takes place at an early stage, around $t \simeq 100$, when the random irregularities contained in the initial condition have been sufficiently amplified by the dynamics. A close-up of the phase portrait is shown in Figure 3.23(d), revealing a core in the phase space projection where the motion follows a complex pattern.

Further discussion

As a one-parameter problem the route to high-dimensional chaos was found to consist of two parts. A Ruelle-Takens scenario takes the flow from stationary to low-dimensional chaotic motions, after which intermittent behavior dominates the transition to high-dimensional chaos. A problem with the applied DNS techniques is that the continuous parameter space can only be explored in discrete steps. Different behavior may live under intermediate values of the control parameter and the precise position of the critical parameter values, at which bifurcations take place, is not possible. On the other hand, unlike a (severely) truncated computational model, a DNS yields Navier-Stokes solutions.
If the purely 2D computations are to be compared with quasi 2D laboratory experiments, it should be kept in mind that the sensitive dependence on the initial conditions (as shown in the present Section for small random disturbances in the initial flow field) may influence the actual transition sequence. Small, random initial fluctuations are thought to be unavoidable in laboratory experiments, which may result in a significantly different phase space behavior.

Chapter 4

Evolution of integral quantities

Civilization begins with order, grows with liberty, and dies with chaos.
Will Durant (1885 - 1981)

4.1 Introduction

If a fluid is brought to motion by the stochastic forcing $q(t, \mathbf{x})$, described in Section 2.2, a wholly different flow is created as compared to the flows resulting from the steady stirring forces applied in the previous Chapter. As remarked by Robinson [114], the solution of the vorticity equation $\omega(t, \mathbf{x})$ at time $t > t_0$ now depends on all times following the initial time t_0 and the global attractor $\mathcal{A}$ is no longer a well-defined object. In this setting we analyze the phenomenology in terms of the most important integral quantities, discussed earlier in Section 1.3. Although the resulting flow is of low to intermediate Reynolds number, it nonetheless displays a turbulent character.
A major problem in the case of a bounded domain equipped with no-slip walls, is the lack of *a priori* control over the asymptotically averaged enstrophy dissipation, χ, due to the production of vorticity at the no-slip walls. Simultaneously, this vorticity production alters the flow phenomenology completely, as compared to turbulence on a double-periodic domain, as vorticity carrying boundary layers are created near the walls.

Spontaneous spin-up

The difference between turbulence in a no-slip domain and flows on a double-periodic domain is perhaps most pronounced if one considers the global angular momentum,

$$L(t) := \int_{\Omega} (\mathbf{r} \wedge \mathbf{u}(t, \mathbf{r})) \cdot \mathbf{e}_3 \mathrm{d}A, \quad \mathbf{r} \in \Omega \tag{4.1}$$

where $\mathbf{r} = (x, y)$ and unit vector $\mathbf{e}_3 \perp \Omega \subset \mathbb{R}^2$. This quantity is irrelevant on a double-periodic domain, whereas it is intricately linked to the phenomenology on a no-slip domain. In decaying turbulence in the square domain $\mathcal{D}$, a sudden growth to peak values of the angular momentum may occur. The phenomenon is a consequence of the self-organization of the flow into a single huge vortex structure and is known as spontaneous spin-up, described by Clercx *et al.* [25] and Maassen *et al.* [86]. Spontaneous

in this case refers to the fact that the observed phenomenology is an inherent characteristic of the turbulence itself, independent of the initial conditions. Kraichnan [74] predicted this type of behavior in the presence of a finite domain-size and used the term Bose-Einstein condensation, referring to the condensation of energy in the lowest accessible wave number mode. Sommeria [129] made early experimental observations of the phenomenon, followed by Paret and Tabeling [107] and Maassen *et al.* [86]. The spin-up phase is followed by a slow decline of the absolute value of the global angular momentum, $|L(t)|$, as $t \to \infty$, caused by viscous dissipation.

In this Chapter it is shown that spin-up-like phenomena may also be observed if the time-dependent forcing $q(t, \mathbf{x})$ is applied to generate a two-dimensional fluid flow from a set of zero initial conditions, $\omega_0(\mathbf{x}) = 0$. Here, the Reynolds number, denoted as Re_*, is based on the time-averaged root-mean-square velocity scale $U = (1/d)\,\langle \|\mathbf{u}\|_{2,\mathcal{D}} \rangle$, achieving a value on the order of $Re_* \simeq 3000$. For these stochastically forced flows, the phenomenology during a spin-up event is again dominated by the generation of a large circulation cell, occupying most of the interior of the domain. However, contrary to the decaying case, in the forced flow several consecutive events occur of rapid build-up and collapse of the circulation cell, where a spontaneous sign reversal of the angular momentum of the flow is possible from one event to the next. Each collapse of the cell is caused by the destabilizing effect of intense boundary layers and is associated to a decrease in the value of the absolute angular momentum. Consequently, the evolution of other relevant integral quantities, such as the energy, $E(t)$, or enstrophy, $Z(t)$, is strongly influenced by the spin-up events. Shear and normal stresses exerted on the fluid, resulting from the interaction of the emerging central cell with the domain boundaries are thought to cause the spin-up phenomenon in the decay scenario [25, 26, 86], which is confirmed in the forced case.

The flow grows to large-scale order, lives relatively undisturbed for some time and then dies with a collapse back to disorder, after which a new phase of growth may begin. There seems to be an analogy with convection systems. The spontaneous sign-reversals of a large circulation cell are similar to the spontaneous sign-reversals of a feature known as 'the wind' in confined thermal convection, described by Niemela *et al.* [97], see also the review article by Kadanoff [66]. However, while these authors speculated upon the cause of the observed large-scale instabilities, the definite cause was not established. Our computations suggest it is the viscous boundary layers that play a crucial role in these issues.
Furthermore, the production of vorticity in viscous boundary layers, due to the no-slip boundary condition, serves as a natural energy dissipation mechanism, as was observed earlier for the initial energy dissipation in decaying flows on a circular no-slip domain by Li *et al.* [79]. Our observations highlight a sharp difference with continuously forced flows in a double-periodic domain, where often some kind of additional energy dissipation is applied to achieve a stationary energy balance, as, e.g., the Ekman damping applied by Maltrud and Vallis [87] or the hypo-viscosity operator applied by Borue [15], where an inverse dissipation operator is added to the equations of motion with $\nu\Delta^{-p}$, for $p = 4, 6, 8, \ldots$.

An intriguing property of the spin-up state is an approximate similarity behavior of $E(t)$ and $|L(t)|$, enabling the definition of a global energy saturation time. If this time approaches unity the kinetic energy of the flow is mainly carried within a large circulation cell, away from the dissipative scales of motion, from which one derives the usual

turbulence time scale τ based upon the ensemble-averaged enstrophy dissipation [102]. Certain bounds on the velocity and vorticity L_2-norms must be fulfilled to obtain the afore mentioned equality. Associated with the energetic upper bound, a domain-sized uniform rotation plays a special role as limiting process. The energy saturation time is subsequently shown to exhibit a scaling behavior with τ and, on the other hand, with the integral-scale Reynolds number.

Chapter outline

The phenomenology of intermediate Reynolds number flows, driven by a stochastic time-dependent forcing, is discussed in Section 4.2. Bounds on an instantaneous energy saturation time and its averaged version are derived and shown to be obeyed in the computational results in Section 4.3.
Coupling back to earlier work on decaying flows in different no-slip domains, we derive several evolution inequalities which the domain integrated angular momentum should satisfy and combine these inequalities with scaling ideas in Section 4.4. Finally, we briefly discuss the difference of the phenomenology on a no-slip domain with that on a double-periodic domain in Section 4.5.
Because the behavior of $L(t)$ is such an important indicator of the phenomenology, we first discuss the evolution balance of the angular momentum, before proceeding with the analysis of computational results.

4.1.1 Angular momentum balance equation

Using generalized partial integration and the no-slip boundary condition it can be shown that an equivalent definition of $L(t)$ exists in terms of the vorticity, $\omega(t,\mathbf{r})$, on the bounded domain $\Omega \subset \mathbb{R}^2$,

$$\int_\Omega xv(t,\mathbf{r}) - yu(t,\mathbf{r})\,\mathrm{d}A = -\frac{1}{2}\int_\Omega r^2\omega(t,\mathbf{r})\mathrm{d}A, \quad \mathbf{r}\in\Omega \tag{4.2}$$

where $r = |\mathbf{r}|$. A balance equation for $L(t)$ can be derived, using either the right hand side of equation (4.2) and the vorticity equation, see e.g. Saffman [123], or definition (4.1) and the primitive variable Navier-Stokes equations. Let us stick to the former, obtaining

$$\dot{L}(t) = -\frac{\nu}{2}\int_\Omega r^2\Delta\omega\mathrm{d}A - \frac{1}{2}\int_\Omega r^2 q\mathrm{d}A.$$

Observe that, for $\Omega = \mathcal{D}$ and by generalized partial integration, the last line can be reworked further into

$$\dot{L}(t) = -\frac{\nu}{2}\oint_{\partial\mathcal{D}} r^2\frac{\partial\omega}{\partial n}\mathrm{d}s - \nu\int_{\mathcal{D}}\mathbf{r}\cdot\nabla\omega\mathrm{d}A - \frac{1}{2}\int_\Omega r^2 q\mathrm{d}A. \tag{4.3}$$

Renaming the third term in the right hand side of balance (4.3) to $M(t)$, we substitute the expression

$$q(t,\mathbf{r}) = \sum_{a\le|\mathbf{k}|\le b} q(t,\mathbf{k})e^{\imath\mathbf{k}\cdot\mathbf{r}},$$

to obtain

$$M(t) = -\tfrac{1}{2} \sum_{a \le |\mathbf{k}| \le b} \int_{\mathcal{D}} (x^2 + y^2) q(t, \mathbf{k}) e^{i\mathbf{k}\cdot\mathbf{r}} \mathrm{d}A. \tag{4.4}$$

Using the classical integration-by-parts formula one obtains, with $\mathcal{D} = [-1, 1]^2$,

$$\int_{[-1,1]^2} x^2 e^{\imath(k_1 x + k_2 y)} \mathrm{d}A = \left(\frac{2}{k_2} \sin k_2\right) \left[\left(\frac{2}{k_1} - \frac{4}{k_1^3}\right) \sin k_1 + \frac{4}{k_1^2} \cos k_1\right],$$

which can be rewritten in terms of spherical Bessel functions of the first kind $j_n(k)$, for $n = 0$ and $n = 2$, see e.g. Arfken and Weber [5], such that one finds

$$M(t) = -\sum_{a \le |\mathbf{k}| \le b} q(t, \mathbf{k}) \sum_{\substack{i,\, j\, =\, 1 \\ i \ne j}}^{2} \frac{2}{3} j_0(k_i) \left(j_0(k_j) - 2 j_2(k_j)\right).$$

From computational results the torque was found to be an order of magnitude smaller than the change in angular momentum, $|M(t)| \ll |\mathrm{d}L(t)/\mathrm{d}t|$, and the correlation between these quantities was found to be insignificant. Henceforth, the evolution of $L(t)$ is assumed to be independent of the torque $M(t)$ associated to the external forcing and any occurring spin-up is indeed spontaneous.

4.2 Phenomenology

A time series of the normalized angular momentum $L'(t)$ during a $Re \simeq 3000$ computation, with other parameters as given in Table 4.1, is shown in Figure 4.1. The normalized quantity equals

$$L'(t) := \frac{L(t)}{\|\mathbf{r}\|_{2,\mathcal{D}} \|\mathbf{u}\|_{2,\mathcal{D}}}$$

where the denominator equals the angular momentum $L_u(t)$ of a uniform rotation with kinetic energy $E(t)$. The spin-up effect is clearly recognizable and the global rotation associated with peaks in $|L'(t)|$ changes sign spontaneously several times, as in, e.g., the interval $t \in [800, 1000]$. It is mainly the viscous normal vorticity gradient, integrated over $\partial\mathcal{D}$ in balance (4.3), that drives the spin-up effect. This corresponds to observations of spin-up of turbulent flow, decaying from a set of random initial conditions under no-slip boundary conditions in $\mathcal{D}$ [25]. The spin-up is caused by self-organization of the flow into a large vortex structure. A similar self-organization process is observed for decaying flows [25, 26, 86], but here the initial stage of spin-up may include a large number of smaller eddies superimposed on a background rotation of specific sign. However, due to the continuous forcing of the flow, increasing the energy of the large vortex structure, the configuration is unstable and eventually breaks down. The break-down process is catalyzed by the viscous boundary layers, which are created at the domain walls. As these boundary layers detach from the wall and interact with the flow in the interior, the central vortex is destabilized and collapses, causing a rapid decrease of the quantity $|L'(t)|$. In the resulting irregular flow another vortex core, possibly with opposite-signed vorticity, may become the new focus for self-organization. In Figure 4.2 three consecutive vorticity snapshots show a break-down and a subsequent reappearance, with opposite sign, of a large coherent structure.

Re_*	ν	U	A_0	R	Δt	N
3000	5.0×10^{-4}	1.5	6.0	0.98	3.4×10^{-4}	161
5000	2.0×10^{-4}	1.0	1.0	0.98	1.35×10^{-4}	257

Table 4.1: *Model parameters as used in the computations, grouped in flow parameters Re_*, ν and flow scale U, forcing parameters A_0 and R and the time step Δt and spatial resolution N, which is equal in both directions. All computations run up to $T = 1000$.*

Corresponding to the snapshots in Figure 4.2, $L'(t)$ is positive at $t = 800$, negative at $t = 1000$ and close to zero during the highly irregular motion at $t = 900$. Note that the Figures are shown in dimensionless simulation time units. One could reformulate time in terms of a turnover time of the largest eddies, T_e, which is defined by means of the maximum measured root-mean-square velocity and the half-width of the domain, $d/2$,

$$T_e = \frac{2}{d \max_t \|\mathbf{u}\|_{2,\mathcal{D}}}.$$

As such, the computations shown in Figure 4.1 run up to $300T_e$.

The global phenomenological picture is in sharp contrast with observations of forced 2D turbulence on a double-periodic domain. There the usual end state is a domain filling dipole structure, which was first observed in DNS by Hossain *et al.* [64] and later by Smith and Yakhot [127, 128]. Strong deviations from the double-periodic setting, due to the presence of boundary layers, were already observed by Li *et al.* [79], in the case of decaying flow on a circular no-slip domain. These authors noted the change in early-time dissipative properties of the flow, under the action of boundary-layer development. For the forced, wall-bounded flows considered here, it is found that the no-slip walls provide a natural energy dissipation mechanism, as the kinetic energy of the flow did not diverge during our computations (see Figure 4.4). The boundary layers are sources of opposite-signed vorticity, as compared to the central vortex. Hence, these structures are sources of enstrophy $Z(t)$, which is proportional to the destruction term in the global energy balance, see also Section 1.3,

$$\dot{E}(t) = -2\nu Z(t) + (\boldsymbol{f}, \mathbf{u}), \tag{4.5}$$

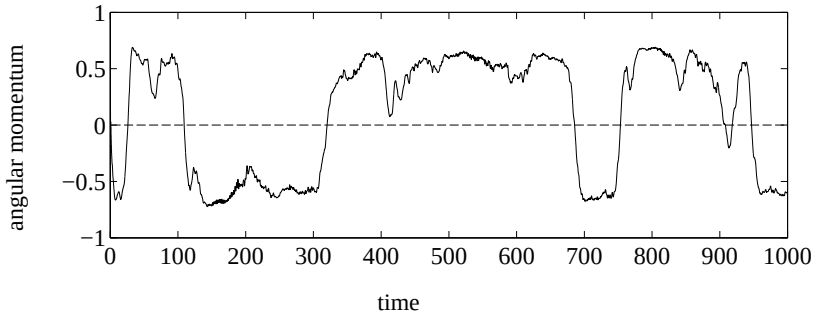

Figure 4.1: *Evolution of the normalized angular momentum $L'(t)$, showing distinct phases of spin-up.*

where the inner product term in the right-hand side represents the energy input due to the forcing. Thus the boundary layers enhance dissipation properties of the flow in two ways; by production of $Z(t)$ on one hand and by causing instability of the central vortex on the other hand.

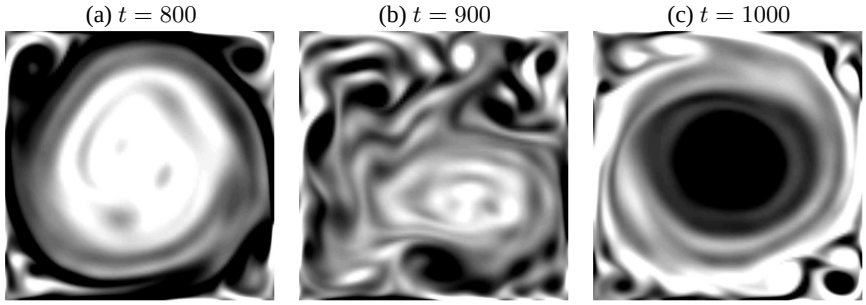

Figure 4.2: *Snapshots of the vorticity evolution during the sign reversal of a large monopolar vortex structure for $Re \simeq 3000$, with vorticity levels ranging from $\omega < -5$ (black) to $\omega > 5$ (white).*

To obtain a more precise description of the encountered coherent structures, the Weiss function $Q_w(t, \mathbf{x})$ is used [150]. This is essentially the Jacobian determinant of the velocity gradient tensor,

$$Q_w(t, \mathbf{x}) := -4 \det(\nabla \mathbf{u}).$$

Depending on the sign of $Q_w(t, \mathbf{x})$ regions in the flow are interpreted as either hyperbolic, $Q_w(t, \mathbf{x}) > 0$, or elliptic, $Q_w(t, \mathbf{x}) < 0$. Because $Q_w(t, \mathbf{x})$ equals the magnitude of the squared rate of strain minus the squared vorticity, $Q_w(t, \mathbf{x}) = 2(|\nabla \mathbf{u}|^2 - \omega^2)$, flow behavior is assumed to be strain-dominated in hyperbolic regions and vorticity-dominated in elliptic regions, corresponding to coherent structures, whereas $Q_w(t, \mathbf{x}) = 0$ denotes the separatrix between the former two. Care should however be taken with respect to the validity of this interpretation throughout the flow, as was argued by Basdevant and Philipovitch [9] and earlier by Weiss [150]. The main assumption that $\nabla \mathbf{u}$ should vary slowly with $\nabla \omega$, implying that the vorticity gradients are determined locally by the eigenvalues of $\nabla \mathbf{u}$ and allowing a characterization in terms of hyperbolic and elliptic behavior, seems to be satisfied only in vortex cores and so-called saddle points. Henceforth, the area of applicability of $Q_w(t, \mathbf{x})$ is sharply reduced.
Corresponding to the snapshots of Figure 4.2, three snapshots of $Q_w(t, \mathbf{x})$ are presented in Figure 4.3. Clearly, at $t = 800$ and $t = 1000$ the elliptic vortex core is surrounded by strain-dominated flow, whereas the roll-up of boundary layers in the corners creates small secondary vortices. The remains of a large elliptic core occupy the lower right quadrant at $t = 900$, at which $L(t) \simeq 0$. During this phase the influence of the forcing is more pronounced, as is visible in the presence of small, relatively weak elliptic structures throughout the flow. The observations above seem to complement the experimental results by Paret and Tabeling [107], in which a large circulation cell dominated the flow in electromagnetically driven thin fluid layer experiments. Following the theoretical predictions by Kraichnan [74], this type of flow was referred to as a condensation regime, suggesting that it occurs when an energy cascade from smaller to larger length scales reaches the domain size d in a finite domain. Due to the loss of stratification in the experiments caused by three-dimensional mixing effects,

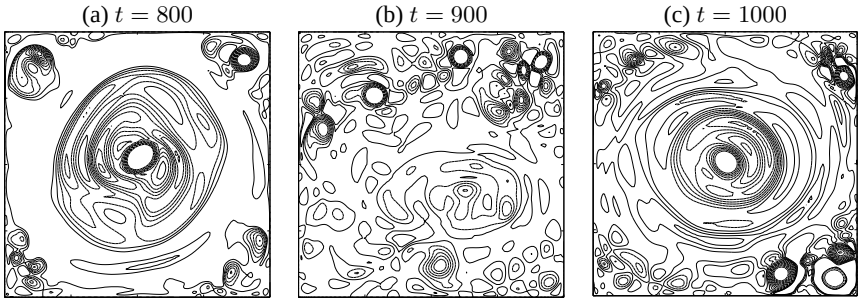

Figure 4.3: *Contour plots of the Weiss function $Q_w(t, \mathbf{x})$, corresponding to Figure 4.2. Dashed lines represent $Q_w(t, \mathbf{x}) < 0$, solid lines $Q_w(t, \mathbf{x}) > 0$ and contour increments in all plots are 10.*

the duration of the experiments was limited and it remained unclear what the long time evolution of the condensation regime would be. Although the formation mechanism for such a circulation cell is poorly understood, our observations suggest that the viscous boundary layers play a crucial role in its development. Henceforth, stability of this type of flow seems, even for modest Re, very unlikely under the action of a time-dependent force $\boldsymbol{f}(t, \mathbf{x})$ in a domain equipped with the no-slip conditions.

On the contrary, it was shown in the previous Chapter that if a time-independent forcing $\boldsymbol{f}(\mathbf{x})$ is applied, statically forcing the wave number $k_f = 6$ for $\nu = 1/2000$, a global circulation cell appears and remains stable for long times, $T > 10^3$. Such a stationary forcing mechanism closely resembles the laboratory experiments by Sommeria [129] and the computational results confirm his experimental observations in the limit $Rh \to \infty$ (no bottom friction), where Rh is an inverse bottom friction parameter. In this case it is thought that the local structure of $\boldsymbol{f}(\mathbf{x})$ prevents a destabilization of the flow, leaving the central cell largely intact. However, it was also argued in the previous Chapter that if initial noise is present, as is likely to be the case during a laboratory experiment, symmetry breaking may eventually occur, possibly leading to a different flow regime. The value of the viscosity parameter plays an important role in these issues, where stability of the central circulation cell becomes less likely for decreasing values of ν.

4.3 Similarity regime

A simple physical idea follows from the observation that the energy scales with velocity squared, and the absolute angular momentum scales with a finite length times velocity,

$$E(t) \propto U^2, \quad |L(t)| \propto \ell U.$$

Hence, on dimensional grounds, one can define the time

$$\gamma := \frac{\left|\int_{\mathcal{D}} r^2 \omega(t,\mathbf{r}) \mathrm{d}A\right|}{\|\mathbf{u}\|_{2,\mathcal{D}}^2}, \tag{4.6}$$

where $\gamma = \mathcal{O}(1)$ implies a strong similarity in the evolution of $E(t)$ and $|L(t)|$, which seems to coincide with a self-organization of the flow into a large vortex structure. After some transient behavior, this similarity regime indeed occurs in the computational data, as can be seen in the upper graph of Figure 4.4. More clearly, it follows from the evolution of γ, shown in the lowest graph in Figure 4.4. After some transient behavior, which is omitted in the graph, the value of γ in the computational results seems bounded close to unity. Indicating approximate similarity in the evolution of $E(t)$ and $|L(t)|$, this seems to coincide with flow self-organization in the interior of $\mathcal{D}$, into a coherent vortex structure. Furthermore, assuming that $E(t)$ remains finite, as is the case in our computations, $\gamma \to 0$ refers to the irregular behavior associated to the break-down and possible sign reversal of this coherent vortex. If one demands that γ is a constant of the order unity $\gamma = \mathcal{O}(1)$, some bounds on the energy and enstrophy should be fulfilled to meet this requirement; let us cast these bounds in the form of a lemma

Lemma 4.3.1. *If $\gamma \in \mathbb{R}$ a constant of order unity, one must have*

$$\|\mathbf{u}\|_{2,\mathcal{D}} \leq \sqrt{2C_0(\mathcal{D})} \quad \textit{and} \quad \|\nabla \mathbf{u}\|_{2,\mathcal{D}} > \sqrt{2C_1(\mathcal{D})} \tag{4.7}$$

for domain-dependent constants $C_0(\mathcal{D}) \simeq 5.3$ and $C_1(\mathcal{D}) \simeq 26.3$, setting $\lambda_1 = \left(2\pi^2/d^2\right)$.

Suppressing the proof of lemma 4.3.1 until the following Subsection, both bounds are seen to be crudely satisfied in Figure 4.4, where $C_1(\mathcal{D})$ is indicated in the lower graph, whereas $C_0(\mathcal{D})$ lies outside the scale of the upper graph. It can be shown that the uniform rotation

$$\mathbf{u}_u(\mathbf{x}) = \frac{2}{\gamma}(-y, x), \quad \text{for} \quad \mathbf{x} \in \mathcal{D}, \quad \gamma = 1,$$

has a global kinetic energy which is exactly equal to $C_0(\mathcal{D})$. However, such a flow is not compatible with the no-slip condition, which demands that $\mathbf{u}_u(\partial\mathcal{D}) = 0$. Hence, γ is no longer close to unity when $E(t) \to C_0(\mathcal{D})$, which is confirmed in the upper graph of Figure 4.4, where the energy in the similarity regime is bounded well below $C_0(\mathcal{D})$.

Clercx *et al.* [26] noted that on a circular domain $\mathcal{C}$, for a given energy, $L(t)$ is maximized under uniform rotation. Consequently, the amount of spin-up in forced turbulence on $\mathcal{C}$ was expressed as a percentage of the angular momentum in uniform rotation. For the computational results presented above, uniform rotation contained in the largest circular sub-domain $B_R \subset \mathcal{D}$, where the radius R is slightly smaller than $(d/2)$, seems

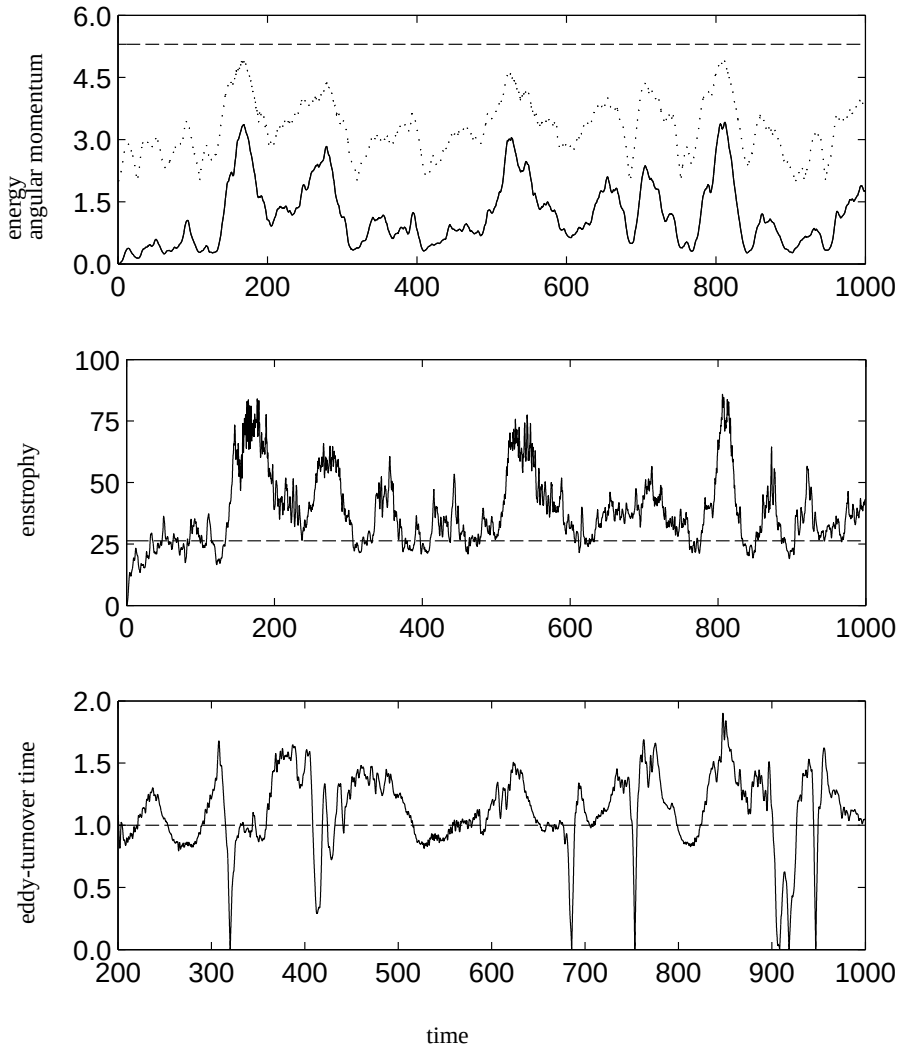

Figure 4.4: *Similarity in the behavior of the kinetic energy (solid line) and the absolute angular momentum, shifted to* $|L(t)| + 2$*, (dotted line) in the upper graph. The dashed line corresponds to the constant* $C_0(\mathcal{D})$ *of lemma 4.3.1. The middle graph shows the enstrophy (solid line) and the constant* $C_1(\mathcal{D})$ *of lemma 4.3.1, (dashed) where we set* $\lambda_1 = (2\pi^2/d^2)$*. The lower graph displays time scale* γ*, omitting transients, where the dashed line corresponds to the equality* $E(t) = |L(t)|$*.*

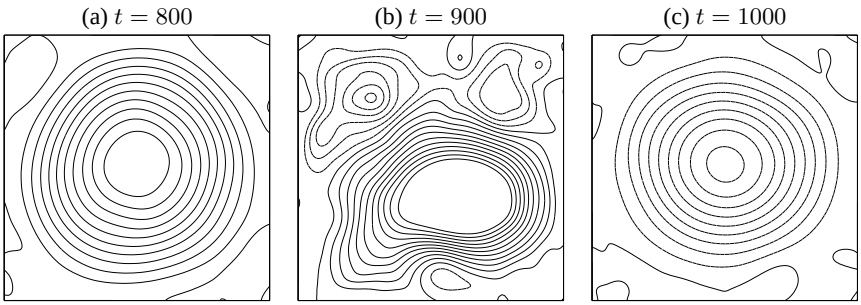

Figure 4.5: *Normalized stream function contour plots, corresponding to the snapshots in Figures (4.2) and (4.3). Contours range from -1 to 1 with an interval of 0.1 and dashed lines represent negative values.*

to be a reasonable first-order approximation at times with strong spin-up of the flow. As shown in three consecutive contour-plots in Figure 4.5, the stream function $\psi(t, \mathbf{x})$ is nearly circular at $t = 800$ and, albeit slightly weaker, at $t = 1000$. These plots bear a strong resemblance with the stream function in the maximum entropy state in decaying turbulence, under zero-viscosity ($\nu = 0$), as obtained by Pointin and Lundgren [109], and later by Chavanis and Sommeria [22], for a bounded square domain.

It is perhaps surprising that the lower bound in lemma 4.3.1 is on the enstrophy rather than the energy. However, this bound can be interpreted as a critical value for the strength of the large coherent structure, which should be attained before the similarity regime can occur.

Geometrical bounds on $E(t)$ and $Z(t)$

We explain the results of lemma 4.3.1, under the assumption $\gamma = \mathcal{O}(1)$, beginning with a general lemma, for a bounded domain Ω.

Lemma 4.3.2. *For $\mathbf{r} \in \Omega$ and constant $\lambda_1 > 0$ the following inequalities hold*

$$|L(t)| \leq \|\mathbf{r}\|_{2,\Omega}\|\mathbf{u}\|_{2,\Omega} \tag{4.8}$$

$$2|L(t)| \leq \|\mathbf{r}\|^2_{4,\Omega}\|\omega\|_{2,\Omega} \tag{4.9}$$

$$2|L(t)| \leq \lambda_1^{-1/2}\|\mathbf{r}\|^2_{4,\Omega}\|\nabla\omega\|_{2,\Omega}. \tag{4.10}$$

Proof of Lemma 4.3.2. Observe first that

$$|L(t)| \leq \int_\Omega |(\mathbf{r} \wedge \mathbf{u}) \cdot \mathbf{e}_3| \mathrm{d}A \leq \int_\Omega |\mathbf{r}||\mathbf{u}| \mathrm{d}A \leq \|\mathbf{r}\|_{2,\Omega}\|\mathbf{u}\|_{2,\Omega},$$

establishing (4.8) while using a property of the absolute value of the exterior product and the classical Schwarz inequality. With the vorticity formulation for the angular momentum and $r = |\mathbf{r}|$, one can apply the Hölder inequality,

$$2|L(t)| \leq \int_\Omega |r^2\omega(t, \mathbf{r})| \mathrm{d}A \leq \|r^2\|_{p,\Omega}\|\omega\|_{q,\Omega}. \tag{4.11}$$

For $p = q = 2$ one has inequality (4.9), a mere application of the Poincaré-Friedrichs (P-F) inequality of Section 1.2.2 yields the other desired result (4.10), noting that $\|r^2\|_{2,\Omega} = \|\mathbf{r}\|^2_{4,\Omega}$. □

Now we are ready to proceed with a proof of our bounding constants in the domain $\mathcal{D}$.

Proof of Lemma 4.3.1. With (4.6) one can replace $|L(t)|$ by $\gamma E(t)$ in inequality (4.8),

$$\frac{\gamma}{2}\|\mathbf{u}\|^2_{2,\mathcal{D}} \leq \|\mathbf{r}\|_{2,\mathcal{D}}\|\mathbf{u}\|_{2,\mathcal{D}}$$

divide both sides by $(\gamma/\sqrt{2})\|\mathbf{u}\|_{2,\mathcal{D}}$ and square the result, to obtain

$$E(t) \leq C_0(\mathcal{D}) = \frac{2}{\gamma^2}\|\mathbf{r}\|^2_{2,\mathcal{D}},$$

where $\|\mathbf{r}\|^2_{2,\mathcal{D}} = (d^2/\sqrt{6})^2$, such that $C_0(\mathcal{D}) = (16/3)(1/\gamma)^2(d/2)^4$ and where d is the domain length, confirming the first inequality of lemma 4.3.1.

Next, we argue that the enstrophy, $Z(t)$, should be greater than a second domain dependent constant. Starting with the observation that, with the P-F inequality, one could obtain either

$$E(t) \leq \frac{2}{\gamma^2}\|\mathbf{r}\|^2_{2,\mathcal{D}} \leq \lambda_1^{-1} Z(t), \tag{4.12}$$

or

$$E(t) \leq \lambda_1^{-1} Z(t) \leq \frac{2}{\gamma^2}\|\mathbf{r}\|^2_{2,\mathcal{D}},$$

neither of which can be excluded beforehand. Let us, however, continue with the last line, rewriting it as

$$\|\omega\|_{2,\mathcal{D}} \leq \frac{2\lambda_1^{1/2}}{\gamma}\|\mathbf{r}\|_{2,\mathcal{D}}.$$

Now, we apply this line to the inequality (4.9) of Lemma 4.3.2,

$$|L(t)| \leq \tfrac{1}{2}\|\mathbf{r}\|^2_{4,\mathcal{D}}\|\omega\|_{2,\mathcal{D}} \leq \frac{\lambda_1^{1/2}}{\gamma}\|\mathbf{r}\|_{2,\mathcal{D}}\|\mathbf{r}\|^2_{4,\mathcal{D}}.$$

As a last step we use our scaling relation (4.6) and replace $|L(t)|$ by $\gamma E(t)$ in the last line, ending up with

$$E(t) \leq \frac{\lambda_1^{1/2}}{\gamma^2}\|\mathbf{r}\|_{2,\mathcal{D}}\|\mathbf{r}\|^2_{4,\mathcal{D}},$$

which is inconsistent with our earlier bound on the energy. So we should prefer relation (4.12), obtaining instead a lower bound on the enstrophy

$$Z(t) \geq C_1(\mathcal{D}) = \frac{2}{\gamma^2}\lambda_1\|\mathbf{r}\|^2_{2,\mathcal{D}}.$$

□

4.3.1 Asymptotic scaling

Turning our attention once more to equality (4.6), we are interested in the average

$$\tilde{\gamma} := \lim_{T\to\infty} \frac{1}{T} \int_{t_0}^{T} \frac{2|L(t)|}{\|\mathbf{u}\|_{2,\mathcal{D}}^2} \mathrm{d}t, \quad 0 < t_0 < T \leq \infty, \tag{4.13}$$

where t_0 can be chosen for convenience to exclude initial transients. Phrased differently, $\tilde{\gamma}$ is a characteristic time for the similarity regime of energy and angular momentum. Thus if the value of the similarity time is on the order of unity, $\tilde{\gamma} = \mathcal{O}(1)$, a situation is achieved where the energy is, on average, carried by a global rotation. For the computational data in Figure 4.4 the estimate is $\tilde{\gamma} \simeq 1.18$.

Danilov and Gurarie [32] remarked that 2D turbulence is a multi-scale phenomenon, roughly characterizable by a well-separated enstrophy saturation time τ and a corresponding time for the energy saturation. It is generally assumed that τ is the most relevant time characterizing the flow dynamics in the direct enstrophy cascade regime [102]; from dimensional arguments it follows from the enstrophy dissipation as $\tau \equiv \chi^{-1/3}$, see also Section 1.3. However, a logarithmic correction may be necessary, based on corrections applied to the spectrum in the direct cascade part of the inertial range by Kraichnan [75],

$$\tau \equiv \chi^{-1/3} \ln \ell_f / \ell_\chi,$$

where ℓ_χ denotes the viscous dissipation length and ℓ_f the forcing length.
Now it is tempting to compare the time for the similarity regime $\tilde{\gamma}$ with the enstrophy saturation time τ. When the phenomenology is dominated by a large circulation cell, see Section 4.2, integral flow properties like the energy, $E(t)$, and angular momentum, $L(t)$, are thought to be carried by scales that are much larger than ℓ_χ. Thus it is expected from physical reasoning that $\tilde{\gamma} \gg \tau$, as was assumed by Danilov and Gurarie [32] for τ and the energetic saturation time scale. Indeed, it can be shown that there exists a lower bound relation between $\sup \tilde{\gamma}$ and τ, which is, however, less pronounced than physical intuition suggests.
Before we proceed we should make an important preparation, assuming that stationary statistical solutions to the problem exist, such that the ensemble average of L_2-norms remains finite, see Section 1.2.2. Replacing time averages with these ensemble-averages, note that, from equation (4.13) one obtains

$$\sup \tilde{\gamma} \geq \int \frac{2\|\mathbf{r}\|_{2,\mathcal{D}}}{\|\mathbf{u}\|_{2,\mathcal{D}}} \mathrm{d}\mu(\mathbf{u}) \geq 2\lambda_1 \|\mathbf{r}\|_{2,\mathcal{D}} \int \|\Delta\mathbf{u}\|_{2,\mathcal{D}}^{-1} \mathrm{d}\mu(\mathbf{u}),$$

where the Poincaré-Friedrichs inequality was applied twice. Upon noting that the function $g(x) = x^{-1}$ is convex for $x \geq 0$, i.e. $g''(x) > 0$, the Jensen inequality, stating that $\langle g(x) \rangle \geq g(\langle x \rangle)$, may be applied. Subsequently applying the Schwarz inequality yields, respectively,

$$\int \|\Delta\mathbf{u}\|_{2,\mathcal{D}}^{-1} \mathrm{d}\mu(\mathbf{u}) \geq \left(\int \|\Delta\mathbf{u}\|_{2,\mathcal{D}} \mathrm{d}\mu(\mathbf{u}) \right)^{-1} \geq \left(\int \|\Delta\mathbf{u}\|_{2,\mathcal{D}}^2 \mathrm{d}\mu(\mathbf{u}) \right)^{-1/2}.$$

Using that $\|\Delta\mathbf{u}\|_{2,\mathcal{D}} = \|\nabla\omega\|_{2,\mathcal{D}}$ and applying $\tau^{-3} = \nu\langle\|\omega\|_{2,\mathcal{D}}^2\rangle$, with the last line one obtains a scaling relation between τ and $\sup\tilde{\gamma}$, involving only domain-dependent constants,

$$\sup \tilde{\gamma} \geq 2\lambda_1^{3/2} \|\mathbf{r}\|_{2,\mathcal{D}} \nu^{1/2} \tau^{3/2}. \tag{4.14}$$

For $\nu = 1/2000$, the scaling (4.14) is compared with computational data in Figure 4.6. However, for the computational data ordinary time-averages were taken and the precise relation of these quantities with respect to the ensemble average is unclear. The result (4.14) does not seem to satisfy the initially expected $\tilde{\gamma} \gg \tau$. It is thought, however, that the complex interaction of the largest scales of motion with the dissipative scales, during a collapse of the large monopolar vortex, makes the average characteristics of these extremes no longer well-separated throughout the flow-evolution. Hence, it is not likely that a sharper bound linking $\tilde{\gamma}$ and τ than the bound (4.14) can be obtained.

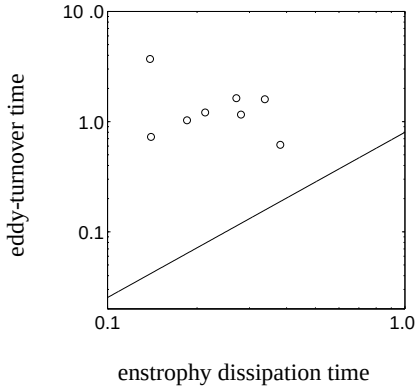

Figure 4.6: *Lower bound relation (4.14), between the enstrophy dissipation time τ and the eddy-turnover time γ, where we put $\lambda_1 = (2\pi^2/d^2)$ (solid line) and computational data (circles) in a log-log plot, for $\nu = 1/2000$. Each marker represents one computation, under slightly different forcing-parameter values.*

Finally, it should be noted that one can also derive a lower bound on $\sup \tilde{\gamma}$ in terms of the generalized Grashof number $\tilde{Gr}$, introduced in Section 2.2. Recall from Section 1.3 that, by a standard calculation [50], one obtains the energy inequality

$$\frac{\mathrm{d}}{\mathrm{d}t}\|\mathbf{u}\|_{2,\mathcal{D}} + \nu\lambda_1\|\mathbf{u}\|_{2,\mathcal{D}} \leq \|\boldsymbol{f}\|_{2,\mathcal{D}},$$

where the P-F inequality was used in the left-hand side and the Schwarz inequality in the right-hand side. Hence, one obtains

$$\langle\|\mathbf{u}\|_{2,\mathcal{D}}\rangle \leq \frac{1}{\nu\lambda_1}\langle\|\boldsymbol{f}\|_{2,\mathcal{D}}\rangle, \tag{4.15}$$

where the brackets $\langle\cdot\rangle$ denote ensemble averaging. Now one has, by definition (2.10), the sequence

$$\sup\tilde{\gamma} \geq \frac{2\|\mathbf{r}\|_{2,\mathcal{D}}}{\langle\|\mathbf{u}\|_{2,\mathcal{D}}\rangle} \geq \frac{2\nu\lambda_1\|\mathbf{r}\|_{2,\mathcal{D}}}{\langle\|\boldsymbol{f}\|_{2,\mathcal{D}}\rangle}, \tag{4.16}$$

a lower bound on $\sup\tilde{\gamma}$ entirely in terms of external control parameters, assuming that the average of the forcing is controllable. In computations, equality in the lower bound (4.16) will not be achieved, because the value of $\tilde{\gamma}$ is assumed to be on the order of unity, $\tilde{\gamma} = \mathcal{O}(1)$, whereas the right hand side of inequality (4.16) is on the order of the kinematic viscosity, $\mathcal{O}(\nu)$.

4.4 Angular momentum scaling and inequalities

Scaling on a circular domain

In this Section we briefly step away from the main topic of forced flows in a square domain, to examine the angular momentum scaling behavior for a decaying flow in a circular no-slip domain. The torque of a fluid in a circular tank $\mathcal{C}$ of radius R containing a fluid spinning at angular velocity Ω_0, in terms of the Reynolds number, Re, and the generalized Grashof number, Gr. Using the traditional Prandtl estimate on the thickness of the viscous boundary-layer,

$$\delta_{bl} \simeq (\nu/\Omega_0)^{1/2},$$

see, e.g., Landau and Lifschitz [76]. The torque of the fluid equals

$$\dot{L}(t) = \nu R \int_0^{2\pi} \omega(\partial\mathcal{C}) \mathrm{d}s,$$

where we can obtain $\omega(\partial\mathcal{C})$ from the Prandtl estimate and the fact that the total circulation of the flow, defined as

$$\Gamma = \int_{\mathcal{C}} \omega \mathrm{d}A,$$

must equal zero. Because $\omega = \Omega_0$, one has for the circulation in the interior Γ_{int} and for the circulation in the boundary layer Γ_{bl}, with $\Gamma = \Gamma_{int} + \Gamma_{bl} = 0$ and $\Gamma_{int} = \pi R^2 \Omega_0$, that

$$\Gamma_{bl} = -\pi R^2 \Omega_0 = \omega(\partial\mathcal{C}) \pi \int_{R-\delta}^{R} r \mathrm{d}r.$$

Disregarding terms involving δ^2, one obtains that $\omega(\partial\mathcal{C}) \sim -R\Omega_0/\delta$, which leads to

$$\dot{L}(t) \sim 2\pi R^2 \Omega_0^{3/2} \nu^{1/2},$$

or, with $Re \sim RU/\nu$ and $U = \Omega_0 R/2$, to

$$\dot{L}(t) \sim \nu^2 R^{-1} Re^{3/2}. \tag{4.17}$$

Summarizing, the dimensional analysis tells us that $\dot{L}(t)$ scales with a constant of order $\mathcal{O}\left(\nu^{1/2}\right)$.

Now we return to the global angular momentum balance, assuming that the external forces are either not present or do not result in a net contribution to this balance, leaving us again with

$$\dot{L}(t) = \nu R \int_{\partial\mathcal{C}} \omega(t, \mathbf{r}) \mathrm{d}s.$$

Note that the pressure contribution is zero on the boundary $\partial\mathcal{C}$, as the innerproduct $(\mathbf{r} \cdot \mathrm{d}\mathbf{s})$ vanishes at $\partial\mathcal{C}$.
Recall from Section 1.2.2 the spaces $L_p(\partial\mathcal{C})$, equipped with norms $\|\cdot\|_{L_p(\partial\mathcal{C})}$. Recall also from Section 1.2.2 the Sobolev trace embedding theorem, see also Adams [2],

yielding the immersion $W^{1,2}(\mathcal{C}) \hookrightarrow L_2(\partial\mathcal{C})$. For the constant C_0 this embedding theorem allows us to relate the norms on $L_2(\partial\mathcal{C})$ and $W^{1,2}(\mathcal{C})$ through the inequality

$$\|\omega\|_{2,\partial\mathcal{C}} \leq C_0 \left(\|\omega\|_{2,\mathcal{C}}^2 + \|\nabla\omega\|_{2,\mathcal{C}}^2\right)^{1/2}.$$

Observe furthermore that, by a property of the spaces $L_1(\partial\mathcal{C})$ and $L_2(\partial\mathcal{C})$, one has $\|\omega\|_{1,\partial\mathcal{C}} \leq \|\omega\|_{2,\partial\mathcal{C}}$. So let us pursue the following line of thought

$$\begin{aligned}
\nu R \int_{\partial\mathcal{C}} \omega(t,\mathbf{r})\mathrm{d}s &\leq \nu R\|\omega\|_{1,\partial\mathcal{C}} \\
&\leq \nu R\|\omega\|_{2,\partial\mathcal{C}} \\
&\leq \nu R C_0 \left(\|\omega\|_{2,\mathcal{C}}^2 + \|\nabla\omega\|_{2,\mathcal{C}}^2\right)^{1/2} \\
&\leq \nu R C_0 \left(1+\lambda_1^{-1}\right)^{1/2} \|\Delta\mathbf{u}\|_{2,\mathcal{C}},
\end{aligned}$$

where we used in the last line the fact that $\|\nabla\omega\|_{2,\mathcal{C}} = \|\Delta\mathbf{u}\|_{2,\mathcal{C}}$ and the P-F inequality. A mishap is that we do not have a direct bound on the quantity $\|\Delta\mathbf{u}\|_{2,\mathcal{C}}$, which is essentially the square root of the palinstrophy. To achieve the scaling 4.17, one must have that

$$\|\Delta\mathbf{u}\|_{2,\mathcal{C}} \propto Re^{1/2},$$

which would yield again $\dot{L}(t) \sim \mathcal{O}\left(\nu^{1/2}\right)$.
On the other hand, on a square no-slip domain for the case of unforced dipole-wall collisions, Clercx and van Heijst [28] observed a scaling behavior for the palinstrophy leading to

$$\|\Delta\mathbf{u}\|_{2,\mathcal{D}} \propto C_t Re^{3/4},$$

where C_t is a constant of order unity and dimension $1/t$. If the latter result would carry over to a circular domain, a combination with the above analysis yields that

$$\dot{L}(t) \leq \nu C_1 Re^{3/4}$$

with constant

$$C_1 = RC_0C_t\left(1+\lambda_1^{-1}\right)^{1/2}.$$

In this case our estimate would be slightly worse than the dimensional scaling results, as we now obtained that $\dot{L}(t)$ scales as most as $\mathcal{O}\left(\nu^{1/4}\right)$.

Results on a square domain

After Topping [141], we define in $\Omega = \mathcal{D}$ the non-negative excess quantity

$$Q(t) := \|\omega\|_{2,\mathcal{D}} - \lambda_1^{1/2}\|\mathbf{r}\|_{2,\mathcal{D}}^{-1}\left|L(t)\right|, \tag{4.18}$$

Referring to the previous Subsection, inequality (4.8) of lemma 4.3.2 implies, together with the P-F inequality, that $Q(t)$ is non-negative, $Q(t) \geq 0$. Certainly, we could also have used the second relation of lemma 4.3.2, inequality (4.9), which would have yielded a slightly smaller geometric constant, but for convenience we use here the constant in definition (4.18). The first quantity in the right-hand-side of (4.18) is the root-mean-square (rms) vorticity, the second quantity has the rms vorticity as its limit.

The quantity $Q(t)$ thus refers to the contributions to the rms vorticity that cannot be explained by a global rotation, it contains, e.g., contributions from viscous boundary layers or vorticity filaments, whence we refer to it as excess vorticity. Figure 4.7 shows the evolution of both $Q(t)$ and the rms vorticity, for the computational data shown earlier in Figure 4.4. The greatest difference between these quantities occurs during times with well developed circulation cell, e.g., around $t = 800$, whereas the difference is almost zero around $t = 900$ when the circulation cell has broken down.

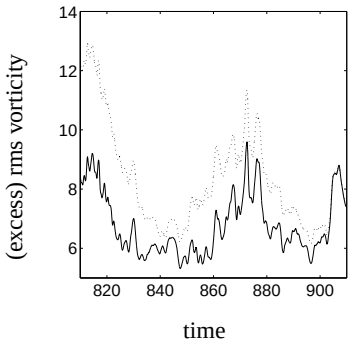

Figure 4.7: *Evolution of the excess vorticity, $Q(t)$, (solid line) and the rms vorticity, $\|\omega\|_{2,\mathcal{D}}$ (dotted line).*

Recall that the spaces $L_q(\partial\Omega)$ are equipped with norms $\|\cdot\|_{L_q(\partial\Omega)}$. Furthermore, one can define an instantaneous average enstrophy 'wavenumber', $\kappa_2(t) := H_2/H_1$, relating the enstrophy to its dissipation, where we denote $H_1 = \|\nabla\mathbf{u}\|_{2,\Omega}$ and $H_2 = \|\Delta\mathbf{u}\|_{2,\Omega}$. The wavenumber $\kappa_2(t)$ is of intrinsic interest, because it may characterize a dominant length in the direct enstrophy cascade regime, as noted by of Bartuccelli *et al.* [8], who defined the ratios H_n/H_{n-1} as so-called ladder inequalities, where higher rungs of the ladder, of order $n = 1, 2, \ldots$, pick up information during more violent, rarer events. Usually, a similar rms wavenumber is defined as $\kappa_1(t) := H_1/H_0$, where $H_0 = \|\mathbf{u}\|_{2,\Omega}$, which is a characteristic wavenumber for the energy of the flow. Now we can pose the following theorem;

Theorem 4.4.1. *In $\Omega = \mathcal{D}$, the square of side d, for domain dependent constant C_2, the evolution of the excess vorticity $Q(t)$ is bounded as*

$$\dot{Q}(t) \leq \nu\kappa_2(t)\left(C_2\|\nabla\omega\|_{2,\partial\mathcal{D}} + \|\nabla\omega\|_{2,\mathcal{D}}\right). \tag{4.19}$$

The theorem states that the evolution of the excess vorticity is limited by both the square root of the wall-generated palinstrophy and the usual rms vorticity gradient (square root of the palinstrophy), weighed by the average enstrophy-carrying wavenumber $\kappa_2(t)$. The $\|\nabla\omega\|_{2,\mathcal{D}}$-contribution is dominant, as it contains information on the palinstrophy throughout the entire domain. However, when strong boundary layers are present near the walls, the former, $\|\nabla\omega\|_{2,\partial\mathcal{D}}$-contribution may also pick-up information.

Proof of the result

Observe the following proof,

Proof of Theorem 4.4.1. Integrating by parts and using the Schwarz inequality in $L_2(\partial\mathcal{D})$, one has

$$\begin{aligned}-\dot{L}(t) &= \nu \int_{\partial\mathcal{D}} r^2 \nabla\omega \cdot \mathbf{n} \mathrm{d}s - 2\nu \int_{\mathcal{D}} \mathbf{r} \cdot \nabla\omega \mathrm{d}A \\ &\leq \frac{\nu\kappa_2(t)}{\lambda_1^{1/2}} \left(\|r^2\|_{2,\partial\mathcal{D}} \|\nabla\omega\|_{2,\partial\mathcal{D}} + 2\|\mathbf{r}\|_{2,\mathcal{D}} \|\nabla\omega\|_{2,\mathcal{D}} \right),\end{aligned}$$

where we used that, by the P-F inequality, one has $1 \leq \kappa_2(t)\lambda_1^{-1/2}$. Also, we now have

$$-\lambda_1^{1/2} \|\mathbf{r}\|_{2,\mathcal{D}}^{-1} \dot{L}(t) \leq \nu\kappa_2(t) \left(\frac{\|r^2\|_{2,\partial\mathcal{D}}}{\|\mathbf{r}\|_{2,\mathcal{D}}} \|\nabla\omega\|_{2,\partial\mathcal{D}} + 2\|\nabla\omega\|_{2,\mathcal{D}} \right). \tag{4.20}$$

Next, we turn to the enstrophy evolution. Because $\partial\mathcal{D}$ is piecewise C^1, we can use the Sobolev trace embedding theorem of Section 1.2.2, one has, for constant $C_0 > 0$, and by the P-F inequality,

$$\begin{aligned}\|\omega\|_{2,\partial\Omega} &\leq C_0 \left(\|\omega\|_{2,\Omega}^2 + \|\nabla\omega\|_{2,\Omega}^2 \right)^{1/2} \\ &\leq C_0 \left(1 + \lambda_1^{-1} \right)^{1/2} \|\nabla\omega\|_{2,\Omega}.\end{aligned}$$

Denoting $C_1 = C_0(\lambda_1^{-1} + 1)^{1/2}$, with these observations

$$\begin{aligned}\dot{Z}(t) &= \nu \int_{\partial\mathcal{D}} \omega \nabla\omega \cdot \mathbf{n} \mathrm{d}s - \nu \|\nabla\omega\|_{2,\mathcal{D}}^2 \\ &\leq \nu \|\omega\|_{2,\partial\mathcal{D}} \|\nabla\omega\|_{2,\partial\mathcal{D}} - \nu \|\nabla\omega\|_{2,\mathcal{D}}^2 \\ &\leq \nu \|\nabla\omega\|_{2,\mathcal{D}} \left(C_1 \|\nabla\omega\|_{2,\partial\mathcal{D}} - \|\nabla\omega\|_{2,\mathcal{D}} \right),\end{aligned}$$

such that, because $\|\omega\|_{2,\mathcal{D}} \equiv \|\nabla\mathbf{u}\|_{2,\mathcal{D}}$ and $\|\nabla\omega\|_{2,\mathcal{D}} \equiv \|\Delta\mathbf{u}\|_{2,\mathcal{D}}$, one obtains

$$\|\dot{\omega}\|_{2,\mathcal{D}} \leq \nu\kappa_2(t) \left(C_1 \|\nabla\omega\|_{2,\partial\mathcal{D}} - \|\nabla\omega\|_{2,\mathcal{D}} \right), \tag{4.21}$$

where we used the enstrophy wavenumber $\kappa(t)$. Now the time derivative of the excess vorticity is

$$\dot{Q}(t) = \|\dot{\omega}\|_{2,\mathcal{D}} - \lambda_1^{1/2} \|\mathbf{r}\|_{2,\mathcal{D}}^{-1} \dot{L}(t),$$

and the theorem follows from inequalities (4.20) and (4.21), with constant

$$C_2 = \left(\|r^2\|_{2,\partial\mathcal{D}} / \|\mathbf{r}\|_{2,\mathcal{D}} \right) + C_1.$$

□

4.5 No-slip versus periodic boundary conditions

Classical scaling on a Poincaré-Friedrichs domain

On an infinite domain Constantin *et al.* [29] showed that the first eigenfunction of the Laplacian operator cannot drive a classical KLB inertial range. The reason is that the forcing and dissipation wavenumbers are not well-separated, $k_\eta \leq \sqrt{3}k_f$. Remarkably, this result was later established for a Markov-chain forcing model by Oetzel and Vallis [100], who observed no separation between the forcing scale and the enstrophy dissipation scale in high-resolution double-periodic simulations.
As noted by Tran and Bowman [142], on a finite domain one can apply the Poincaré-Friedrichs (P-F) inequality, which may also prohibit classical scaling. Let us combine then the method devised by Constantin *et al.* with the P-F inequality, noting that

$$\langle E(t)\rangle = \int_{k_d}^{k_\eta} E(k)\mathrm{d}k \quad \text{and} \quad \langle Z(t)\rangle = \int_{k_d}^{k_\eta} k^2 E(k)\mathrm{d}\kappa, \tag{4.22}$$

where k_η denotes the enstrophy cut-off wavenumber, see Section 1.3, and k_d denotes the smallest wavenumber, related to the domain length. Applying then the KLB-spectrum, where one can observe, for forcing wavenumber k_f, that

$$\epsilon = (c_1/c_0)^{3/2}\eta k_f^{-2}, \tag{4.23}$$

such that one obtains,

$$\begin{aligned} k_d^2\langle E(t)\rangle &\simeq k_d^2 \int_{k_d}^{k_f} c_0\epsilon^{2/3}k^{-5/3}\mathrm{d}k + k_d^2\int_{k_f}^{k_\eta} c_1\eta^{2/3}k^{-3}\mathrm{d}k \\ &\simeq c_1\eta^{2/3}\left[\frac{3}{2}\left(\frac{k_d}{k_f}\right)^{4/3} - \left(\frac{k_d}{k_f}\right)^2 - \frac{1}{2}\left(\frac{k_d}{k_\eta}\right)^2\right] \end{aligned} \tag{4.24}$$

and

$$\begin{aligned} \langle Z(t)\rangle &\simeq \int_{k_d}^{k_f} c_0\epsilon^{2/3}k^{1/3}\mathrm{d}k + \int_{k_f}^{k_\eta} c_1\eta^{2/3}k^{-1}\mathrm{d}k \\ &\simeq c_1\eta^{2/3}\left[\frac{3}{4}\left(1 - \left(\frac{k_d}{k_f}\right)^{4/3}\right) + \ln(k_\eta/k_f)\right]. \end{aligned} \tag{4.25}$$

Combining (4.24) and (4.25) with the P-F inequality, $k_d^2\langle E(t)\rangle \leq \langle Z(t)\rangle$, one finds

$$\frac{9}{4}\left(\frac{k_d}{k_f}\right)^{4/3} - \left(\frac{k_d}{k_f}\right)^2 \leq \frac{3}{4} + \frac{1}{2}\left(\frac{k_d}{k_\eta}\right)^2 + \ln(k_\eta/k_f).$$

Apply next the KLB-assumption that $k_d \ll k_f \ll k_\eta$, then

$$e^{-3/4}k_f \leq k_\eta. \tag{4.26}$$

Not as strong as the result by Constantin *et al.*, but still one sees that k_f and k_η may be not well-separated and one may even have $k_f > k_\eta$, which would mean that no

inertial range exists below the forcing scale. Note that we did not even require no-slip boundaries to achieve this result, the mere fact that a P-F inequality can be applied is sufficient.

Further discussion

Throughout the development of the theory of 2D turbulence flows on a double-periodic domain have served as a reference case. The absence of boundary integrals in the enstrophy balance on a periodic domain provides a control over the enstrophy dissipation χ, which is lacking for no-slip boundary conditions. However, it was observed in our computational results that the no-slip boundaries enhance energy dissipation due to the generation of vorticity in the viscous boundary layers, a mechanism which is absent on a double-periodic domain. This difference was also noted by Clercx *et al.* [26] for computations on a circular no-slip domain as compared to a flow on a double-periodic domain. In fact, while Tran and Bowman [142, 143], in their theory on spectral scaling exponents, assume that the energy reaches a stationary state in computations, such a state has not yet been observed for pure Navier-Stokes flows on a double-periodic domain.
Furthermore, Eyink [39] remarked that a rigorous prove that the energy in the limit $\nu \to 0$ remains finite, $E(t) < \infty$, is still lacking, but intuition suggests this is more likely to be the case on a no-slip domain than on a double-periodic domain. Note that no (quasi) 2D laboratory experiments with infinite kinetic energy have been observed so far. In this context we should also mention a result due to Vishik and Fursikov [148], who proved, for a white-noise in time forcing in a no-slip domain, that

$$\nu\langle\|\nabla\mathbf{u}\|^2_{2,\Omega}\rangle = F_{ii}(0), \tag{4.27}$$

where $F_{ii}(0)$ is the trace of the forcing correlation tensor. While Eyink [40] interpreted this result as a proof of diverging energy in forced turbulence in the limit $\nu \to 0$, for the viscous case it implies, by the P-F inequality, a finite energy.

With respect to phenomenology, forced Navier-Stokes flows on a double-periodic domain invariably seem to lead to a dipolar condensation regime, as observed by Hossain *et al.* [64]. In this sense, the no-slip boundaries have a dramatic effect on the evolution of the flow, as the difference of such a stable dipolar state on a double-periodic domain with the disrupted condensation regime evolution observed in our computations is quite pronounced. Immediately, our results raise questions on the applicability of KLB-theory to the no-slip setting; the interaction of small with large scales of motion during the break-up of a large circulation cell and the generation of enstrophy at the walls are in clear violation of the assumptions of the classical scaling theory. However, our results encompass only modest Reynolds numbers. Increasing the integral scale Reynolds number may lead to a different phenomenology and different conclusions.

Chapter 5

Vorticity statistics

There are three kinds of lies: lies, damned lies, and statistics.
Benjamin Disraeli (1804-1881)

5.1 Introduction

In this Chapter we turn to study certain statistical properties of flows that can be characterized by the disrupted condensation regime phenomenology described in Chapter 4. Our aim is to examine the statistics of the small scales of motion, thus carving away the effects of the self-organization of the flow at the large scales. Furthermore, we examine the influence of the no-slip walls on these small scales of motion and compare the observed scaling behavior of these statistics with that predicted by classical KLB-theory. However, we consider only limited integral-scale Reynolds numbers, such that a comparison may not always be appropriate. Our aim is, again, not to reach higher Reynolds numbers, but rather to examine in more detail the statistics associated with the disrupted condensation regime.

The most important tool used to analyze flow statistics is based on spatial vorticity (or velocity) differences, taken over length scale $r = |\mathbf{r}|$,

$$\delta\omega(\mathbf{r}) = \omega(\mathbf{x}+\mathbf{r}) - \omega(\mathbf{x}).$$

If the vorticity field is Hölder continuous, see Adams [2], it holds that, for $0 < \mu < 1$,

$$|\omega(\mathbf{x}+\mathbf{r}) - \omega(\mathbf{x})| \leq Cr^{\mu} \quad C \in \mathbb{R}^{+},$$

and the absolute differences exhibit a scaling behavior with r.
Raising the differences to the power n followed by ensemble averaging $\langle\cdot\rangle$, yields the n-th order vorticity structure function

$$S_n(\omega(\mathbf{r})) = \langle(\delta\omega(\mathbf{r}))^n\rangle.$$

Because the Eulerian velocity field $\mathbf{u}(t,\mathbf{x})$ lives in $\mathbb{R}^2$, one can take either parallel or perpendicular velocity differences, leading respectively to $S_n^{\parallel}(\mathbf{u}(\mathbf{r}))$ and $S_n^{\perp}(\mathbf{u}(\mathbf{r}))$. As noted by Doering and Gibbon [35], any function in the Lebesgue space L_2 may still have local singularities. In a two-dimensional fluid flow this may be observed in the form of filamentary structures that carry large amounts of vorticity and thus may act as

true discontinuities in the vorticity field. So a theory that deals with the scaling behavior of $S_n(\omega(\mathbf{r}))$ should take into account the possibility of such intermittency effects on the small length scales in the flow. These effects cause deviations from Gaussianity for the smallest length scales, observed in the form of, e.g., asymmetric probability distribution functions of vorticity increments. On the other hand, because the Navier-Stokes equations are invariant with scale, statistical quantities that depend on the separation length r should also possess scaling behavior that is proportional to r.

Multi-fractal scaling

The two issues of scale invariance and intermittency are addressed with the so-called multi-fractal formalism, see e.g. Frisch [53]. The key concept is that instead of a fixed scaling exponent, each scale r may have its specific exponent,

$$\delta\omega(\mathbf{r}) \sim r^h,$$

with probability distribution

$$P_h(\delta\omega) \sim r^{\dim - D(h)}.$$

The scaling exponent has a clear geometrical meaning: $\dim$ refers to the spatial dimension of the problem, which equals 2, whereas $D(h)$ refers to a fractal dimension of the problem. Consequently, by using the difference $2 - D(h)$, one assumes that a lower-dimensional subset of the full two-dimensional flow problem causes the observed vorticity fluctuations. Again, this can be visualized in the form of vorticity filaments that are more one- than two-dimensional entities, whilst carrying a non-negligible amount of vorticity.
The scaling behavior of the vorticity structure functions of order n would be

$$S_n(\omega(\mathbf{r})) \sim r^{\zeta(n)},$$

where it is understood that taking the logarithm on both sides leads, for small r, to exponent

$$\zeta(n) \equiv \inf_{h \geq 0} \{nh + [2 - D(h)]\},$$

and the infimum is taken because only the smallest exponents are of interest. The relation between the vorticity structure function exponents and the classical energy spectrum $E(k)$, at wave number k, is for

$$E(k) \sim k^{\beta},$$

that one has $\beta = -(3 + \zeta(2))$.

A theoretical issue is the possibility of 'dissipative singularities', that cannot be ruled out. Suppose that $\epsilon(\mathbf{r})$ denotes the local energy dissipation concentrated in a ball with radius r. In fact, the classical theory assumes that $\epsilon(\mathbf{r}) \rightarrow 0$ for $\nu \rightarrow 0$, which implies regularity of the velocity field, $\delta\mathbf{u}(\mathbf{r}) \sim r$, and Kraichnan scaling [75] for the vorticity field, $\delta\omega(\mathbf{r}) \sim$ constant, because the velocity and vorticity Hölder exponents are related by $\mu_{\mathbf{u}} = \mu_{\omega} + 1$. However, in the limit $r \rightarrow 0$ a negative Hölder exponent, $\mu < 0$, would lead to singularities. It is the possibility of these 'negative Hölder singularities'

in the vorticity field that has led to some heated debate, see Eyink [41] and Falkovich and Lebedev [43] and also the discussion in Section 4.5.

Structure function scaling results for small scales of motion were obtained in laboratory experiments in a thin, electromagnetically forced fluid layer by Paret *et al.* [106] and in soap film experiments by Kellay *et al.* [68], see also the overview by Kellay and Goldburg [69], and Rivera *et al.* [113], who compared the result obtained with structure functions to the results obtained with a filtering technique based on large-eddy simulations. Several numerical experiments were devoted to the topic, of which we mention the studies by Babiano *et al.* [7], whose work was based on velocity rather than vorticity increments and Chen *et al.* [23], who used large-eddy filtering techniques to examine the alignment of the vorticity gradient and the vorticity transport vector. Similar alignment issues were explored earlier by Protas *et al.* [110].

Chapter outline

In Section 5.2 we analyze the scaling behavior of vorticity structure functions in the interior of the domain, assuming our measurements are taken sufficiently far from the boundary to reduce the influence of the no-slip boundaries to a minimum. In Section 5.3 scaling results in the near-wall region are compared to those for the interior. Section 5.4 contains results on the local enstrophy transfer, which is coupled to the third-order mixed structure function.

5.2 Statistics in the interior of the domain

For separation lengths r, lying between the forcing scale and the viscous dissipation scale, $\ell_f > r > \ell_\chi$, assuming only a constant ultraviolet flux of enstrophy and using the language of the multi-fractal model, Eyink [39] proved the scaling

$$S_n(\omega(\mathbf{r})) \sim r^{\zeta(n)}, \quad \zeta(n) \leq 2/3, \quad \forall n,$$

for the n^{th}-order vorticity structure function, where $\zeta(n)$ is the usual multi-fractal scaling exponent. This result confirms the theoretical work of Sulem and Frisch [131], who concluded that in the enstrophy range the energy spectrum should scale as $E(k) \leq c_0 k^\beta$, with the lower bound $\beta > -4$.

On the contrary, using the classical Batchelor argument for the advection of a passive scalar, Falkovich and Lebedev [42] argued that one must have $\zeta(n) = 0$ for all n. Instead, these authors assumed a logarithmic scaling regime for all vorticity structure functions,

$$S_n(\omega(\mathbf{r})) \sim (\ln(r))^{2n/3}.$$

This, in turn, suggests that logarithmic intermittency corrections on spectral scaling in the enstrophy cascade range, are perhaps superfluous. The Falkovich-Lebedev result was confirmed in an experimental setting in the aforementioned laboratory experiments on a quasi-2D flow in a square PVC cell by Paret *et al.* [106], who assumed the flow to be dominantly isotropic. These authors observed no significant deviations from Gaussian values, estimated the direct cascade KLB-constant to be $c_1 \simeq 1.4 \pm 0.3$ and concluded that classical KLB-theory, perhaps even without later logarithmic corrections,

is probably fully sufficient in explaining direct cascade dynamics. Remarkably, high resolution (2048^2 modes) DNS by Ishihara and Kaneda [65] of forced turbulence on a double periodic domain, using hyperviscosity, where the dissipation operator equalled $\nu\Delta^p$ for $p = 6$, also obeyed the classical picture, with logarithmic corrections and constant $c_1 = 1.9$. On the other hand, Tran and Bowman [142] argued that on any finite domain one should have a spectral exponent in the direct cascade range of $\beta < -5$, which would imply that $\zeta(2) > 2$. However, strictly speaking the relations used in their argument are only valid for a double-periodic domain, making the predictions less universal than indicated.

Before comparing our computational results with the ideas mentioned above, we briefly outline some of the usual statistical tools used in the data analysis.

Statistical tools and computational results

Several quantities should be measured to obtain an idea of the statistical properties of the small scales. The basic quantity is the probability density function (PDF) $P(s'(\mathbf{r}))$ of normalized vorticity increments,

$$s'(\mathbf{r}) = \frac{\delta\omega(\mathbf{r})}{\langle(\delta\omega(\mathbf{r}))^2\rangle^{1/2}},$$

where the denominator represents the root-mean-square over time.
Furthermore, the skewness and flatness represent the third and fourth statistical moments of a distribution and are defined for the vorticity increments as, respectively,

$$S(\mathbf{r}) := \frac{S_3(\omega(\mathbf{r}))}{(S_2(\omega(\mathbf{r})))^{3/2}}$$

and

$$F(\mathbf{r}) := \frac{S_4(\omega(\mathbf{r}))}{(S_2(\omega(\mathbf{r})))^2}.$$

This latter measure can also be expanded to include higher orders, known as the so-called hyperflatness factors, which are defined as

$$H_{2n}(\mathbf{r}) := \frac{S_{2n}(\omega(\mathbf{r}))}{(S_2(\omega(\mathbf{r})))^n} \quad \text{for} \quad n = 2, 3, \ldots.$$

If $H_{2n}(\mathbf{r})$ is independent of separation length r, no intermittency is present, which, by the multi-fractal scaling model, results in scaling exponents $\zeta(2n) = n\zeta(2)$, or, $\zeta(n) \propto n$. However, it was argued by Dubos *et al.* that while the hyperflatness may deviate from its expected value $E(H_{2n}(\phi))$ for a Gaussian random process ϕ,

$$E\left(H_{2n}(\phi)\right) = \frac{(2n)!}{2^n n!},$$

such deviations do not prove the presence of intermittency in the classical sense.
Another important issue is to check for statistical convergence of the data, for which Tabeling *et al.* [135], see also Belin *et al.* [11], applied a convenient method. Based on the fact that the flatness, $F(\mathbf{r})$, can also be expressed as

$$F(\mathbf{r}) = \int_0^\infty (s'(\mathbf{r}))^4 P'(s'(\mathbf{r}))\mathrm{d}s' = \frac{\int_0^\infty (s(\mathbf{r}))^4 P(s,\mathbf{r})\mathrm{d}s}{\left(\int_0^\infty (s(\mathbf{r}))^2 P(s,\mathbf{r})\mathrm{d}s\right)^2},$$

ν	ℓ_f	A_0	$\tilde{a}$	Δt	N
2.0×10^{-4}	0.29	5.0	0.01	1.35×10^{-4}	257

Table 5.1: *Computational parameters; kinematic viscosity, forcing length, forcing amplitude, initial noise amplitude, computational time step and computational resolution.*

Re_*	ℓ_{en}	ℓ_χ	Re_χ
7500	0.63	0.0045	4150

Table 5.2: *Measured quantities; integral-scale Reynolds number, mean-square wavenumber, enstrophy dissipation length and alternate Reynolds number.*

where we temporarily denoted vorticity differences as $s(\mathbf{r}) = \delta\omega(\mathbf{r})$ and where $P(s, \mathbf{r})$ is the PDF of these vorticity increments. As remarked by Tabeling *et al.*, it is the quantity

$$(s(\mathbf{r}))^p \, P(s, \mathbf{r}), \tag{5.1}$$

for orders $p = 4, 6, \ldots$, that allows one to check the statistical convergence of the data, by simply plotting that quantity and verifying if the tails of the distribution are well-defined. In fact, for their experiments on three-dimensional turbulence in a low-temperature helium gas Belin *et al.* plotted a relation between the order of the structure function and the minimum number of data points required to obtain converged statistics. From this relation these authors concluded that sixth order structure functions required a record length of up to $\mathcal{O}\left(10^5\right)$ points, whereas eighth-order structure functions required a number of points on the order $\mathcal{O}\left(5 \times 10^7\right)$. On the other hand, Paret *et al.* [106] could determine vorticity structure functions, in experiments on quasi-2D turbulence in electromagnetically forced thin fluid layers, up to order $n = 12$, using a mere 10^5 data points, because the PDF of vorticity increments were sufficiently close to a Gaussian PDF.

Let us move on to discuss our computational results, starting with a summary of the numerical parameters in Table 5.1 and several measured quantities in Table 5.2. Note that, with $k_f = 7$, the forcing length-scale equals approximately $\ell_f \sim 0.29$. From the time-averaged kinetic energy it follows that the integral-scale Reynolds number was close to $Re_* \simeq 7500$. As mentioned before in Section 4.4, the square root of the ratio of enstrophy and energy defines a characteristic mean-square wavenumber, $\kappa_1(t) = (Z(t)/E(t))^{1/2}$, from which one obtains a mean energy carrying wavelength, $\ell_{en} = 2\pi\langle\kappa_1\rangle^{-1}$. Averaged over time, the characteristic energy length in our computational results is slightly larger than twice the forcing length. During the computations the palinstrophy was at most on the order of $P(t) = \mathcal{O}\left(10^7\right)$, thus satisfying the heuristic demand for the computational resolution, equation (2.7). Furthermore, the dissipative length-scale for the enstrophy, ℓ_χ, was determined to be less than the smallest separation length over which vorticity differences were measured in the interior $r = 0.006$. Hence, a modest enstrophy cascade inertial range $\ell_f > r > \ell_\chi$ is achieved of close to two decades. In this respect, for laboratory experiments in electromagnetically forced shallow fluid layers Paret *et al.* [106] defined a Reynolds number as the

squared ratio of forcing and enstrophy dissipation lengths,

$$Re_\chi := \left(\frac{\ell_f}{\ell_\chi}\right)^2,$$

achieving a value on the order of $Re_\chi = \mathcal{O}\left(10^3\right)$. Here, the same definition yields $Re_\chi = 4.2 \times 10^3$.

In view of the discussion above, it is important to first consider the issue of convergence of statistics, using the method introduced by Belin *et al.* [11] and noting that our record lengths are on the order of $\mathcal{O}\left(10^6\right)$ points. Arguably, it is easier to obtain records of sufficient length in most laboratory experiments than in numerical simulations, where, for high Reynolds numbers, only relatively few eddy turn-over times are computed. In Figure 5.1 the quantity (5.1) is shown, for $p = 4, 6, 8$ and 10, measured at the separation length $r = 0.006$. With increasing order the tails become less well-defined and the shape becomes less symmetric. Clearly, the statistics for $p = 8$ and 10 are not converged, whereas the situation for $p = 6$ is still reasonably acceptable. The consequence is, hence, that we cannot consider structure functions or the hyperflatness of orders greater than 6, with any confidence. Indeed, this is a severe limitation with respect to issues of intermittency, where it is desirable to have information on higher order statistics and those aspects should definitely be addressed in future work.

We plot vorticity structure functions of orders 2, 4 and 6 against separation length in a double logarithmic graph in Figure 5.2(a). The measurements of vorticity increments are taken in the center of the domain, throughout a small square $B(r)$ of side r. In such a manner one hopes to reduce the influence of the boundaries and achieve a more or less isotropic situation. It was argued by Paret *et al.* [106] that experiments in a quasi 2D flow in a square cell, yielded isotropic results for the vorticity statistics, after sufficient record lengths were averaged.

The solid line in the graph corresponds to $\zeta(n) = 2/3$, the upper bound on the scaling exponents of vorticity structure functions of all orders provided by Eyink [39]. Clearly, scaling for $\zeta(2)$ is steeper than 2/3, but not as steep as the value $\zeta(2) > 2$, predicted by Tran and Bowman [142]. An explanation for the deviations from both the Eyink-model and the Tran and Bowman prediction may lie in the non-constant enstrophy flux on a bounded domain, an observation we return to in Section 5.4. We sum up the results for the scaling exponents in Table 5.3. The values for $n = 2$ and $n = 4$ are significantly different from the values obtained from laboratory experiments by Paret *et al.* [106], who observed scaling exponents ranging from $\zeta = -0.05$ to $\zeta = 0.15$. Furthermore, these results point at a steeper than $\beta = -3$ scaling of the energy spectrum in the direct cascade range. On the other hand, Paret *et al.* noted that the enstrophy dissipation in their experiments may not be entirely two-dimensional, which could have profound consequences with respect to the observed scaling behavior at small scales.

Figure 5.2(b) shows the flatness and hyperflatness of order $n = 3$, corresponding to the data in Figure 5.2(a). The corresponding Gaussian values are 3 and 15 for the flatness and third order hyperflatness, respectively, from which the computational data deviate strongly moving towards smaller scales. However, both the results for the (hyper) flatness and the scaling exponents may be different for higher Reynolds numbers, where a different phenomenology may be found to occur.

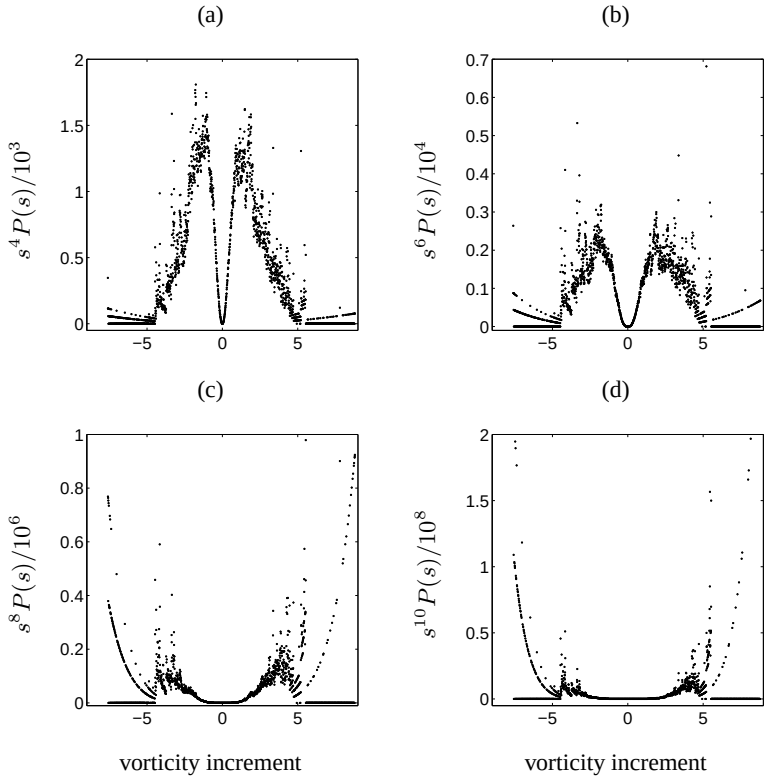

Figure 5.1: *Convergence check for the vorticity statistics (structure functions), showing the scaled quantity (5.1), for order p=4 (a), p=6 (b), p=8 (c) and p=10 (d).*

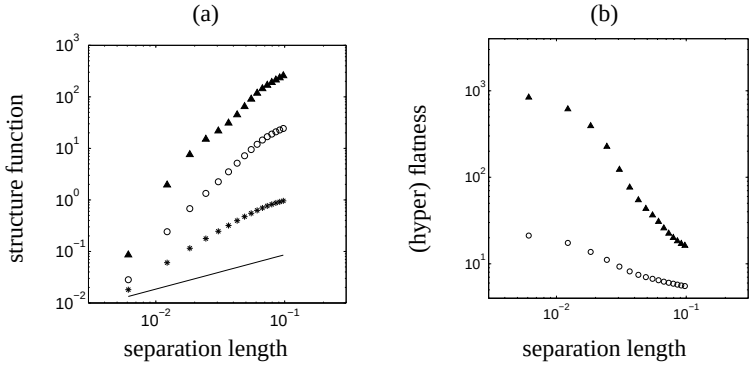

Figure 5.2: *Double logarithmic plot of normalized vorticity structure functions (a), of order n=2 (stars), n=4 (circles) and n=6 (triangles) versus separation length $|\mathbf{r}|$, where the solid line corresponds to $\zeta(n) = 2/3$. Double logarithmic plot of flatness (circles) and hyperflatness of order $n = 3$ (filled triangles) against separation length (b).*

n	2	4	6
$\zeta(n)$	1.3 ± 0.1	2.2 ± 0.1	2.7 ± 0.2

Table 5.3: *Scaling exponents for the structure functions of order n.*

One-dimensional Chebyshev spectra

To complement our observations on scaling behavior, one-dimensional power spectra are examined, showing the distribution of energy and enstrophy over the computational modes. Because the usual Fourier methods are not applicable on a no-slip domain, we have to use one-dimensional Chebyshev spectra instead. These spectra are measured along a line in the domain, following the procedure outlined by Clercx and van Heijst [27]. Evaluating the local kinetic energy in terms of its Chebyshev coefficients $\tilde{E}_{mn}(t)$,

$$E(t, \mathbf{x}) = \sum_{m=0}^{N} \sum_{n=0}^{N} \tilde{E}_{mn}(t) T_n(x) T_m(y),$$

where N is the number of Chebyshev polynomials, which is equal for each direction, and $T_n(x)$ is the n-th order Chebyshev polynomial, see Subsection 2.1.1. Averaging the symmetrically equal contributions along the lines $x = 0$ and $y = 0$, one obtains the one-dimensional (1D) spectrum,

$$\tilde{S}_n(t) = \tfrac{1}{2} \left| \sum_{m=0}^{N} \left(\tilde{E}_{nm}(t) + \tilde{E}_{mn}(t) \right) T_m(0) \right|,$$

a positive quantity. However, it must be cautioned that the correspondence to a Fourier spectrum is not a one-to-one relation and that the Chebyshev spectra should not be compared directly to the KLB-spectrum and its predictions for spectral scaling. Even so, it is interesting to examine the scaling behavior of the Chebyshev spectra, shown below in Figure 5.3. Two 1D spectra at the same instant in time are shown, evaluated on lines through the center of the domain $x = 0$ and $y = 0$. In each spectrum we show, for comparison, the classical KLB-scaling with exponent $\beta = -3$.
While the 1D spectrum on the line $x = 0$ has a fairly uniform scaling in the region below the injection scale, $\ell_f \simeq 0.3$ or mode number 12, the scaling exponent equals $\beta = -2.5 \pm 0.2$. The anisotropy of the flow becomes clear if one considers the corresponding 1D spectrum measured at $y = 0$, where two scaling regions can be identified. One region extends from the forcing scale to mode number 100, where the exponent equals $\beta = -2 \pm 0.1$, for larger modes (smaller scales) the exponent is as low as $\beta = -5 \pm 0.2$. Again, care should be taken in the comparison of these scaling exponents to the theory developed for the double-periodic case, not to mention the case of an infinite domain. Even so, the results are surprising as *a priori* one might expect steeper spectra, as was conjectured by Tran and Bowman [144] for domains where the P-F inequality can be applied.

Time-averaged 1D spectra are shown in Figure 5.4, for $x = 0.0$ and $y = 0.0$. These spectra were averaged over roughly $45T_e$, where T_e denotes the large-scale eddy turnover

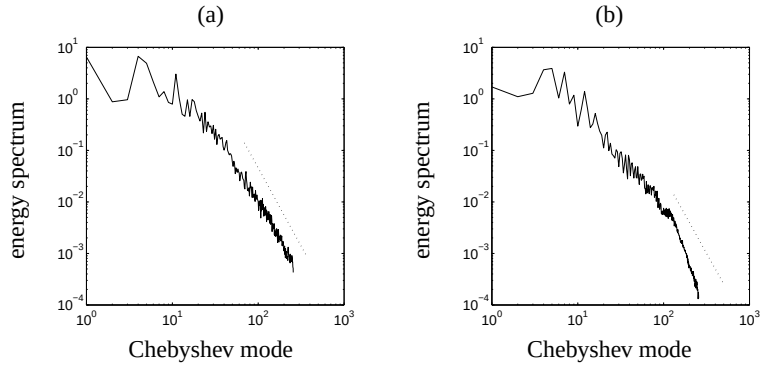

Figure 5.3: *Double logarithmic plot of the spectral energy per Chebyshev mode on lines through the center of the domain, $x = 0$ (a) and $y = 0$ (b). The dotted line in each graph shows the classical scaling with exponent $\beta = -3$. In both plots the forcing injection scale is at mode 12 and time equals $t = 200$.*

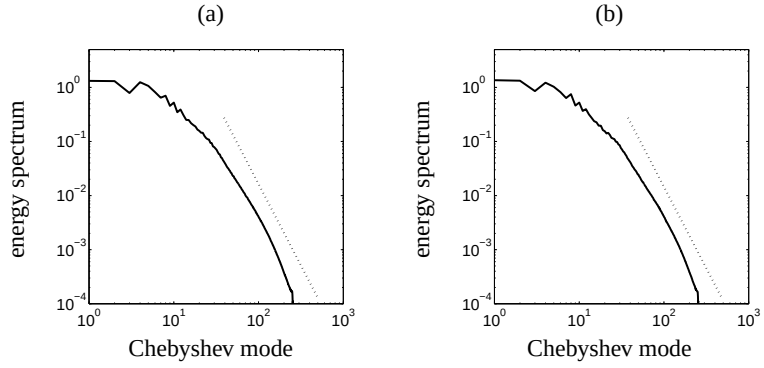

Figure 5.4: *Double logarithmic plot of the spectral energy per Chebyshev mode on lines through the center of the domain, $x = 0$ (a) and $y = 0$ (b), averaged over roughly 45 large-scale eddy turnover times. The dotted line in each graph shows the classical scaling with exponent $\beta = -3$. In both plots the forcing injection scale is situated at mode 12.*

time, introduced in the previous Chapter. In these averaged spectra the anisotropy effect has largely been levelled out. For both directions two scaling regions can be identified. Extending upwards from the region of the forcing scale to, roughly, mode number 150, the exponent is surprisingly close to the classical predictions, with $\beta = -3 \pm 0.1$. However, for the higher modes the spectrum scales like $\beta = -4$.
The scaling exponent over the middle range of modi is somewhat larger than the exponent derived from the second order vorticity structure function, $\zeta(2)$, but for the high mode numbers the scaling would be in much closer correspondence, as $\zeta(2) = 1.3 \pm 0.1$, which would lead to $\beta = -4.3 \pm 0.1$. It is thought that the advection of viscous boundary layers into the interior of the domain leads to the altered scaling for the high Chebyshev modes, an observation we return to in the next Section.
A remaining problem is that the lack of isotropy on a no-slip domain makes the coupling between exponents $\zeta(2)$ and β less obvious. Furthermore, the unclear relation between the 1D Chebyshev spectrum and the usual Fourier spectrum mentioned above should be kept in mind.

5.3 Statistics in the wall-region

In the previous Sections we deliberately took measurements at some distance from the domain boundary $\partial\mathcal{D}$, to avoid obvious bias expected to occur near the wall. Now we turn to examine statistics measured near the domain boundary, measured in the wall-normal direction, and compare these to the scaling results reported in the previous Section. For three-dimensional turbulence Benzi *et al.* [12] compared small-scale velocity statistics measured near a no-slip wall with statistics measured in the bulk of the flow, concluding there was an increase in deviations from Gaussian behavior moving towards the wall.

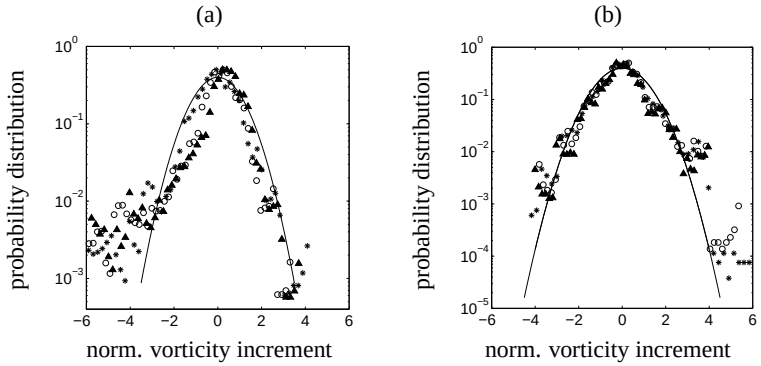

Figure 5.5: *Log-linear plot of the PDF, $P(s')$, of normalized vorticity increments, $s'(\mathbf{r})$, with $r = 0.006$ (stars), $r = 0.012$ (circles) and $r = 0.024$ (filled triangles), where the solid line represents a Gaussian normal PDF, near the wall (a) and in the interior of the domain (b). Measurements in (a) were taken in the wall-normal direction.*

In Figure 5.5(a) we show the PDF of normalized vorticity increments in the wall-region at three separation lengths and the corresponding PDF in the interior in Figure 5.5(b). Clearly, deviations from the normal distribution, shown in the Figure as solid lines, are

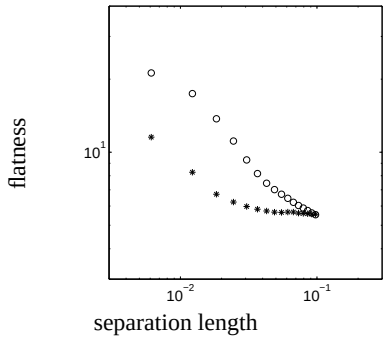

Figure 5.6: *Double logarithmic plot of flatness for wall region (stars) and interior (circles) versus separation length* r.

very pronounced in the near-wall region, although smaller deviations also occur in the interior for separation lengths $r = 0.006$ and $r = 0.012$. In the wall region the deviations are still marked for $r = 0.024$, but this is not the case in the interior. In the work of Benzi *et al.* increasing deviations from a Gaussian distribution were interpreted as an increase in intermittency, moving from the interior of the flow towards the wall.

Surprisingly, from Figure 5.6 the increase of the flatness towards smaller separation lengths $|\mathbf{r}|$ seems to be greater for the interior than for the wall region. This result indicates that, considering deviations from Gaussian behavior, there may be no clear difference between the wall region and the interior of the flow. From a phenomenological viewpoint the latter conclusion fits with the idea that boundary layers and vorticity filaments are advected into the interior of the domain when a large circulation cell breaks up, that is, if one accepts that it is these elongated structures that are responsible for the deviations from Gaussian behavior.

An important quantity is the average boundary layer thickness δ_{bl}, defined here as

$$\delta_{bl} := \left(\frac{\int_{\partial\mathcal{D}} \left(\partial_n \mathbf{u}_{\parallel}\right)^2 \mathrm{d}s}{\int_{\partial\mathcal{D}} \left(\partial_n \omega\right)^2 \mathrm{d}s} \right)^{1/2},$$

where $\mathbf{u}_{\parallel}$ denotes the velocity component parallel to the boundary, $\mathbf{u} \parallel \partial\mathcal{D}$ and ∂_n denotes the derivative normal to $\partial\mathcal{D}$, see Maassen [85]. On the square no-slip domain one has $\partial_n \mathbf{u}_{\parallel}(\partial\mathcal{D}) = \omega(\partial\mathcal{D})$. In other words, the average boundary layer thickness is defined as the ratio of the magnitude of the stress to the vorticity gradient at the boundary. Averaged over 45 large-scale eddy turnover times in the statistically stationary regime, the boundary layer thickness equals $\langle \delta_{bl} \rangle = 0.0062$, a value corresponding to the initial boundary layer thickness in simulations of decaying flows on a square no-slip domain by Clercx and van Heijst [27].

One-dimensional Chebyshev spectra

We examine one-dimensional Chebyshev spectra, shown Figure 5.7. These spectra are measured at $t = 200$ in the near-wall region on the lines $x = 0.99$ and $y = 0.99$, see the previous Section for an explanation. Measured on the line $x = 0.99$, Figure 5.7(a), the spectrum displays an extended scaling region with exponent $\beta = -2.5 \pm 0.1$. For $y = 0.99$, Figure 5.7(b), the scaling in the highest modes is as $\beta = -2.9 \pm 0.1$, but

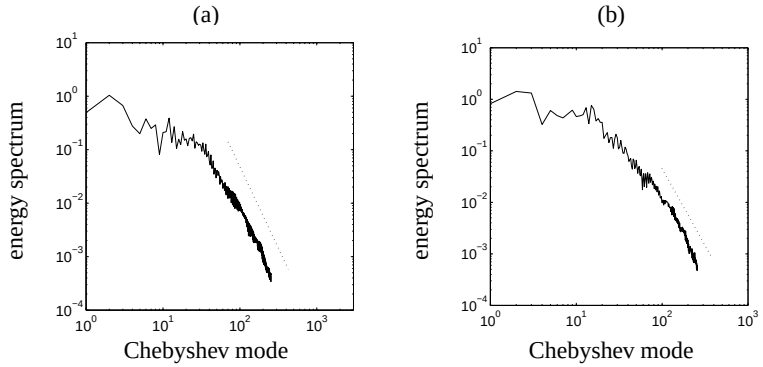

Figure 5.7: *Double logarithmic plot of the spectral energy per Chebyshev mode on lines near the wall, $x = 0.99$ (a) and $y = 0.99$ (b). The dotted line in each graph shows the classical scaling with exponent $\beta = -3$. In both plots the forcing injection scale is situated at mode 12.*

moving from the high modes to the forcing mode the scaling behavior flattens out, such that the region of mode numbers < 50 has exponent $\beta = -2 \pm 0.2$.

Clercx and van Heijst [27] performed simulations of decaying turbulence on a square no-slip domain at integral-scale Reynolds numbers $Re = 5000$, $Re = 10000$ and $Re = 20000$, where the initial condition corresponded to an array of 100 Gaussian vortices of alternating sign. For the scaling exponents of the instantaneous Chebyshev spectrum measured at an early time near the wall, it was observed that the scaling exponent of the highest Chebyshev modes relaxed from $\beta = -2.4$ to $\beta = -5/3$, moving from $Re = 5000$ to $Re = 20000$. It was argued by these authors that the boundary layers, acting as a source of small-scale vorticity, cause the spectrum for the higher Chebyshev modes to become less than the *a priori* expected $\beta = -3$.
In our forced simulations, the $\beta = -5/3$ scaling is not observed for the instantaneous Chebyshev spectra measured in the near-wall region. Due to the lower Reynolds numbers achieved here, the scaling exponent seems closer to that found at $Re = 5000$ in the decaying simulations. On the other hand, in the computations on decaying flows in $\mathcal{D}$, for $Re = 20000$, the spectral scaling of high Chebyshev modes was observed to evolve in time from $\beta = -5/3$ to $\beta = -3$, [27], an observation that was coupled to the simultaneously increasing thickness of the boundary layer.
For the time-averaged spectra in Figure 5.8, averaged over roughly $45T_e$, a scaling region with $\beta \simeq -3$ seems to extend over an even larger range of Chebyshev modi than for the averaged 1D spectra measured in the interior of the domain at $x = 0$ and $y = 0$, shown in Figure 5.4. Extending from modes 20 to 180, a -3 scaling region is recovered, while the higher modes clearly have a steeper scaling behavior, which is closer to $\beta = -5$. In the near-wall region it is thought that the viscous boundary layers influence the spectral scaling behavior over a range of modi, extending beyond the mode numbers associated to the average boundary layer thickness, which is found around mode number 246. Correspondingly, the steeper scaling exponent measured for the high mode numbers in the previous Section was thought to be caused by the influence of vorticity filaments (advected boundary layers).
However, it must be noted that while scaling exponents may (or may not) deviate from classical predictions, the presence of a direct cascade of enstrophy cannot be derived

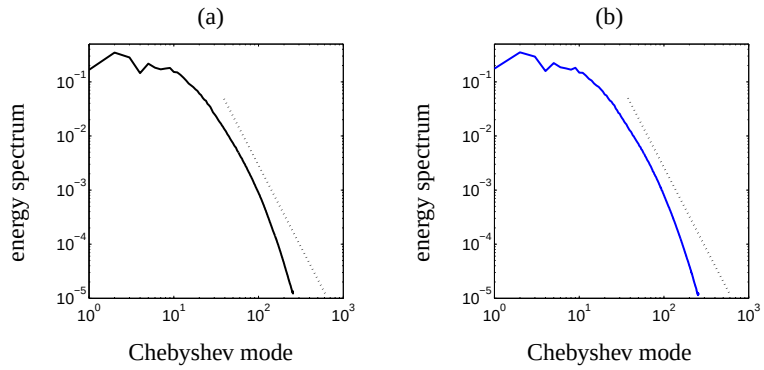

Figure 5.8: *Double logarithmic plot of the spectral energy per Chebyshev mode on lines near the wall, $x = 0.99$ (a) and $y = 0.99$ (b), averaged over roughly 45 large-scale eddy turnover times. The dotted line in each graph shows the classical scaling with exponent $\beta = -3$. In both plots the forcing injection scale is situated at mode 12, the averaged boundary layer thickness is at mode 246.*

from the scaling exponents alone. To obtain this information the enstrophy transfer should be measured, which, again, creates some problems for a no-slip domain.

5.4 A note on the enstrophy

Before considering the enstrophy transfer, let us briefly re-examine, on a general bounded domain Ω with sufficiently smooth boundary $\partial\Omega$, the domain integrated enstrophy balance (1.15). For convenience, we assume a time-independent inhomogeneous term $q(\mathbf{x})$,

$$\dot{Z}(t) + \nu\|\nabla\omega\|_{2,\Omega}^2 = \nu \int_{\partial\Omega} \omega\partial_{\mathbf{n}}\omega \mathrm{d}s + (\omega, q).$$

The analysis gives us some feeling for the enstrophy dissipation process and highlights one of the difficulties in establishing properly the enstrophy transfer. The procedure is very similar to that followed in the proof of theorem 4.4.1, requiring again the trace theorem. First we obtain, by the Hölder inequality,

$$\int_{\partial\Omega} \omega\partial_{\mathbf{n}}\omega \mathrm{d}s \leq \|\omega\|_{2,\partial\Omega}\|\nabla\omega\|_{2,\partial\Omega}.$$

Now relating the norms on $\partial\Omega$ to those over Ω by the trace theorem and rewriting the result with the P-F inequality, one obtains

$$\|\omega\|_{2,\partial\mathcal{D}} \leq C_0\|\omega\|_{1,2,\mathcal{D}} \leq C_0\left(1+\lambda_1^{-1}\right)^{1/2}\|\nabla\omega\|_{2,\mathcal{D}},$$

see also Section 4.4. Furthermore, one can rewrite the innerproduct term by applying, respectively, the Schwarz, Young and P-F inequalities,

$$(q,\omega) \leq \|q\|_{2,\Omega}\|\omega\|_{2,\Omega} \leq \frac{\|q\|_{2,\Omega}^2}{2\nu\lambda_1} + \frac{\nu\lambda_1}{2}\|\omega\|_{2,\Omega}^2 \leq \frac{\|q\|_{2,\Omega}^2}{2\nu\lambda_1} + \frac{\nu}{2}\|\nabla\omega\|_{2,\Omega}^2.$$

Finally, combining these results yields

$$\dot{Z}(t) + \frac{\nu}{2}\|\nabla\omega\|_{2,\Omega}^2 \leq C_1\nu\|\nabla\omega\|_{2,\Omega}\|\nabla\omega\|_{2,\partial\Omega} + \frac{\|q\|_{2,\Omega}^2}{2\nu\lambda_1},$$

where $C_1 = C_0(1+\lambda_1^{-1})^{1/2}$. Taking asymptotic averages, we end up with an expression for the enstrophy dissipation which is different from the usual result on a double-periodic domain, although its asymptotic upper bound remains unaltered,

$$\limsup_{t\to\infty}\frac{\nu}{t}\int_0^t \|\nabla\omega\|_{2,\Omega}\left(\|\nabla\omega\|_{2,\Omega} - C_1\|\nabla\omega\|_{2,\partial\Omega}\right)\mathrm{d}\tau \leq \frac{\|q\|_{2,\Omega}^2}{2\nu\lambda_1}.$$

The first term on the left-hand side equals the usual expression $\chi \equiv \nu\langle\|\nabla\omega\|_{2,\Omega}\rangle$, see Section 1.3, but the second term follows from the presence of no-slip boundaries. So it is the difference of the rms vorticity gradient over the whole domain with the rms vorticity gradient over the boundary that determines the enstrophy dissipation, rather than the usual palinstrophy (mean-square vorticity gradient). These considerations could explain why the Tran and Bowman theory for a double-periodic domain [142] may not be applicable to the no-slip situation. One of the key equations used in their work is essentially the energy balance minus the enstrophy balance,

$$k_f^2\dot{E}(t) - \dot{Z}(t) = 2\nu\left(P(t) - k_f^2 Z(t)\right),$$

where k_f is a forcing wavenumber. On a no-slip domain the right hand side would include the norm $\|\nabla\omega\|_{2,\partial\Omega}$ and there is no *a priori* reason to assume that this quantity tends to vanish under the limit of large times $t\to\infty$. Hence, a directly controlled upper bound on χ is lacking. An interesting situation occurs if

$$C_1\|\nabla\omega\|_{2,\partial\Omega} \to \|\nabla\omega\|_{2,\Omega},$$

which refers to a setting where (nearly) all the enstrophy dissipation is concentrated in the viscous boundary layers and which could lead to considerable deviations from the classical scaling exponents for the vorticity statistics.

Enstrophy transfer

From the vorticity equation one can derive, in the isotropic case, an exact equation for stationary two-point vorticity correlations, see Bernard [13],

$$-\tfrac{1}{2}\nabla\langle[\delta_\parallel\mathbf{u}(\mathbf{r})][\delta\omega(\mathbf{r})]^2\rangle + 2\nu\langle\nabla\omega(\mathbf{r}+\mathbf{x})\nabla\omega(\mathbf{x})\rangle = G(\mathbf{x}),$$

where $G(\mathbf{x})$ denotes the forcing correlation term and the brackets $\langle\cdot\rangle$ denote combined space and time averaging. Taking first the inviscid limit and then the limit of small correlation lengths, one is stuck with a mixed correlation function, in analogy with the Kolmogorov scaling for the third-order velocity structure function in three dimensional flows. Hence the global scaling law (see Bernard [13], Eyink [39] or Tabeling [133]), for the scale dependent enstrophy dissipation, $\chi(\mathbf{r})$, reads as

$$\frac{-1}{2r}\langle Q(\mathbf{r})\rangle = \chi(\mathbf{r}), \tag{5.2}$$

where we denoted the quantity

$$Q(\mathbf{r}) = [\delta_{\|}\mathbf{u}(\mathbf{r})][\delta\omega(\mathbf{r})]^2.$$

By the global law (5.2) the average of this latter quantity should equal the scale dependent enstrophy dissipation, $\chi(\mathbf{r})$. Because the situation is statistically stationary, the transfer should equal dissipation. However, it must be stressed that it is uncertain whether the scaling law (5.2) even holds in the case of a no-slip domain. Relating the quantity $\chi(\mathbf{r})$ to the enstrophy transfer may thus not be appropriate, because in the derivation of equation (5.2) one assumes, respectively, that the situation is isotropic, that one has a constant enstrophy transfer and that one operates in the limit of large Reynolds numbers. As argued before, see also Section 1.3, we meet neither of these requirements, as was pointed out in the discussion on the domain integrated enstrophy balance, above. On the other hand, it is not possible to determine the enstrophy transfer directly from Chebyshev mode triad interactions, as is the case for spectral computations based on Fourier modes on a double-periodic domain. As such, computing the mixed third-order structure function may be the only alternative on a no-slip domain.

The left hand side of equation (5.2), normalized by its maximum value, is shown as a function of r in Figure 5.9, where we took our measurements in a small square centered in the domain. Although the integral of the quantity $-\frac{1}{2}r^{-1}\langle Q(\mathbf{r})\rangle$ is negative, as one expects for the range of scales below the forcing length, one clearly sees an alternating behavior with positive values occurring at several length scales. Interpreting the Figure in terms of enstrophy transfer, there is a predominant flux towards smaller scales in the range $0.1 \geq r \geq 0.006$. Moreover, the shape of the transfer function is rather different from the typical time averaged enstrophy transfer per wavenumber on a double-periodic domain, as determined directly from wavenumber triad interactions, see e.g. Maltrud and Vallis [88], but again, our interpretation is disputable.
Coupling these results to the observed Chebyshev spectra is not straightforward, but roughly one could state that it is the production of vorticity in the near-wall region that causes both the 1D Chebyshev spectra and the quantity $Q(\mathbf{r})$ to deviate from observations on a double-periodic domain. However, we mention, again, that the integral-scale Reynolds numbers considered here are rather modest and different results may be obtained if the number Re_* is increased significantly.

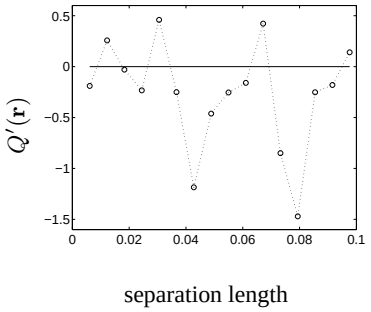

Figure 5.9: *The normalized mixed third-order structure function* $Q'(\mathbf{r}) = -\frac{1}{2}r^{-1}\langle Q(\mathbf{r})\rangle/Q_{max}(\mathbf{r})$*, as a function of separation length* $|\mathbf{r}|$.

In turbulent soap film experiments Kellay *et al.* [68] measured the PDF of the quantity $Q(\mathbf{r})$, denoted as $P(Q(\mathbf{r}))$, and compared this PDF to an exponential fit. Results were

highly non-Gaussian, and the form of the exponential fit was accordingly

$$\exp^{-(|Q(\mathbf{r})|/Q_0)^\alpha}$$

where the value of the exponent was determined at $\alpha = 0.4$. Numerical computations on a double-periodic domain with high Reynolds numbers, $Re = \mathcal{O}\left(5 \times 10^5\right)$, lead to a similar value for the exponent, with $\alpha = 0.41$. Furthermore, the exponent did not vary significantly with scale. In Figure 5.10(a) we show the PDF $P(Q(\mathbf{r}))$ for three separation lengths. Indeed, the PDF has a highly non-Gaussian form and the exponential fit with $\alpha = 0.4$ and $Q_0 = 0.04$ is reasonable for increasing separation lengths, Figures 5.10(b), (c) and (d).
Thus our computational results are in accordance with the earlier experimental and numerical work of Kellay *et al.* [68], even though the Reynolds numbers considered here are much lower. For forced and hyper-viscous 2D turbulence on a double periodic domain Chen *et al.* [23] found symmetric PDFs of the enstrophy transfer for a range of length scales. However, these authors calculated the enstrophy transfer with a large eddy simulation filtering technique, rather than based on the third order mixed structure function. The advantage of such a method is that it allows a calculation of the enstrophy flux at each point in the domain, rather than having to average over space. Increasing tails of the measured PDFs for smaller scales was interpreted as a sign of increasing intermittency, an observation that, more or less, carries over to the results presented here.
Recall from Section 1.1 that the physical mechanism behind the direct cascade of enstrophy, if it exists, was posed by Batchelor [10] to be an amplification of vorticity gradients due to shearing of small scale filaments by the large scale flow field. Based on new ideas in 3D turbulence, Chen *et al.* [23] examined the local alignment of the vorticity gradient $\nabla\omega(t, \mathbf{x})$ and the vorticity transport vector. These authors concluded that vorticity is mainly transported along streamlines and much less so along the direction of the gradient $\nabla\omega(t, \mathbf{x})$, confirming Batchelor's ideas.

Instead of the local enstrophy flux defined by Chen *et al.*, which requires some form of large-eddy approximation, we plot the instantaneous point-wise nonlinear term in the local enstrophy equation and attempt to couple this quantity to the Weiss function, $Q_w(t, \mathbf{x})$, introduced in Section 4.2. Multiplying the vorticity equation with $\omega(t, \mathbf{x})$, one obtains the balance equation for the local enstrophy $Z(t, \mathbf{x}) := \frac{1}{2}(\omega(t, \mathbf{x}))^2$,

$$\partial_t Z(t, \mathbf{x}) + \Psi(t, \mathbf{x}) = (1/Re)\, \omega(t, \mathbf{x})\Delta\omega(t, \mathbf{x}) + \omega(t, \mathbf{x})q(t, \mathbf{x}),$$

where the local transfer term is just

$$\Psi(t, \mathbf{x}) := \omega(t, \mathbf{x})\left(\mathbf{u}(t, \mathbf{x}) \cdot \nabla\omega(t, \mathbf{x})\right).$$

Of course, this latter term drops out in the domain integrated balance.

Considering first snapshots of the stream function $\psi(t, \mathbf{x})$ and vorticity $\omega(t, \mathbf{x})$ at the same instant, $t = 200$, Figure 5.11(a) and (b), one sees the remains of a larger circulation cell. This feature is most pronounced in the stream function, where the cell occupies a large part of the domain. In the vorticity field one observes two pronounced vortex cores of opposite sign, one of which belongs to the large cell, as well as several elongated filamentary structures extending from the wall regions into the interior of the domain; these latter filaments are clearly detached boundary layers. Recall that the

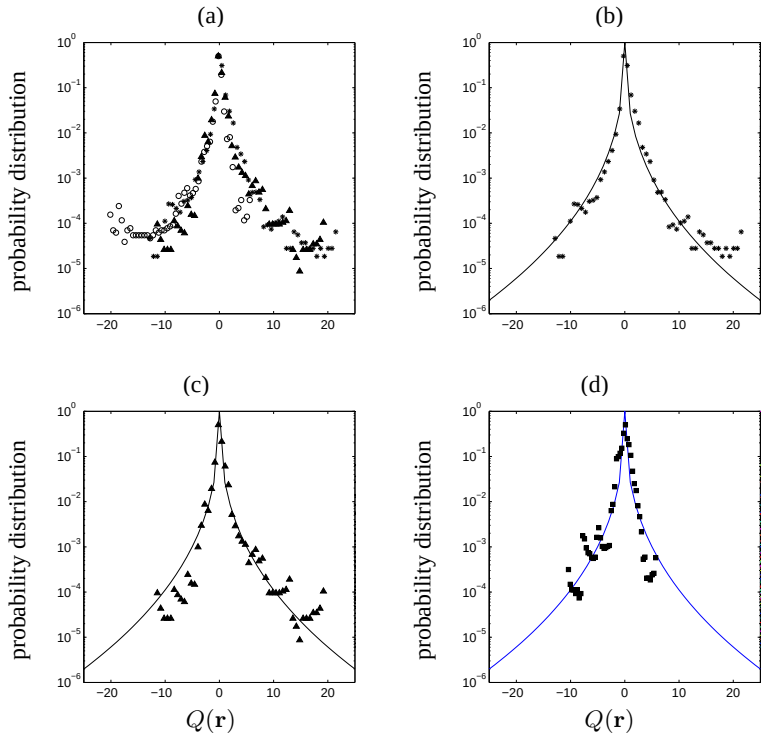

Figure 5.10: *Probability distribution function, $P(Q)$, of the quantity $Q(\mathbf{r})$ (a) at three separation lengths, $r = 0.006$ (stars), $r = 0.012$ (circles) and $r = 0.024$ (filled triangles). Separate PDFs for $r = 0.006$ (b), $r = 0.024$ (c) and $r = 0.096$ (d) are compared to an exponential fit (solid line in each graph).*

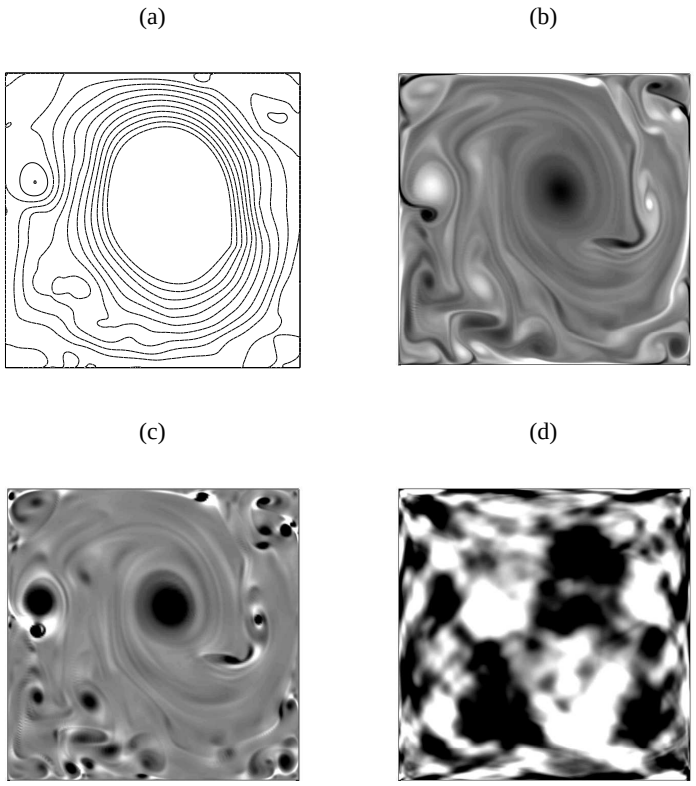

Figure 5.11: *Iso-contour plot of the stream function, $\psi(t, \mathbf{x})$, where contours range from -1 to 1, with an interval of 0.1 and dashed lines represent negative values (a). Snapshot of the normalized vorticity, $2\omega(t, \mathbf{x})/\langle|\omega(t, \mathbf{x})|\rangle$, compressed to the interval (-5,5) (b). Normalized Weiss function, $Q_w(t, \mathbf{x})/\langle|Q_w(t, \mathbf{x})|\rangle$, compressed to the interval (-5,5) (c) and the normalized nonlinear term in the point-wise enstrophy equation, $\Psi(t, \mathbf{x})/\langle|\Psi(t, \mathbf{x})|\rangle$, compressed to the interval [-1,1](d). In plots (b), (c) and (d) white indicates positive values and black indicates negative values, for all plots $t = 200$.*

instantaneous 1D Chebyshev spectra measured on the perpendicular lines $x = 0$ and $y = 0$ at $t = 200$ and shown in Figure 5.3 in Section 5.2, revealed a large variation in scaling. These differences in scaling can be explained from the vorticity field, where $x = 0$ is largely dominated by the circulation cell, whereas $y = 0$ picks up information from filamentary structures and secondary vortices as well.
The Weiss function $Q_w(t, \mathbf{x})$, Figure 5.11(c), identifies two strong elliptic cores, corresponding to the two vortices of opposite sign and many smaller cores, whereas the surrounding flow is weakly strain-dominated. Whereas the regions where $\Psi(t, \mathbf{x}) < 0$ seem to be unrelated to the Weiss function, the regions where $\Psi(t, \mathbf{x}) > 0$ seem to be coupled mainly to the regions that are weakly strain-dominated.

Further discussion

The purpose of the present Chapter was to examine scaling properties of small-scale vorticity statistics under the condensation regime phenomenology. Due to the non-isotropy of the flow a comparison with scaling results for pure Navier-Stokes flows on a double-periodic domain is problematic. *A priori* results on the vorticity statistics, such as the relation between the enstrophy transfer and the mixed structure function of third order, may be questionable for the case of a bounded no-slip domain. Also, caution should be taken in translating the scaling exponents obtained from Chebyshev spectra into the Fourier spectral exponents as used in classical KLB-theory.
Another problem in connecting the results in the present Chapter with KLB-theory and computational results known from the relevant literature is the low integral-scale Reynolds numbers examined here. Higher Reyolds numbers may give rise to a significantly different scaling results, as was e.g. observed by Clercx and van Heijst [27] for increasing Reynolds numbers in decaying flows on a bounded square domain. It follows that there is a need for higher Reynolds number computations with strongly increased resolutions, spanning a larger inertial range.
The flows considered here are purely two-dimensional, a property that may not be satisfied for the smallest length-scales in laboratory experiments on shallow fluid layers, as remarked by Paret *et al.* [106], see also the discussion on the role of bottom friction in such experiments by Satijn *et al.* [124]. Furthermore, the no-slip condition is the natural boundary condition in such laboratory experiments, rendering computations with a similar geometry and no-slip boundary conditions a necessary step if results from the laboratory are to be compared with existing scaling theories.

Chapter 6

Summary and Conclusions

We have found a strange footprint on the shores of the unknown. We have devised profound theories, one after another, to account for its origins. At last, we have succeeded in reconstructing the creature that made the footprint.
And lo! It is our own.
Sir Arthur Eddington (1882 - 1944)

The work reported in this thesis, a follow-up to the PhD work of Maassen [85] on decaying flows on bounded domains, concerns several aspects of forced Navier-Stokes flows on a bounded domain for low to intermediate values of the integral-scale Reynolds number, Re_*, achieving at most $Re_* \simeq 7500$. Our conclusions highlight the effect of the no-slip boundaries on the evolution of the flow. In itself it is not surprising that such an influence occurs; flows in a non-homogeneous setting are expected to deviate from the isotropic flows *a priori*, where the isotropic setting refers to the plane in the case of heuristic turbulence theory or to a double-periodic domain in the case of 2D computations. However, the generation of viscous boundary layers and their influence on the flow in the interior of the domain remains a surprisingly much neglected issue in the relevant literature on (quasi) two-dimensional viscous flows.

A pronounced example of the difference of a bounded flow as opposed to flows in a double-periodic domain is observed when one follows the route to chaos in a square domain. As a function of the kinematic viscosity parameter this route can roughly be divided into two parts; a Ruelle-Takens scenario [120, 96] leads the flow from stationary to low-dimensional chaotic solutions, as shown by Molenaar *et al.* [94]. The low-dimensional chaotic motions are then disturbed by increasingly frequent events of increasing intensity, resembling a Manneville and Pomeau [90] intermittency scenario. Our results reveal a marked difference with similar experiments on a double-periodic domain by Braun *et al.* [18], where the transition sequence included travelling wave instabilities and a period-doubling cascade. On the other hand, computations with one periodic and one no-slip direction by these authors showed chaos occurring after a break-up of a temporally periodic flow with two fundamental frequencies, which is more like the Ruelle-Takens scenario observed here. An explanation for these differences follows from the fact that instabilities in a no-slip domain are caused by the formation of secondary vortices and the detachment of viscous boundary layers, a process that is, naturally, absent in a double-periodic domain. A problem with the adopted strategy in the exploration of the route to chaos is that no continuous bifurcation se-

quence could be established; only a discrete set of values for the control parameter were examined. Also, our exploration was limited by the computational resolution, rather than by phenomenological considerations.

An interesting phenomenology can be observed in forced flows for intermediate values of the Reynolds number on a square no-slip domain, where the forcing mechanism is a time-dependent, stochastic process, comparable to the action of a stirring device that moves in random order through the fluid. Self-organization of the flow takes place, leading to a single large circulation cell in the interior of the domain. At the solid domain-boundary viscous boundary layers are created, which may eventually detach from the wall and roll-up in the corners of the domain. When these secondary vortices interact with the large circulation cell, the latter may become unstable and collapse, after which a new phase of self-organization may lead to another circulation cell, possibly of opposite sign, Molenaar *et al.* [93]. Such findings are in marked contrast to the phenomenology of forced flows in a double-periodic domain, see Hossain *et al.* [64], where the usual end-state is a stable domain-filling dipolar vortex. From several inequalities describing the behavior of the domain-integrated angular momentum, $L(t)$, on both a square and a circular no-slip domain, bounds were obtained on the behavior of that quantity. In some instances these bounds are physically uninteresting or unobtainable, but in such cases it makes sense to explore if the bounds can be improved using scaling results from computations or dimensional arguments. Furthermore, it is interesting to evaluate the phenomenology for higher integral-scale Reynolds numbers compared to those considered here, which is likely to lead to different results.

Finally, if one examines the statistics of the small scales in the disrupted condensation regime phenomenology, strong deviations from Gaussian behavior can be observed. These deviations are thought to be caused by the observed phenomenology; especially the advection of boundary layers into the interior and the build-up and break-down of a large circulation cell prevent a more or less isotropic situation, with the associated Gaussian statistics, from developing. The scaling exponent for the second-order vorticity structure function, $\zeta(2)$, was found to be larger than the upper bound prediction by Eyink [39], $\zeta(2) \leq 2/3$, but smaller than the estimate by Tran and Bowman [142], $\zeta(2) > 2$, following from their prediction on spectral scaling in the direct cascade range. On the other hand, the observation that this exponent is nonzero, $\zeta(2) \neq 0$, also contradicts earlier results by Paret *et al.* [106], obtained from laboratory experiments in square PVC container with no-slip boundaries. Here, again, it is interesting to obtain data for higher resolution and higher Reynolds number computations, which is necessary to make a reliable comparison of results to existing scaling theories. Furthermore, a means of determining the enstrophy transfer, $\chi(\mathbf{r})$, other than by means of the mixed third-order structure function has to be devised. Notwithstanding earlier experimental results, the applicability of the latter method to a no-slip domain is not without doubt, as neither of the assumptions of isotropy or a constant enstrophy transfer are satisfied in that case.

Considering the differences between forced Navier-Stokes flows on a double-periodic domain and the type of forced flows examined here, it seems unlikely that a simple one-to-one correspondence exists between the former and (quasi) two-dimensional flows in domains with rigid walls, as observed in laboratory experiments. Furthermore, it is at present still unclear how any of the wall-bounded settings for two-dimensional flows relate to the classical KLB-theory. In fact, as argued by Tran and Bowman [143], it is also

uncertain how double-periodic flows relate to KLB-theory. Furthermore, the purely two-dimensional case considered in this thesis is hard to achieve in a laboratory experiment, as one is likely to introduce some form of bottom friction or three-dimensional effect on the smallest scales of motion, which greatly increases the complexity of the problem. However, our computations can be viewed as an intermediate step between the laboratory experiment on one hand and computations on a double-periodic domain on the other.

References

[1] H. D. I. Abarbanel. *Analysis of observed chaotic data*. Springer Verlag, Del Mar, 1996.

[2] R. A. Adams. *Sobolev spaces*. Academic Press, New York, 1975.

[3] G. Ahlers. Low temperature studies of the Rayleigh-Bénard instability and turbulence. *Physical Review Letters*, 33:1185–1188, 1974.

[4] K. Alvelius. Random forcing of three-dimensional homogeneous turbulence. *Physics of Fluids*, 11:1880–1889, 1999.

[5] G. B. Arfken and H. J. Weber. *Mathematical methods for physicists*. Academic Press, San Diego, 1995.

[6] A. Babiano, C. Basdevant, B. Legras, and R. Sadourny. Vorticity and passive-scalar dynamics in two-dimensional turbulence. *Journal of Fluid Mechanics*, 183:379–397, 1987.

[7] A. Babiano, B. Dubrulle, and P. Frick. Scaling properties of numerical two-dimensional turbulence. *Physical Review E*, 52:3719–3729, 1995.

[8] M. V. Bartuccelli, C. R. Doering, and J. D. Gibbon. Ladder theorems for the 2D and 3D Navier-Stokes equations on a finite periodic domain. *Nonlinearity*, 4:531–542, 1991.

[9] C. Basdevant and T. Philipovitch. On the validity of the "Weiss-criterion" in the two-dimensional turbulence. *Physica D*, 73:17–30, 1994.

[10] G. K. Batchelor. Computation of the energy spectrum in two-dimensional turbulence. *Physics of Fluids*, suppl.II:233–239, 1969.

[11] F. Belin, P. Tabeling, and H. Willaime. Exponents of structure functions in a low temperature helium experiment. *Physica D*, 93:52–63, 1996.

[12] R. Benzi, G. Amati, C. M. Casciola, F. Toschi, and R. Piva. Intermittency and scaling laws for wall bounded turbulence. *Physics of Fluids*, 11:1284–1286, 1999.

[13] D. Bernard. Three-point velocity correlation functions in two-dimensional forced turbulence. *Physical Review E*, 60:6184–6187, 1999.

[14] G. Boffetta, A. Celani, and M. Vergassola. Inverse energy cascade in two-dimensional turbulence: Deviations from Gaussian behavior. *Physical Review E, Rapid Communications*, 61:R29–R32, 2000.

[15] V. Borue. Spectral exponents of enstrophy cascade in stationary two-dimensional homogeneous turbulence. *Physical Review Letters*, 71:3967–3970, 1993.

[16] V. Borue. Inverse energy cascade in stationary two-dimensional homogeneous turbulence. *Physical Review Letters*, 72:1475–1478, 1994.

[17] A. Brandstäter, J. Swift, H. L. Swinney, A. Wolf, J.D. Farmer, E. Jen, and J.P. Crutchfield. Low-dimensional chaos in a hydrodynamic system. *Physical Review Letters*, 51:1442–1445, 1983.

[18] R. Braun, F. Feudel, and P. Guzdar. Route to chaos for a two-dimensional externally driven flow. *Physical Review E*, 58:1927–1932, 1998.

[19] Th. Buzug, J. von Stamm, and G. Pfister. Fractal dimensions of strange attractors obtained from the Taylor-Couette experiment. *Physica A*, 191:559–563, 1992.

[20] C. Canuto, M. Y. Hussaini, A. Quarteroni, and T. A. Zang. *Spectral methods in fluid dynamics*. Springer-Verlag, New York, 1988.

[21] G. F. Carnevale. Two-dimensional turbulence: an overview. *(to appear)*, -:–, 2004.

[22] P. H. Chavanis and J. Sommeria. Classification of self-organized vortices in two-dimensional turbulence: the case of a bounded domain. *Journal of Fluid Mechanics*, 314:267–297, 1996.

[23] S. Chen, R. E. Ecke, G. L. Eyink, X. Wang, and Z. Xiao. Physical mechanism of the two-dimensional enstrophy cascade. *Physical Review Letters*, 91:214501–1–4, 2003.

[24] H. J. H. Clercx. A spectral solver for the Navier-Stokes equations in velocity-vorticity formulation for flows with two nonperiodic directions. *Journal of Computational Physics*, 137:186–211, 1997.

[25] H. J. H. Clercx, S. R. Maassen, and G. J. F. van Heijst. Spontaneous spin-up during the decay of 2D turbulence in a square container with rigid boundaries. *Physical Review Letters*, 80:5129–5132, 1998.

[26] H. J. H. Clercx, A. H. Nielsen, D. J. Torres, and E. A. Coutsias. Two-dimensional turbulence in square and circular domains with no-slip walls. *European Journal of Mechanics B/Fluids*, 20:557–576, 2001.

[27] H. J. H. Clercx and G. J. F. van Heijst. Energy spectra for decaying 2D turbulence in a bounded domain. *Physical Review Letters*, 85:306–309, 2000.

[28] H. J. H. Clercx and G. J. F. van Heijst. Dissipation of kinetic energy in two-dimensional bounded flows. *Physical Review E*, 65:066305–1–4, 2002.

[29] P. Constantin, C. Foias, and O. P. Manley. Effects of the forcing function spectrum on the energy spectrum in 2-D turbulence. *Physics of Fluids*, 6:427–429, 1994.

[30] P. Constantin, C. Foias, and R. Temam. On the dimension of the attractors in two-dimensional turbulence. *Physica D*, 30:284–296, 1988.

[31] A. Cumming and P. S. Linsay. Quasiperiodicity and chaos in a system with three competing frequencies. *Physical Review Letters*, 60:2719–2722, 1988.

[32] S. Danilov and D. Gurarie. Forced two-dimensional turbulence in spectral and physical space. *Physical Review E*, 63:061208–1–061208–12, 2001.

[33] S. Danilov and D. Gurarie. Nonuniversal features of forced two-dimensional turbulence in the energy range. *Physical Review E, Rapid Communications*, 63:020203–1–4, 2001.

[34] O. Daube. Resolution of the 2D Navier-Stokes equations in velocity-vorticity form by means of an influence matrix technique. *Journal of Computational Physics*, 103:402–414, 1992.

[35] C. R. Doering and J. D. Gibbon. *Applied analysis of the Navier-Stokes equations*. Cambridge University Press, Cambridge, 1995.

[36] M. Dubois, M. A. Rubio, and P. Berge. Experimental evidence of intermittencies associated with a subharmonic bifurcation. *Physical Review Letters*, 51:1446–1449, 1983.

[37] J. P. Eckmann and D. Ruelle. Fundamental limitations for estimating dimensions and Lyapunov exponents in dynamical systems. *Physica D*, 56:185–187, 1992.

[38] V. Eswaran and S. B. Pope. An examination of forcing in direct numerical simulations of turbulence. *Computers and Fluids*, 16:257–278, 1988.

[39] G. L. Eyink. Exact results on scaling exponents in the 2D enstrophy cascade. *Physical Review Letters*, 74:3800–3803, 1995.

[40] G. L. Eyink. Exact results on stationary turbulence in 2D: consequences of vorticity conservation. *Physica D*, 91:97–142, 1996.

[41] G. L. Eyink. Eyink replies. *Physical Review Letters*, 76:1975, 1996.

[42] G. Falkovich and V. Lebedev. Universal direct cascade in two-dimensional turbulence. *Physical Review E*, 50:3883–3899, 1994.

[43] G. Falkovich and V. Lebedev. Comments on "Exact results on scaling exponents in the 2D enstrophy cascade". *Physical Review Letters*, 76:1974, 1996.

[44] J. D. Farmer. Chaotic attractors of an infinite-dimensional dynamical system. *Physica D*, 4:366–393, 1982.

[45] M. J. Feigenbaum. The onset spectrum of turbulence. *Physics Letters*, 74A:375–378, 1979.

[46] M. J. Feigenbaum. Universal behavior in nonlinear systems. *Physica D*, 7:16–39, 1983.

[47] F. Feudel and N. Seehafer. Bifurcation and pattern formation in a two-dimensional Navier-Stokes fluid. *Physical Review E*, 52:3506–3511, 1995.

[48] C. Foias. What do the navier-stokes equations tell us about turbulence? In M. L. Lapidus, L. H. Harper, and A. J. Rumbos, editors, *Harmonic analysis and nonlinear differential equations*, pages 151–180, New York, 1997. American Mathematical Society.

[49] C. Foias, O. P. Manley, R. Rosa, and R. Temam. *Navier-Stokes equations and turbulence*. Cambridge University Press, Cambridge, 2001.

[50] C. Foias, O. P. Manley, R. Temam, and Y. M. Treve. Asymptotic analysis of the Navier-Stokes equations. *Physica D*, 9:157–188, 1983.

[51] C. Foias and R. Temam. Some analytic and geometric properties of solutions of the evolution Navier-Stokes equations. *Journal de Mathematique Pures et Appliquées*, 58:339–368, 19879.

[52] A. M. Fraser and H. L. Swinney. Independent coordinates for strange attractors from mutual information. *Physical Review A*, 33:1134–1140, 1986.

[53] U. Frisch. *Turbulence*. Cambridge University Press, Cambridge, 1995.

[54] U. Frisch and P. L. Sulem. Numerical simulation of the inverse cascade in two-dimensional turbulence. *Physics of Fluids*, 27:1921–1923, 1984.

[55] G. P. Galdi. *An introduction to the mathematical theory of the Navier-Stokes equations, vol. I, II*. Springer-Verlag, New York, 1994.

[56] G. Gallavotti. *Foundations of fluid dynamics*. Springer-Verlag, Rome, 2001.

[57] M. Giglio, S. Musazzi, and U. Perini. Transition to chaotic behavior via a reproducible sequence of period-doubling bifurcations. *Physical Review Letters*, 47:243–246, 1981.

[58] W. I. Goldburg, M. A. Rutgers, and X l. Wu. Experiments on turbulence in soap films. *Physica A*, 239:340–349, 1997.

[59] J. P. Gollub and S. V. Benson. Many routes to turbulent convection. *Journal of Fluid Mechanics*, 100:449–470, 1980.

[60] J. P. Gollub and H. L. Swinney. Onset of turbulence in a rotating fluid. *Physical Review Letters*, 35:927–930, 1975.

[61] P. Grassberger and I. Procaccia. Estimation of the Kolmogorov entropy from a chaotic signal. *Physical Review A*, 28:2591–2593, 1983.

[62] D. B. Haidvogel and T. A. Zang. The accurate solution of Poisson's equation by expansion in Chebyshev polynomials. *Journal of Computational Physics*, 30:167–180, 1979.

[63] R. Hegger, H. Kantz, and T. Schreiber. Practical implementation of nonlinear time series methods: The TISEAN package. *Chaos*, 9:413–40, 1999.

[64] M. Hossain, W. H. Matthaeus, and D. Montgomery. Long-time state of inverse cascades in the presence of a maximum length scale. *Journal of Plasma Physics*, 30:479–493, 1983.

[65] T. Ishihara and Y. Kaneda. Energy spectrum in the enstrophy transfer range of two-dimensional forced turbulence. *Physics of Fluids*, 13:544–547, 2001.

[66] L. P. Kadanoff. Turbulent heat flows: structure and scaling. *Physics Today*, 54:34–39, 2000.

[67] Y. Kaneda and T. Ishihara. Nonuniversal k^{-3} energy spectrum in stationary two-dimensional homogeneous turbulence. *Physics of Fluids*, 65:845–894, 2001.

[68] H. Kellay, C. H. Bruneau, and X l. Wu. Probability density functions of the enstrophy transfer in two dimensional grid turbulence. *Physical Review Letters*, 84:1696–1699, 2000.

[69] H. Kellay and W. I. Goldburg. Two-dimensional turbulence: a review of some recent experiments. *Reports on Progress in Physics*, 65:845–894, 2002.

[70] H. Kellay, X l. Wu, and W. I. Goldburg. Experiments with turbulent soap films. *Physical Review Letters*, 74:3975–3978, 1995.

[71] M. B. Kennel, R. Brown, and H. D. I. Abarbanel. Determining embedding dimension for phase-space reconstruction using a geometrical construction. *Physical Review A*, 45:3403–3411, 1992.

[72] S. Kida, M. Yamada, and K. Ohkitani. A route to chaos and turbulence. *Physica D*, 37:116–125, 1989.

[73] L. Kleiser and U. Schumann. In E. H. Hirschel, editor, *Third GAMM Conference on Numerical Methods in Fluid Mechanics*, page 165, Braunschweig, 1980. Vieweg.

[74] R. H. Kraichnan. Inertial ranges in two-dimensional turbulence. *Physics of Fluids*, 10:1417–1423, 1967.

[75] R. H. Kraichnan. Inertial range transfer in two- and three-dimensional turbulence. *Journal of Fluid Mechanics*, 47:525–535, 1971.

[76] L. D. Landau and E. M. Lifschitz. *Fluid Mechanics*. Pergamon Press, Moscow, 1959.

[77] B. Legras, P. Santangelo, and R. Benzi. High-resolution numerical experiments for forced two-dimensional turbulence. *Europhysics Letters*, 5:37–42, 1988.

[78] C. E. Leith. Diffusion approximation for two-dimensional turbulence. *Physics of Fluids*, 11:671–673, 1968.

[79] S. Li, D. Montgomery, and W. B. Jones. Inverse cascades of angular momentum. *Journal of Plasma Physics*, 56:615–639, 1996.

[80] A. Libchaber, S. Fauve, and C. Laroche. Two-parameter study of the routes to chaos. *Physica D*, 7:73–84, 1983.

[81] E. H. Lieb. On characteristic exponents in turbulence. *Communications in Mathematical Physics*, 92:473–480, 1984.

[82] D. K. Lilly. Numerical simulation of two-dimensional turbulence. *Physics of Fluids Supplement*, 12:240–249, 1969.

[83] E. Lindborg and K. Alvelius. The kinetic energy spectrum of the two-dimensional enstrophy cascade. *Physics of Fluids*, 12:945–947, 2000.

[84] E. N. Lorenz. Deterministic nonperiodic flow. *Journal of Atmospheric Sciences*, 20:130–141, 1963.

[85] S. R. Maassen. *Self-organization of confined two-dimensional flows*. PhD thesis, Eindhoven University of Technology, Eindhoven, 2000.

[86] S. R. Maassen, H. J. H Clercx, and G. J. F. van Heijst. Self-organization of quasi-two-dimensional turbulence in stratified fluids in square and circular containers. *Physics of Fluids*, 814:2150–2169, 2002.

[87] M. E. Maltrud and G. K. Vallis. Energy spectra and coherent structures in numerical simulations of two-dimensional and beta-plane turbulence. *Journal of Fluid Mechanics*, 228:321–342, 1991.

[88] M. E. Maltrud and G. K. Vallis. Energy and enstrophy transfer in forced two-dimensional turbulence. *Physics of Fluids A*, 7:1760–1765, 1993.

[89] P. Manneville and Y. Pomeau. Intermittency and the Lorenz-model. *Physics Letters*, 75A:1–2, 1979.

[90] P. Manneville and Y. Pomeau. Different ways to turbulence in dissipative dynamical systems. *Physica D*, 1:219–226, 1980.

[91] B. K. Martin, X. L. Wu, and W. I. Goldburg. Spectra of decaying turbulence in a soap film. *Physical Review Letters*, 80:3964–3967, 1998.

[92] W. H. Matthaeus, W. T. Stribling, D. Martinez, S. Oughton, and D. Montgomery. Decaying, two-dimensional, Navier-Stokes turbulence at very long times. *Physica D*, 51:531–538, 1991.

[93] D. Molenaar, H. J. H. Clercx, and G. J. F. van Heijst. Angular momentum of forced 2D turbulence on a square no-slip domain. *Physica D*, 196:329–340, 2004.

[94] D. Molenaar, H. J. H. Clercx, and G. J. F. van Heijst. Confined two-dimensional fluid flow follows a Ruelle-Takens route to chaos. *(under consideration) Physical Review Letters*, 2004.

[95] T. Mullin (ed.). *The nature of chaos*. Oxford science publications, Oxford, 1993.

[96] S. Newhouse, D. Ruelle, and F. Takens. Occurence of strange axiom A attractors near quasi periodic flows on $T^m,\ m \geq 3$. *Communications in Mathematical Physics*, 64:35–40, 1978.

[97] J. J. Niemela, L. Skrbek, K. R. Sreenivasan, and R. J. Donnelly. The wind in confined thermal convection. *Journal of Fluid Mechanics*, 449:169–178, 2001.

[98] T. Nozawa and S. Yoden. Formation of zonal band structure in forced two-dimensional turbulence on a rotating sphere. *Physics of Fluids*, 9:2081–2093, 1997.

[99] T. Nozawa and S. Yoden. Spectral anisotropy in forced two-dimensional turbulence on a rotating sphere. *Physics of Fluids*, 9:3834–3842, 1997.

[100] K. G. Oetzel and G. K. Vallis. Strain, vortices, and the enstrophy inertial range in two-dimensional turbulence. *Physics of Fluids*, 9:2991–3004, 1997.

[101] K. Ohkitani. Log-corrected energy spectrum and dimension of attractor in two-dimensional turbulence. *Physics of Fluids A*, 1:451–452, 1989.

[102] K. Ohkitani. Wave number space dynamics of enstrophy cascade in a forced two-dimensional turbulence. *Physics of Fluids A*, 3:1598–1611, 1991.

[103] S. A. Orszag. Numerical methods for the simulation of turbulence. *Physics of Fluids, Suppl. II*, 12:250–257, 1969.

[104] M. R. Overholt and S. B. Pope. A deterministic forcing scheme for direct numerical simulations of turbulence. *Computers and Fluids*, 27:11–28, 1998.

[105] N. H. Packard, J. P. Crutchfield, J. D. Farmer, and R. S. Shaw. Geometry from a time series. *Physical Review Letters*, 45:712–716, 1980.

[106] J. Paret, M. Jullien, and P. Tabeling. Vorticity statistics in the two-dimensional enstrophy cascade. *Physical Review Letters*, 83:3418–3421, 1999.

[107] J. Paret and P. Tabeling. Intermittency in the two-dimensional inverse cascade of energy: Experimental observations. *Physics of Fluids*, 10:3126–3136, 1998.

[108] G. Pfister, Th. Buzug, and N. Enge. Characterization of experimental time series from Taylor-Couette flow. *Physica D*, 58:441–454, 1992.

[109] Y. B. Pointin and T. S. Lundgren. Statistical mechanics of two-dimensional vortices in a bounded container. *Physics of Fluids*, 19:1459–1470, 1976.

[110] B. Protas, A. Babiano, and N. K.-R. Kevlahan. On geometrical alignment properties of two-dimensional forced turbulence. *Physica D*, 128:169–179, 1999.

[111] A. Provenzale, L. A. Smith, R. Vio, and G. Murante. Distinguishing between low-dimensional dynamics and randomness in measured time series. *Physica D*, 58:31–49, 1992.

[112] L. E. Reichl. *A modern course in statistical physics*. Wiley-interscience, Austin, 1988.

[113] M. K. Rivera, W. B. Daniel, S. Y. Chen, and R. E. Ecke. Energy and enstrophy transfer in decaying two-dimensional turbulence. *Physical Review Letters*, 90:104502–1–4, 2003.

[114] J. C. Robinson. A rigorous treatment of 'experimental' observations for the two-dimensional Navier-Stokes equations. *Proceedings of the Royal Society of London A*, 457:1007–1020, 2001.

[115] M. T. Rosenstein, J. J. Collins, and C. J. De Luca. A practical method for calculating largest Lyapunov exponents from small data sets. *Physica D*, 65:117–134, 1993.

[116] M. T. Rosenstein, J. J. Collins, and C. J. De Luca. Reconstruction expansion as a geometry-based framework for choosing proper delay times. *Physica D*, 73:82–98, 1994.

[117] J. C. Roux, R. H. Somyi, and H. L. Swinney. Observations of a strange attractor. *Physica D*, 8:257–266, 1983.

[118] D. Ruelle. Small random perturbations of dynamical systems and the definition of attractors. *Communications in Mathematical Physics*, 82:137–151, 1981.

[119] D. Ruelle. Characteristic exponents for a viscous fluid subjected to time dependent forces. *Communications in Mathematical Physics*, 93:285–300, 1984.

[120] D. Ruelle and F. Takens. On the nature of turbulence. *Communications in Mathematical Physics*, 20:167–192, 1971.

[121] M. A. Rutgers. Forced 2D turbulence: experimental evidence of simultaneous inverse energy and forward enstrophy cascades. *Physical Review Letters*, 81:2244–2247, 1998.

[122] M. A. Rutgers, X l. Wu, R. Bhagavatula, A. A. Petersen, and W. I. Goldburg. Two-dimensional velocity profiles and laminar boundary layers in flowing soap films. *Physics of Fluids*, 8:2847–2854, 1996.

[123] P. G. Saffman. *Vortex dynamics*. Cambridge University Press, Cambridge, 1992.

[124] M. P. Satijn, A. W. Cense, R. Verzicco, H. J. H. Clercx, and G. J. F. van Heijst. Three-dimensional structure and decay properties of vortices in shallow fluid layers. *Physics of Fluids*, 13:1932–1945, 2001.

[125] J. C. Saut and R. Temam. Generic properties of Navier-Stokes equations: genericity with respect to the boundary values. *Indiana University Mathematics Journal*, 29:427–446, 1980.

[126] H. G. Schuster. *Deterministic chaos, an introduction*. VCH, Kiel, 1995.

[127] L. M. Smith and V. Yakhot. Bose condensation and small-scale strucure generation in a random force driven 2D turbulence. *Physical Review Letters*, 71:352–355, 1993.

[128] L. M. Smith and V. Yakhot. Finite-size effects in forced two-dimensional turbulence. *Journal of Fluid Mechanics*, 274:115–138, 1994.

[129] J. Sommeria. Experimental study of the two-dimensional inverse energy cascade in a square box. *Journal of Fluid Mechanics*, 170:139–168, 1986.

[130] J. Sommeria and J. Verron. An investigation of nonlinear interactions in a two-dimensional recirculating flow. *Physics of Fluids*, 27:1918–1920, 1984.

[131] P. L. Sulem and U. Frisch. Bounds on energy flux for finite energy turbulence. *Journal of Fluid Mechanics*, 72:417–423, 1975.

[132] H. L. Swinney and J. P. Gollub. The transition to turbulence. *Physics Today*, 31:41–49, 1978.

[133] P. Tabeling. Two-dimensional turbulence: a physicist approach. *Physics Reports*, 362:1–62, 2002.

[134] P. Tabeling, O. Cardoso, and B. Perrin. Chaos in a linear array of vortices. *Journal of Fluid Mechanics*, 213:511–530, 1990.

[135] P. Tabeling, G. Zocchie, F. Belin, J. Maurer, and H. Willaime. Probablity density functions, skewness and flatness in large Reynolds number turbulence. *Physical Review E*, 53:1613–1621, 1996.

[136] R. Temam. Infinite-dimensional dynamical systems in fluid mechanics. In F. Browder, editor, *Nonlinear functional analysis and its applications*, pages 431–445, New York, 1986. American Mathematical Society.

[137] R. Temam. *Infinite dimensional dynamical systems in mechanics and physics*. Springer-Verlag, New York, 1988.

[138] R. Temam. *Navier-Stokes equations and nonlinear functional analysis*. SIAM, Philadelphia, 1995.

[139] H. Tennekes. Turbulent flow in two and three dimensions. *Bulletin of the American Meteorological Society*, 59:22–28, 1978.

[140] J. M. T. Thompson and H. B. Stewart. *Nonlinear dynamics and chaos*. John Wiley & Sons, Chichester, 2002.

[141] P. Topping. Pressure estimates in two dimensional incompressible fluid flow. *Physica D*, 137:143–156, 2000.

[142] C. V. Tran and J. C. Bowman. On the dual cascade in two-dimensional turbulence. *Physica D*, 176:242–255, 2003.

[143] C. V. Tran and J. C. Bowman. Robustness of the inverse cascade in two-dimensional turbulence. *Physical Review E*, 69:036303–1–7, 2004.

[144] C. V. Tran, T. G. Shepherd, and H. R. Cho. Stability of stationary solutions of the forced Navier-Stokes equations on the two-torus. *Discrete and continuous dynamical systems-series B*, 6:1–13, 2000.

[145] Y. M. Treve and O. P. Manley. Energy conserving Galerkin approximations for 2-d hydrodynamic and MHD Bénard convection. *Physica D*, 4:319–342, 1982.

[146] G. J. F. van Heijst and R. C. Kloosterziel. Tripolar vortices in a rotating fluid. *Nature*, 338:569–571, 1989.

[147] F. Verhulst. *Nonlinear differential equations and dynamical systems*. Springer-Verlag, Utrecht, 1996.

[148] M. J. Vishik and A. V. Fursikov. *Mathematical problems of statistical hydromechanics*. Kluwer Academic Publishers, Bussum, 1988.

[149] R. W. Walden, P. Kolodner, A. Passner, and C. M. Surko. Nonchaotic Rayleigh-Bénard convection with four and five incommensurate frequencies. *Physical Review Letters*, 53:242–245, 1984.

[150] J. Weiss. The dynamics of enstrophy transfer in two-dimensional hydrodynamics. *Physica D*, 48:273–294, 1991.

[151] M. G Wells, H. J. H. Clercx, and G. J. F. van Heijst. Laboratory and numerical experiments of continually forced two-dimensional turbulence. *(to appear in) Journal of Fluid Mechanics*, -:–, 2004.

[152] A. Wolf, J. B. Swift, H. L. Swinney, and J. A. Vastano. Determining Lyapunov exponents from a time series. *Physica D*, 16:285–317, 1985.

[153] Z. Yin. *On statistical-mechanical descriptions of decaying two-dimensional turbulence*. PhD thesis, Eindhoven University of Technology, Eindhoven, 2003.

[154] Z. Yin, H. J. H. Clercx, and D. Montgomery. On an easily implemented parallel scheme for a 2D Fourier pseudospectral algorithm. *Computers & Fluids*, 33:509–520, 2004.

[155] E. Zeidler. *Applied functional analysis*. Springer-Verlag, New York, 1991.

Samenvatting

Het proefschrift bevat de resultaten van een numerieke en theoretische studie naar geforceerde twee-dimensionale (2D) visceuze stromingen op een begrensd domein. De studie is een onderdeel van het 2D turbulentie programma van de Stichting voor Fundamenteel Onderzoek der Materie (FOM). Numerieke simulaties werden uitgevoerd met een bestaand computer model, gebaseerd op een pseudo-spectrale discretisatie techniek. Er is gebruik gemaakt van de supercomputers van de Stichting Nationale Computerfaciliteiten (NCF). Hierbij een woord van dank aan zowel de NCF als FOM voor de geboden financiële ondersteuning.

Voor een tijdsonafhankelijke forcering werd bekeken wat de eindtoestand van de stroming is als de waarde van de kinematische viscositeit in discrete stappen wordt verlaagd, de zogenaamde route naar chaos. Daarbij kijkt men voornamelijk naar het gedrag van het systeem in de tijd, door, bijvoorbeeld, op bepaalde punten in het domein de waarden van de vorticiteit te meten in regelmatige intervallen. Voor afnemende waarden van de viscositeitsparameter vindt men een opeenvolging van stationair, periodiek, dubbel-periodiek, drievoudig-periodiek en, uiteindelijk, mild-chaotisch gedrag. Deze transitiereeks lijkt sterk op het uit de chaostheorie bekende Ruelle-Takens scenario. Echter, het betreft hier laag-dimensionale chaos; het gedrag van het systeem lijkt nog steeds sterk op de voorafgaande periodieke bewegingen maar is niet meer zo netjes geordend als tijdens het periodieke regime. Met laag-dimensionaal wordt overigens bedoeld dat er slechts een beperkt aantal vrijheidsgraden nodig zijn om het systeem te beschrijven. Dit in tegenstelling tot, bijvoorbeeld, een turbulente stroming die juist gekenmerkt wordt door een groot aantal vrijheidsgraden.
Laat men nu de waarde van de kinematische viscositeit nog verder afnemen, dan wordt het mild-chaotische regime in toenemende mate verstoord door perioden met hoog-dimensionaal gedrag van grote intensiteit. Naar het duale karakter van het systeem wordt in dit geval gerefereerd met de term intermittentie. Op een gegeven moment overheerst het hoog-dimensionale gedrag volledig en is de stroming in een tweede chaotische fase terecht gekomen. Dit tweede deel van de transitiereeks lijkt sterk op de intermittentie-route tot chaos, eveneens bekend uit de chaostheorie. Om het waargenomen gedrag te analyseren kan men enerzijds de gemeten tijdreeksen bekijken en Fourier spectra of structuur functies berekenen. Anderzijds kan men, door een gemeten tijdreeks uit te zetten tegen een iets vertraagde versie van zichzelf (in twee of meerdere dimensies), proberen om de faseruimte van het systeem te reconstrueren. Punten die in de tijdreeks ver van elkaar verwijderd zijn kunnen in faseruimte vlak naast elkaar komen te liggen, als gevolg van de dynamica van het systeem. Voor faseruimten met een dimensie hoger dan twee kan men doorsneden construeren, zogenaamde Poincaré secties, waarin voor bepaalde, laag-dimensionale gevallen duidelijke patronen herkenbaar zijn. Voor het intermittente gedrag is de dimensie van de bijbe-

horende faseruimte echter veelal zo groot, dat het moeilijk wordt om het gedrag te analyseren. Voor een echt turbulente stroming is dit zelfs onmogelijk, omdat het aantal datapunten dat vereist is om de faseruimte van het systeem grondig te kunnen analyseren exponentieel groeit met de dimensie van het systeem.

Houdt men een stroming in leven met een tijdsafhankelijke stochastische forcering, dan valt, voor een middelmatig aantal vrijheidsgraden, een spectaculaire fenomenologie waar te nemen. Er vindt spontane zelf-organisatie van de stroming plaats, zodat een domein-vullende circulatiecel ontstaat. Deze cel wordt echter gedestabiliseerd door interactie met aan de wand gegenereerde visceuze grenslagen. De destabilisatie kan uiteindelijk uitmonden in een volledige destructie van de cel, waarna zich een nieuwe cel kan vormen, mogelijk met een tegengestelde rotatie richting. Een dergelijke evolutie is sterk verschillende van het gedrag van geforceerde stromingen op een vierkant domein met twee periodieke richtingen. In het laatste geval ontstaat op een gegeven moment een stabiele dipool-structuur, die het gehele domein vult. De evolutie op een afgesloten domein wordt omschreven als een onderbroken condensatie regime, refererend naar een voorspelling van Kraichnan [74], dat er een ophoping van energie kan plaatsvinden in de grootste golflengte op een eindig domein. Fysisch vindt een dergelijk ophoping, of condensatie, plaats in de vorm van een grote domein vullende wervel.
Voor de beschreven fenomenologie zijn boven- en ondergrenzen aan het gedrag van het domein geintegreerde hoekimpulsmoment, onderzocht. Er is telkens gepoogd om vanuit eerste principes, d.w.z vanuit de bewegingsvergelijking, te werken om zodoende tot *a priori* resultaten te komen. In bepaalde gevallen lukt het echter niet om fysisch relevante grenzen op te stellen en is gebruik gemaakt van bestaande schalingsideen verkregen door numerieke simulaties of dimensie argumenten.

Behalve het gedrag van integrale grootheden is het van belang het lokale gedrag te meten, in de vorm van snelheids- en vorticiteitsverschillen. Deze structuurfuncties schalen met de afstand waarover ze gemeten worden. De schalingsexponenten die hieruit volgen geven een idee of de stroming zich gedraagt zoals voorspeld in de heuristische 2D turbulentietheorie of dat er afwijkingen plaatsvinden. In dit geval was het doel om voor het onderbroken condensatie regime het gedrag van de kleine schalen te bekijken. Met name de vorticiteits schalingsexponenten over de kleinste lengte schalen lijken af te wijken van het ideale gedrag, ten gevolge van de advectie van vorticiteitsfilamenten (losgelaten visceuze grenslagen) naar het inwendige van het domein.
Daarnaast is de kansverdeling van de derde-orde gemengde structuurfunctie bepaald. Op een dubbel-periodiek domein geeft laatstgenoemde structuurfunctie een idee van het transport van de enstrofie (gekwadrateerde vorticiteit). Echter, op een afgesloten domein lijken er nogal wat haken en ogen te zitten aan een dergelijke interpretatie; het domein is niet isotroop, de invoer van enstrofie is niet constant omdat er vorticiteit gegenereerd wordt aan de wanden en het Reynolds getal is in onze berekeningen aan de lage kant. Opvallend is dat de gemeten kansverdelingen toch sterk lijken op uit de literatuur bekende resultaten.

Samenvattend kan men stellen dat de aanwezigheid van vaste wanden een sterke invloed heeft op geforceerde Navier-Stokes stromingen met een middelmatig Reynolds getal. Zowel de fenomenologie als het schalingsgedrag van dergelijke stromingen lijkt af te wijken van het geijkte gedrag op een dubbel periodiek domein. Voor de interpretatie van laboratorium experimenten aan (quasi) twee-dimensionale stromingen, waar-

bij men vrijwel altijd met vaste wanden te maken heeft, is een dergelijke observatie van groot belang. Het lijkt erop dat er voor middelmatige Reynolds getallen geen directe vertaalslag mogelijk is van numerieke simulaties op een dubbel-periodiek domein naar laboratorium experimenten of van de experimenten naar de heuristische turbulentietheorie.

Acknowledgements

he struggled to get through his day, he was helplessly behind,
he poured himself onto the page,writing for hours at a time.
Six degrees of inner turbulence, Dream Theater (2001)

First of all, a big thank you goes out my supervisors, Herman Clercx and GertJan van Heijst, for all their advice and encouragement during the four years of this PhD project; I am very grateful for the confidence they put in a non-physicist. Helpful remarks and comments during the last phase of the project from my co-promotor Detlef Lohse and committee members Brenny van Groesen and Anton van Steenhoven are gratefully acknowledged.

A lot of thanks to all the staff at the Fluid Dynamics Laboratory and the fellow PhD students with whom I've had a chance of exchanging thoughts and drinks. I mention especially my office mate Werner Kramer (I'm still sorry for almost killing your plants), former postdoc Mathew Wells and (former) colleagues and students Adrian, Andrzej, Dennis, Geert, Jieheng, John, Laurens, Marleen, Martin, Petra, Ralph, Ruben, Sveta and Thijs. Thank you for the fun during conferences, the borrels in N-laag and the many, many coffee breaks in the egg. Also, I couldn't have survived without the help of Gert on small and big computer problems and secretaries Brigitte and Marjan on small and big administrative problems, merci beaucoup.

Gabriel and Irina, after breakfast in Paris I'm sure lunch awaits us in Barcelona. Thank you for a lot of fun during the last months in Eindhoven.

Climbing is my greatest passion, which I've been fortunate enough to share on many occasions with other fanatics; Arko, Harry, Jurriaan, Mathew, Maurice, Wouter and all the occasional weekend climbing friends, keep on rocking!

Dear Arko, Eric, Jeroen, Johan, Michel and Wouter. You showed me the true importance of friendship. You were there when the whisky bottle had to be emptied, when storms had to be endured and when life had to be celebrated. I thank you and your ladies for all those moments throughout the ups and downs of the last four years.

Finally, my brother and sisters, Emanuel, Rafaela, Ingvild, Janneke and Floor, my father and his wife, Martien and Juuleke, and my mother, Heidi, to whom this thesis is dedicated, I thank you for your unrelenting warmth and support.

Statements

accompanying the thesis

Forced Navier-Stokes Flows on a Bounded Two-Dimensional Domain

1 Two-dimensional fluid flow in a confined domain under stationary forcing follows a Ruelle-Takens route to chaos. *This thesis, Chapter 3.*

2 In forced flows on a bounded square domain a large circulation cell may form spontaneously, gain in strength, and collapse after interaction with the viscous boundary layers, after which the process may repeat itself. *Molenaar, Clercx & van Heijst. Physica D,* **196***, p.329-340, 2004.*

3 Interactions of the large scales of motion with small-scale boundary layers during the collapse of a large circulation cell on a bounded square domain leads to anomalous scaling behavior for the vorticity statistics. *This thesis, Chapter 5.*

4 The applicability of a Poincaré-Friedrichs inequality on a finite domain is a key difference between the classical theory of two-dimensional turbulence and a bounded two-dimensional flow. *This thesis, Chapters 1, 4 and 5.*

5 Besides bringing safety to the land, dikes may have destroyed the famous Holland light. *www.hollandslicht.nl.*

6 Contrary to popular belief, those rock climbers most at risk of injury are the most dedicated and the most skilled. *Wright, Royle & Marshall. Br. J. Sports Med.,* **35***, p.181-185, 2001.*

7 Small perturbations can change the roadmap to peace in the Middle-East into a roadmap to chaos.

8 Living in the global village has changed our notions of *goede buur* and *verre vriend*: today they may be one and the same person.

9 In climbing the pleasure is scale invariant: mastering a three meter boulder problem can be as rewarding as ascending a mountain.

10 Using bottled oxygen on the worlds' highest peaks is equivalent to competing in the *Tour de France* with a motorized bicycle.

Eindhoven,
October 2004